Generation of Human Induced Motor Neurons from Patients with BVVL Harboring Novel Neurodegeneration Causing Mutation

by

Deniz Ata

A Dissertation Submitted to the

Graduate School of Health Sciences

in Partial Fulfilment of the Requirements for

the Degree of

Doctor of Philosophy

in

Cellular and Molecular Medicine

KOÇ UNIVERSITY

February 2022

Generation of Human Induced Motor Neurons from Patients with BVVL Harboring Novel Neurodegeneration Causing Mutation

Koç University

Graduate School of Health Sciences

This is to certify that I have examined this copy of a doctoral dissertation by

Deniz ATA

and have found that it is complete and satisfactory in all respects,
and that any and all revisions required by the final
examining committee have been made.

Committee Members:

Prof. Dr. Tamer Tevfik Önder (Advisor) _____

Prof. Dr. Ayşe Nazlı Başak _____

Assoc. Prof. Dr. Atay Vural _____

Assoc. Prof. Dr. Bilal Ersen Kerman _____

Assoc. Prof. Dr. Gül Yalçın Çakmaklı _____

Date: 04/02/2022

To my selfless family and the many wonderous people, I've met along the way.

ABSTRACT

Generation of Human Induced Motor Neurons from Patients with BVVL Harboring Novel Neurodegeneration Causing Mutation

Deniz ATA

Doctor in Philosophy in Cellular and Molecular Medicine

February 4, 2022

Brown-Vialetto-Van Laere syndrome (BVVL) is a rare ALS-like neurodegenerative disorder. BVVL symptoms start with sensorineural deafness and cranial nerve palsies, followed by sensory and cranial neuron degeneration. Currently, mutations in the Riboflavin transporter family (RFVT/SLC52) protein-encoding genes are linked to riboflavin deficiency and BVVL. Interestingly, in our patient group of six siblings, no mutations were detected in *RFVT/SLC52* genes. Instead, whole-exome sequencing supported with in silico analysis and haplotype analysis resulted in a novel "Glu1656Lys" mutation in the *KIF13A* gene, encoding "Kinesin-like protein – KIF13A". KIF13A is known to play a major role in the endosomal – lysosomal system by mediating clathrin-independent endosomal recycling, which is crucial for a healthy, functioning nervous system. In this study, we have generated and characterized patient-specific induced pluripotent stem cells (iPSCs) of KU-BVVL patients carrying the neurodegeneration, causing novel KIF13A mutation. In addition, I have generated and characterized patient-specific induced motor neurons (iMNS) of KU-BVVL patients carrying the *KIF13A* mutation via a small-molecule-based differentiation method, adapted from previous studies and optimized to suit our experimental requirements. KU-BVVL-iMNs can be used as a valid model cell line that reflects the diseased phenotype as KIF13A protein is abundantly present in iMNs, predominantly in the soma and dendritic regions. Furthermore, I have also designed and generated various plasmid constructs, including mutant and wild type

constructs of KIF13A, *KIF13A* targeting CRISPR/Cas9 expression vectors, and KIF13A-BioID fusion constructs. These molecular reagents, along with patient iPSC-derived motor neurons, will be important tools to understand KIF13A related processes and molecular mechanisms that are crucial for a healthy, functioning nervous system.

ÖZETÇE

Nörodejenerasyona Yol Açan Yeni Bir Gen Mutasyonu Taşıyan BVVL Hastalarına Ait Indüklenmiş Motor Nöronların Oluşturulması

Deniz ATA

Hücresel ve Moleküler Tıp, Doktora

4 Şubat 2022

Brown-Vialetto-Van Laere sendromu (BVVL), nadir görülen ALS benzeri bir nörodejeneratif hastalıktır. BVVL semptomları sensorinöral işitme kaybı ve kranial sinir palsisi ile başlayıp sensörial ve kranyal sinir nörodejenerasyonu ile devam eder. Riboflavin transporter ailesi (RFVT/SLC52) proteinlerini kodlayan gen mutasyonları riboflavin yoksunluğu ve BVVL ile ilişkilendirilmiştir. İlginç olarak, altı kardeşten oluşan hasta grubumuzda *RFVT/SLC52* genlerinde mutasyon saptanmamıştır. Haplotip ve in siliko analiz ile desteklenen tüm ekzom dizilime sonucuna göre "Kinesin-like protein – KIF13A" proteinini kodlayan *KIF13A* geninde daha önce raporlanmamış bir saptanmıştır. Sağlıklı ve işleyen bir sinir sistemi için büyük öneme sahip olan KIF13A proteininin klatrin-bağımsız endosomal geri dönüşümde rol aldığı endozomal-lizozomal sistem için kritik role sahip olduğu bilinmektedir. Bu çalışmada, *KIF13A* geninde nörodejenerasyona sebep olan, daha önce raporlanmamış bir mutasyon taşıyan KU-BVVL hasta grubu için hasta spesifik indüklenmiş pluripotent kök hücre (iPKH) oluşturduk ve karakterizasyonunu tamamladık. Buna ek olarak, deneysel ihtiyaçlarımız doğrultusunda önceki çalışmaları temel alarak oluşturduğumuz küçük molekül bazlı farklılaşma metodu kullanarak "Glu1656Lys" *KIF13A* mutasyonu taşıyan hasta spesifik indüklenmiş motor nöronlar (iMN) oluşturduk ve karakterizasyonunu tamamladık. Oluşturulan iMN'lerde, KIF13A proteini yoğun şekilde bulunmakta olup, protein çoğunlukla soma ve dendritik bölgelerde gözlemlenmiştir. Bu durum göze alındığında KU-BVVL iMN hücre hatları hastalıklı fenotipi doğru şekilde yansıtan hücresel modeller olarak kullanılabilmektedir. Bunlara ek olarak, aralarında mutant ve yabanıl tip KIF13A-GFP, *KIF13A* hedefleyen CRISPR/CAS9 ve KIF13A-BioID füzyon rekombinant plasmidleri bulunan çeşitli plasmidler oluşturulmuş olup bunlar,

iMN’ler ile birlikte, KIF13A’nın dahil olduğu, sağlıklı ve işleyen sinir sistemi işe ilişkili moleküler işeleyişler üzerindeki önemini ortaya çıkaracak olan çalışmalarda kullanılacaktır.

ACKNOWLEDGMENTS

Firstly, I would like to thank my to thank Professor Tamer Önder for guiding the lost me through the relatively darkest period of my life (my first couple of terms of Ph.D.) and guiding me towards the best possible direction to reach the best possible outcome and help me harness my desire to contribute to science and society, Dr. Tuğba Bağcı-Önder who patiently and enthusiastically brain-stormed with me on my rather unconventional ideas and more importantly believing in me and my potential.

I want to thank Professor A. Nazlı Başak and Dr. Atay Vural to include me in their most promising research project and welcome me as if I am their lab member whenever I visit them or ask for guidance, and Dr. Bilal Kerman to bring optimism and show the better side of failings throughout the development of my thesis project.

Moreover, I would like to thank my current and previous colleagues and flatmates, who made Ph.D. more bearable for me, those people are; from my laboratory group “TO Lab” members Dr. Burcu Özçimen, Eray Enüstün, Dr. Deniz Uğurlu-Çimen, and Team Negar members, Dr. Alişan Kayabölen, Dr. Doğancan Özturan, Dr. Fidan Şeker-Polat, Dr. Uğur Akcan, Gizem Nur Şahin-Kayabölen, Göktuğ Karabıyık, Nareg Pınarbaşı-Değirmenci, and Özen Leylek for helping me whenever I needed. Including their support and help, my flat-mates deserve extra credit, specifically for Ali Cenk Aksu and Filiz Şenbabaoğlu being de facto parents of the household and Özen Leylek bringing camomile tea and optimism to the household even in the worst situations.

Lastly, I would like to thank my inherited and acquired family, especially my father Dr. Arif Ösün without whom I would be a wasted talent, a lost, wandering person without a purpose, Arda Ösün, Ayşe Mersin, Berk Coşardemir, Elif Bike Ösün-Coşardemir, Özlem Ösün, Dr. Hatice Arı, İdil Aydoğan, Başak Konuşur, Beril Arı, Bora Atar, Çağrı Deliler, Güneş Ünal, Selin Yalkut, and Tolga Atar for believing in me and their support.

Ethical Approval

This study was approved by Koç University Ethical Committee (2016.247.IRB2.119). Patients were informed prior to skin biopsy procedure, and patients signed written consent.

Funding

This project is funded by TUBITAK 1001 (1195398) fund and KUTTAM research funds.

Figures

Figures were created with “BioRender.com” and MS Office.

TABLE OF CONTENTS

TABLE OF CONTENTS

TABLE OF CONTENTS

TABLE OF CONTENTS

TABLE OF CONTENTS

LIST OF FIGURES

LIST OF FIGURES

LIST OF FIGURES

LIST OF FIGURES

List of Appendix Figures

LIST OF TABLES

LIST OF TABLES

LIST OF TABLES

ABBREVIATIONS

ABBREVIATIONS

AD	Alzheimer's Disease
ALS	Amyotrophic Lateral Sclerosis
BDNF	Brain-Derived Neurotrophic Factor
bFGF	Basic Fibroblast Growth Factor
BioID	Proximity dependent biotin identification
BirA*	Promiscuous BirA Ligase
BLOC-1	Biogenesis of Lysosome-related Organelles Complex 1
BLOC-2	Biogenesis of Lysosome-related Organelles Complex 2
BSA	Bovine Serum Albumin
BVVL	Brown-Vialetto-Van Laere Syndrome
C(T)	Treshold Cycle
cDNA	Complementary DNA
CHIR	CHIR99021
CNTF	Ciliary Neurotrophic Factor
CRISPR/Cas9	Clustered Regularly Interspaced Short Palindromic Repeats / CRISPR- associated protein 9
DANN	Deleterious Annotation of genetic variants using Neural Networks
dCas9	Deactivated Cas9
DCV	Dense Core Vesicle
DMEM	Dulbecco's modified eagle medium
DMH1	Dorsomorphin homolog 1
DMSO	Dimethyl sulfoxide
DNA	Deoxyribonucleic acid
DOX	Doxycycline
EBNA	Epstein–Barr nuclear antigen 1
EDTA	Ethylenediaminetetraacetic acid
EE	Early endosome
ESC	Embryonic stem cell
ESCRT-0	The endosomal sorting complexes required for transport 0
esMN	Early-stage motor neuron
FACS	Fluorescence-activated Cell Sorting
FAD	Flavin Adenine Dinucleotide

ABBREVIATIONS

FBS	Fetal Bovine Serum
FMN	Flavin Mononucleotide
FTD	Frontotemporal Dementia
GDNF	Glial cell line-Derived Neurotrophic Factor
GERP	Genomic Evolutionary Rate Profiling
GFP	Green fluorescent protein
gnomAD	The Genome Aggregation Database
HD	Huntington's Disease
HEK293T	Human Embryonic Kidney 293T
hESC	human Embryonic Stem Cell
HMI	Hypomelanosis of Ito
hr	hour
HRP	Horseradish Peroxidase
Hrs	Hepatocyte growth factor-Regulated tyrosine kinase Substrate
iDOt1L	Dot1L inhibitor (EPZ004777)
IF	Immunofluorescence
iMN	induced Motor Neuron
iPSC	Induced Pluripotent Stem Cell
KIF13A	KIF13A gene encodes kinesin-like protein 13A
KLD	Kinase-Ligase-DpnI enzyme mix
KO	Knockout
KOSR	KnockOut Serum Replacement
LE	Late Endosome
lsMN	late stage Motor Neuron
LTP	Long Term Potentiation
M6P	Mannose-6-Phosphate
M6PR	Mannose-6-Phosphate Receptor
MEF	Mouse Embryonic Fibroblast
MICAL1	Microtubule Associated Monooxygenase, Calponin And LIM Domain Containing 1
min	Minute
MN	Motor Neuron
MND	Motor Neuron Disorder
MNX1	Motor neuron and pancreas homeobox 1
MOI	Multiplicity of Infection
mRNA	messenger RNA

ABBREVIATIONS

MT	Mutant
MVB	Multivesicular Body
n.s.	not significant
NBM	Neurobasal Medium
NGN2	Neurogenin-2
NI	Neuronal Induction
NPC	Neural Progenitor Cell
NT	Non-Targeting
OE	Overexpression
OS	Oxidative Stress
OSKM	Oct4, Sox2, Klf4 and c-Myc
P/S	Penicillin/Streptomycin
PBS	Phosphate-buffered saline
PD	Parkinson's Disease
PEG	Polyethylene glycol
PFA	Paraformaldehyde
PMNC	Peripheral Blood Mononuclear Cell
PRM	Purmorphamine
PS	Proteamin sulfate
RA	Retinoic Acid
RAB11-FIP2	Rab11-family interacting protein 2
RE	Recycling Endosome
REC	Restriction Enzyme Cloning
RFVT	Riboflavin Transporter
RhoB	Ras homolog gene family member B
RNA	Ribonucleic acid
RNA-Seq	RNA Sequencing
ROCK	Rho-associated, coiled-coil containing protein kinase
ROS	Reactive Oxygen Species
rpm	revolutions per minute
RT	Room Temperature
RTD	Riboflavin Transporter Deficiency
RT-qPCR	Real-Time quantitative PCR
s.d.	Standard Deviation
s.err.	Standard error

ABBREVIATIONS

SB43	SB431542
SDM	Site-Directed Mutagenesis
sgRNA/gRNA	single guide RNA/guide RNA
SIFT	The Sorting Intolerant from Tolerant
SLC52	Solute Carrier family 52
SNV	Single Nucleotide Variation
SOC	Super Optimal broth with Catabolite repression medium
SVP	Synaptic Vesicle Precursor
TetON	The tetracycline-controlled Tet-On gene expression system
VPA	Valproic Acid
WB	Western Blot
WES	Whole-Exome Sequencing
WT	Wild Type
Y Compound	Y-27632
oriP	Origin of plasmid replication

CHAPTER 1: INTRODUCTION

1.1. Neurodegenerative Disorders

Neurodegenerative disorders are characterized by progressive dysfunction and loss of neurons and synapses in specific (vulnerable) populations of neurons of the nervous system. Many neurodegenerative diseases – including Amyotrophic Lateral Sclerosis (ALS), Alzheimer's Disease (AD), Frontotemporal Dementia (FTD), Huntington's Disease (HD), and Parkinson's disease (PD) – occur as a result of pathogenic (neurodegenerative) molecular mechanisms. The molecular mechanisms/processes inducing neurodegeneration are considered multifactorial caused by genetic, environmental, and endogenous factors related to aging.

The cause of neurodegeneration can be simply considered as harmful alterations of molecular pathways [1]. The common, interconnected molecular pathways underlying neurodegeneration include: (I) Impairment of protein quality control and abnormal protein dynamics; protein misfolding, aggregation, proteasomal dysfunction, and detrimental activity of chaperones and co-chaperones [2-10]. (II) Oxidative stress (OS) and formation of free radicals/reactive oxygen species (ROS); cellular damage, impaired DNA repair system, mitochondrial dysfunction caused by ROS [11]. (III) Mitochondrial dysfunctions and impaired bioenergetics, mitochondrial DNA damage, impairment of mitochondrial quality control and selective degradation of defunct mitochondria through mitophagy [12-23]. (IV) Autophagy, Endosomal – Lysosomal Pathway deficits and impairment of the downregulation bulk cytosolic contents macromolecules, protein aggregates, and damaged or excess organelles [4, 24-35]. (V) Aberrant membrane composition, synaptic toxicity, synaptic impairments, and network dysfunctions [36-39]. (VI) Disruption of cellular/axonal transport [40-46]. (VII) Altered levels of neurotrophins [47-50]. (VIII) Abnormal stress granules dynamics and stress granule aggregation [26, 29, 51-62]. (IX) Aberrant RNA metabolism [36-39]. (X) Maladaptive innate immune pathways and response [34, 37, 48, 63-74].

CHAPTER 1: INTRODUCTION

1.2. Classification of Motor Neuron Disorders

Motor neuron disorders are neurodegenerative diseases that are typically motor syndromes, primarily affecting motor neurons and motor units, not sensory neurons. MNDs show insidious onset; they are chronically progressive and can be caused by genetic mutations inherited (familial) or sporadic (non-hereditary mutations).

Motor neuron disorders (MNDs) can be broadly categorized in terms of affected cell type and affected region of the nervous system. MNDs can be further categorized in terms of weakness involved body region relative to the median plane (sagittal plane), symmetricity of it, and affection status of sensory neurons. MNDs can be decided to be distal, proximal, or mixed; and have different combinations of upper and lower motor neuron findings [75].

1.3. Brown Vialetto Van Laere Sydnrome (BVVL)

The Brown-Vialetto-Van Laere syndrome (BVVL) is a rare neurological disease that is characterized by progressive bulbar palsy, with sensorineural deafness. Bulbar palsy is a set of conditions that can occur due to degeneration of bulbar neurons, the lower cranial nerves that innervate the muscles of tongue movement, articulation, chewing, and swallowing, resulting in symptoms such as tongue atrophy, the thickness of speech (dysarthria), and difficulty swallowing (dysphagia) (Figure 1) [76-81]. The onset of the symptoms varies from infancy to the third decade, prevalently in the first decade, childhood. BVVL has ALS-like features and symptoms such as degeneration of both upper and lower motor neurons (collectively known as corticospinal neurons), which lead to muscle weakness and eventual paralysis. Two diseases diverge as BVVL most frequently characterized by progressive and sensorineural deafness, slurring of speech, facial weakness, respiratory compromise. Like ALS, neurodegeneration in BVVL begins focally then spreads to other parts of the nervous system, resulting in paralysis of other skeletal muscles, including respiratory muscles. BVVL is invariably fatal, with an average survival time of 10 years after the onset of their first symptom, although it is documented that several cases have survived 20–30 years.

CHAPTER 1: INTRODUCTION

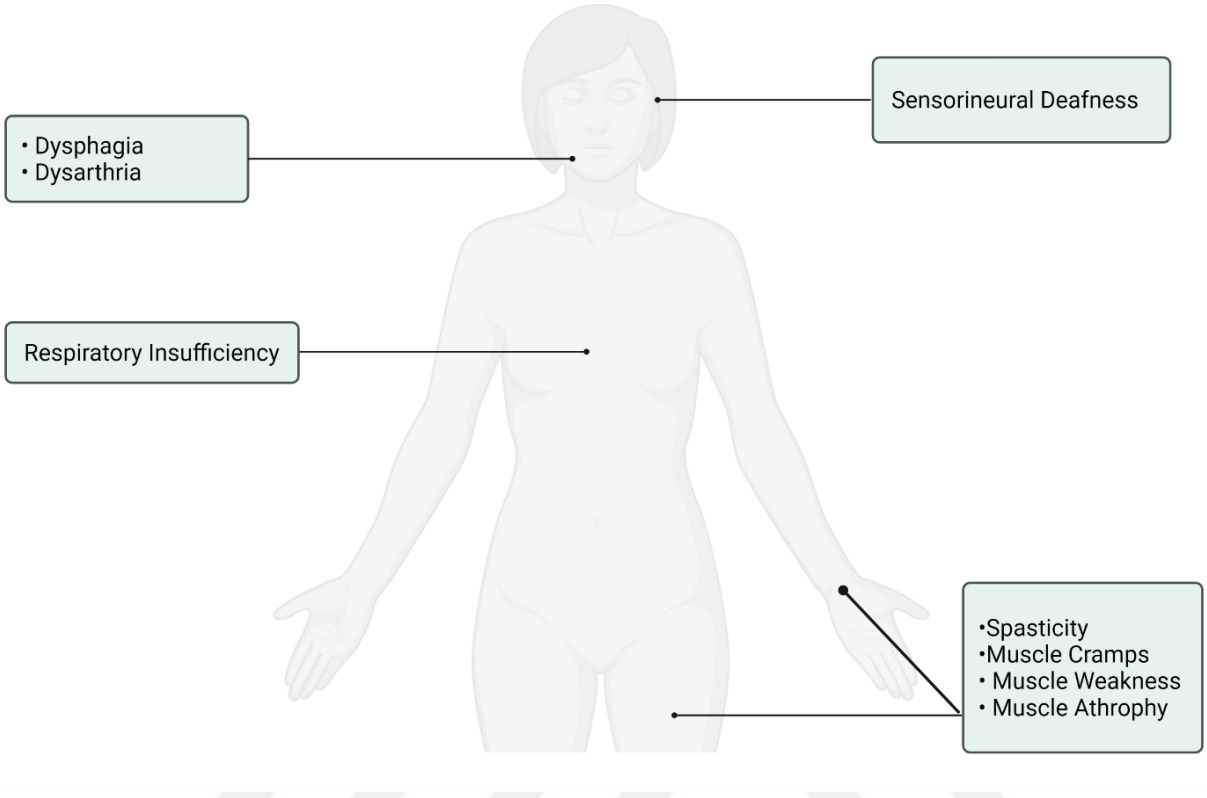

Figure 1: Clinical manifestations of BVVL. Clinical manifestations of BVVL include sensorineural deafness, the thickness of speech (dysarthria), difficulty swallowing (dysphagia)**.**

Molecular Genetics of BVVL

Although the unique clinical characteristics of the BVVL have been described at the end of the 1800s, the first clues regarding the genetic cause of BVVL were revealed when solute carrier family 52 (SLC52) member gene mutations were discovered in BVVL patients in 2010 and 2012 [82, 83]. Subsequently, it was discovered that SLC52 family proteins are responsible for dietary riboflavin uptake and transportation. Riboflavin (Vitamin B2) is the precursor of flavoproteins, flavin mononucleotide (FMN), and flavin adenine dinucleotide (FAD). Riboflavin is a key molecule in an aerobic cell since flavoproteins are crucial for mitochondrial function, oxidative phosphorylation, and oxidative stress reduction. Deficiencies in riboflavin uptake and transport result in mitochondrial dysfunction by reduced energy levels and oxidative stress reduction [84]. However, mutations in the SLC52 family genes are not found in a fraction of the patients who are clinically diagnosed with BVVL. In line with these, it was also discovered that high dose intravenous riboflavin application halted and, up to some point, reversed the

progression of neurodegeneration in BVVL patients. As a result, BVVL has become the first treatable ALS-like disease [85]. This finding suggests that there may be other genes involved in the pathophysiology of BVVL.

1.4. Patient Group – KU-BVVL

This thesis project was based on a family with six siblings; five out of six (one deceased) were clinically diagnosed with BVVL.

Four siblings (three male, one female) aged between 20-28 had generalized weakness and prominent pontopulbar palsy. Their parents were first cousins and did not have any neurologic symptoms. Patients have one healthy elder brother and one sibling who deceased at the age of 18 due to a similar condition and frequent infections. In all patients age of onset was around 12 years. They all had a history of slow progression that worsened significantly during infections or conditions that required high metabolic demand. On physical examination, all patients were cachectic and had a low body height. Neurological examination revealed ptosis, restricted eye movements, prominent bilateral facial palsy, mild sensory hearing loss, hypophonia, diminished gag reflex, and generalized mild weakness in extremities. Deep tendon reflexes were absent in all and there was extensor plantar response in two elder patients. Vibration sensation was diminished. Electromyography revealed widespread lower motor neuron denervation and nerve conduction studies were normal. Based on the findings of pontobulbar dominant generalized lower motor neuron disorder plus upper motor neuron findings, a diagnosis of Brown-Vialetto-van Laere (BVVL) syndrome was made. High-dose riboflavin treatment was started, and all the patients had a prominent positive response during the first year. The treatment response was limited; however, the patients' conditions were stable during eight years of follow-up.

No mutations were detected in *SLC52A2/3* genes with whole-exome sequencing. All patients responded favorably to riboflavin treatment and had marked improvements in their complaints. However, under four years of clinical follow-up, this improvement reached a plateau and was not adequate to stop disease completely, requiring additional treatment methods.

CHAPTER 1: INTRODUCTION

To identify the genetic mutation in this family; whole-exome sequencing (WES) and homozygosity mapping were carried out at the Koç University Suna and İnan Kıraç Foundation Neurodegeneration Research Laboratory (Figure 2).

The Genome Aggregation Database (gnomAD), formerly known as ExAC Database, was used to interpret data frequency and sort out single nucleotide polymorphisms [86]. The Genomic Evolutionary Rate Profiling (GERP) score was assessed to prioritize single-nucleotide variants that might be an evolutionary constrained and associated with the diseased phenotype. "The GERP score is defined as the reduction in the number of substitutions in the multi-species sequence alignment compared to the neutral expectation. For example, a GERP score of 4 would mean there are 4 fewer substitutions at a particular site than what is expected based on the neutral rate of evolution across the phylogeny" [87]. **D**eleterious **A**nnotation of genetic variants using **N**eural **N**etworks (DANN) uses machine learning to develop its algorithm and generates a list of functional vs. non-functional variations. DANN uses a scoring system between 0 and 1, with 1 annotating the pathogenic variant [88]. The Sorting Intolerant from Tolerant (SIFT) algorithm predicts the adverse effect of a coding variant by computing the new composition of amino acids. SIFT score ranges from 0 to 1, and a value between 0 and 0.05 is predicted to affect protein function [89]. One candidate gene, *KIF13A*, encoding Kinesin-3 family member KIF13A protein, with a possible pathogenic single nucleotide variation (SNV) was detected. The detected SNV results in amino acid change "pGlu1656Lys". High GERP score of 6.0799 suggests that this variation might be in an evolutionary constrained site. In addition, the DANN algorithm labelled this variant as non-functioning, and the effect of this variation was reported as damaging (adversely affecting the protein function) in SIFT predictive model (Figure 3, Table 1).

ID	Gene	Nucleotide Change	Change Consequence	The Frequency at gnomAD (ExAC) Database	GERP Conservation Score	DANN Score	SIFT Prediction
KU-BVVL (BVVL-1)	KIF13A	c.4966G>A	p.Glu1656Lys	0,0000494	6,0799	0,9983	Damaging

Table 1: WES and in silico analysis result. In silico analysis resulted in a new candidate gene mutation on KIF13A.

CHAPTER 1: INTRODUCTION

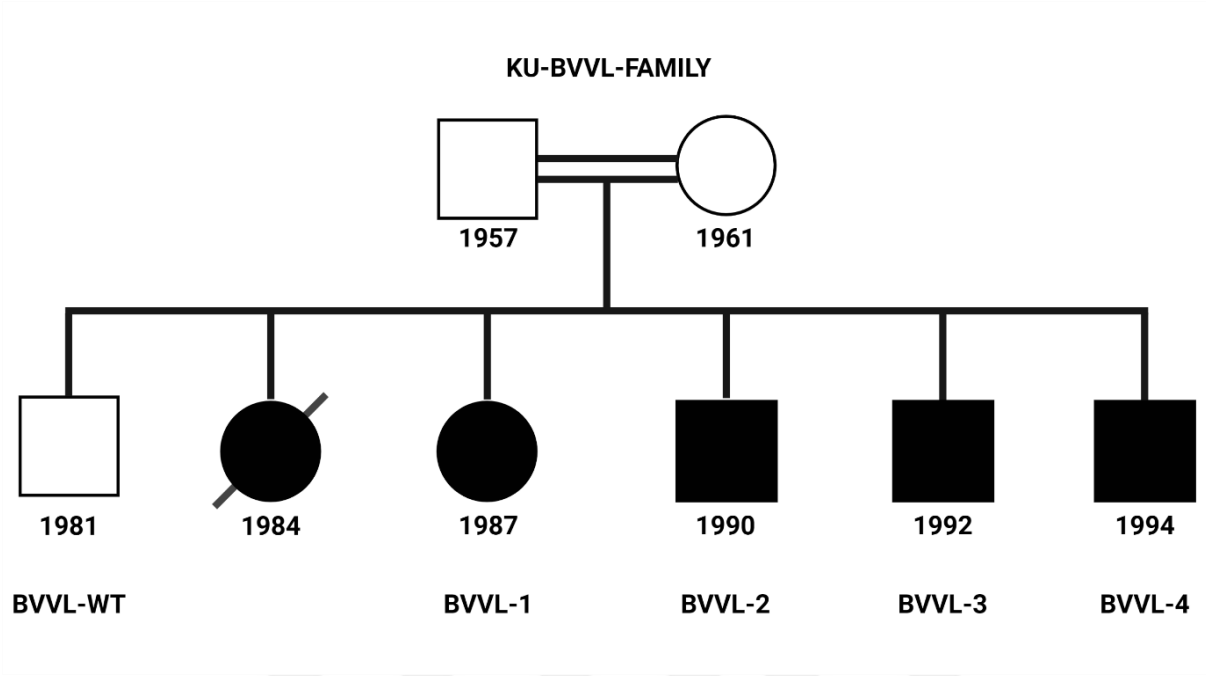

Figure 2: KU-BVVL Family pedigree. Five out of six siblings (one deceased) were clinically diagnosed with BVVL.

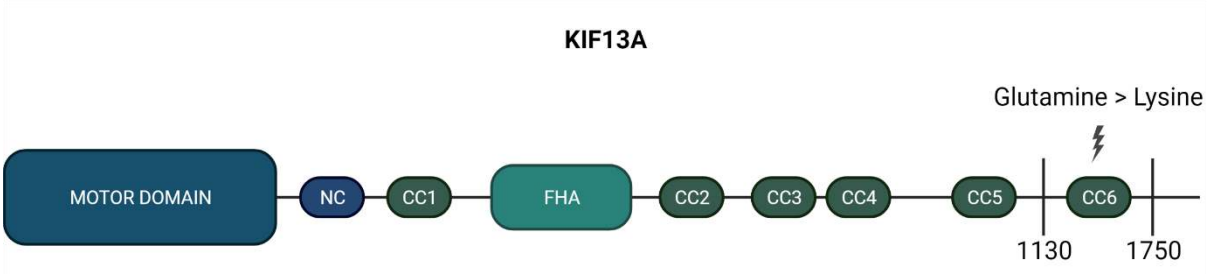

Figure 3: Domain map of KIF13A Protein. Location of Glutamate > Lysine SNV on KIF13A protein is near the CC6 domain. FHA: forkhead-associated domain. NC: Neck domain CC: Coiled-coil domain, FHA: Forkhead-associated domain.

CHAPTER 1: INTRODUCTION

1.5. Kinesin Motor Proteins & The Endosomal – Lysosomal System

The kinesin superfamily is a large family of kinesin motor proteins, with more than 45 members divided into 14 families. Kinesin motor proteins are one of the major actors in intracellular cargo transport as well as microtubule organization and dynamics regulation. Kinesin motor proteins consist of a motor domain that directs movement along microtubules and a tail domain that interacts with cargo [90]. The activity of kinesin motor proteins is ATP-dependent as their motor domains hydrolase ATP to drive movement along microtubules [91].

The Endosomal - Lysosomal system (also known as endo-lysosomal system) can be defined as “a series of organelles in the endocytic pathway” where various cargo molecules, including defunct/damaged organelle and proteins that went through autophagy for timely clearance or membrane receptors and neurotransmitters required for normal cellular function are internalized, recycled, and modulated [92, 93]. The Endo-lysosomal system is comprised of early endosomes (EE), recycling endosomes (RE), late endosomes (LE), autophagosomes, and lysosomes. The highly dynamic system is mediated by Kinesins and Rab guanosine triphosphates (Rab GTPases), as kinesins mediate cargo transport along microtubules and Rab GTPases recruit molecular motors, organize and identify the endosomes [94-102]. The Endo-lysosomal system and its components are essential for a healthy, functioning nervous system as they are essential to maintain membrane composition and cellular homeostasis.

Malfunction in the endo-lysosomal system has been implicated in developmental disorders, aging, cancer, and neurodegeneration. As key components of microtubule organization, endo-lysosomal system, and vesicular system, kinesin motor proteins are also implicated in cancer, developmental disorders, neurodegenerative diseases and disorders. These include Alzheimer’s Disease, Autism Spectrum Disorders, Joubert Syndrome, Microcephaly, and Spastic Paraplegia (Table 2) [102-121].

CHAPTER 1: INTRODUCTION

1.6. Kinesin-like protein 13A – KIF13A

KIF13A gene encodes kinesin-like protein 13A (KIF13A), a member of the kinesin-3 family. KIF13A is known to play a major role in the endosomal – lysosomal system by mediating the clathrin-independent endosomal recycling, closely interacting with $Rab10^+$, $Rab11^+$, $Rab22^+$ vesicles. Important cargo of KIF13A regarding the nervous system includes hepatocyte growth factor-regulated tyrosine kinase substrate (Hrs) vesicles, serotonin type 1a receptor, transferrin receptor, and AMPARs [102, 107, 122-125].

Endosomal recycling of receptors is essential to synaptic function and plasticity, as well as cellular homeostasis of the nervous system. Internalized receptors may be directed to lysosomal degeneration or revert to the plasma membrane from recycling endosomes. In addition, Recycling endosomes also serves as submembrane reserve pools that modulate long-term potentiation (LTP) [112, 126-135].

It has been established that KIF13A is an important player in the endosomal – lysosomal system. The importance of KIF13A for a healthy, functioning nervous system becomes more apparent as knowledge on KIF13A interaction partners improves and KIF13A's involvement in critical cellular processes is revealed.

In a recent study by Gutierrez et al., it has been revealed that KIF13A is responsible for the remodelling of Rab11-family interacting protein 2 (RAB11-FIP2) endosomal structures during LTP and is essential for the delivery of AMPARs to the dendritic spine surface during long-term potentiation induction [125]. KIF13A is also shown to transport serotonin type 1a receptor to the dendritic membrane [107]. Both studies could indicate that a deficiency of KIF13A could lead to neurodegeneration through aberrant membrane composition, synaptic toxicity, synaptic impairments, and network dysfunctions [36-39].

In another preprint study, Birdsall et al. revealed that KIF13A is essential for activity-dependent transport of "the endosomal sorting complexes required for transport 0" (ESCRT-0) component Hrs+ vesicles. Hrs is essential for sorting proteins into the ESCRT pathway and downstream ESCRT machinery to catalyse multivesicular body (MVB) formation. In addition,

CHAPTER 1: INTRODUCTION

Birdsall et al. identified kinesin motor protein KIF13A as essential for the activity-dependent transport of Hrs to synaptic vesicle pools and the degradation of synaptic vesicle membrane proteins. Furthermore, their data demonstrated a novel activity- and KIF13A-dependent mechanism for mobilizing axonal transport of ESCRT machinery to facilitate the degradation of SV membrane proteins [136].

Although KIF13A was only shown to transfer mannose-6-phosphate receptors (M6PR) to the cell surface in T cells, this finding could also indicate the possibility of KIF13A dependent transport of M6PR, which is essential for lysosome biogenesis [137]. In addition, KIF13A is shown to be co-localized with the biogenesis of lysosome-related organelles complex 1 (BLOC-1) and 2 (BLOC-2) [100, 102]. These findings further support Birdsall et al.'s findings and bolster the importance of KIF13A on multivesicular body (MVB) formation, lysosomal biogenesis, and autophagy. Neurodegeneration could be an outcome of KIF13A deficiency caused by autophagy, endosomal – lysosomal pathway deficits, and impairment of the downregulation bulk cytosolic contents macromolecules, protein aggregates, and damaged or excess organelles [4, 24-35].

RE tubule morphogenesis mechanism explained using the "tug-of-war" model. This model suggests that tubular endosome elongation and fission is a result of "tug-of-war" like activity of opposite-polarity motors, kinesin(s), and dynein(s) [102, 138, 139]. Etoh et al. revealed that kinesin involved in this mechanism is KIF13A and is indispensable for RE tubule morphogenesis, as tubular elongation diminished in KIF13$^{-/-}$ cells [101]. Broken equilibrium in this "tug-of-war" towards one side could affect downstream RE trafficking and lead to neurodegeneration through deficiency in multiple critical molecular pathways for neuronal survival.

KIF13A's involvement in transferrin receptor transport should not be neglected, as abnormal transferrin dynamics are shown to lead to neurodegeneration [102, 122-124].

In a recent case report, a Hypomelanosis of Ito (HMI) patient carrying heterozygous frameshift variant, KIF13A c2357dupA was identified. The said mutation results in nonsense-mediated decay of the KIF13A mRNA. Structural abnormalities were detected in the patient magnetic resonance imaging. As a case report, this study did not pursuit the underlying molecular

mechanism of the diseased outcome, but Gong et al.'s study on KIF13A role on RhoB plasma membrane localization indicate developmental abnormality is a result of defunct K1F3A regulation of cell membrane blebbing and migration of neural crest cells through recycling of small GTPase, Ras homolog gene family member B, (RhoB) to the plasma membrane [116, 140].

The activity of KIF13A is regulated through an autoinhibitory mechanism predominantly mediated by the Rab22A and coiled-coil – 1 segment of the protein. KIF13A functions as weak dimers and like many other kinesins, adopt an autoinhibitory conformational state which restricts the dimerization of the protein and ATP hydrolysis of its motor domain. KIF13A adopts an autoinhibited conformational state in which the autoinhibitory coiled-coil 1 segment associates with both the neck and motor domains, tightly fastens them together, and locks down the entire neck domain. This inhibits both the neck domain-mediated dimerization and the ADP release from the motor domain. It is known that the autoinhibition mechanism works in the absence of Cargo or Rab22A in case of KIF13A, limiting excess ATP hydrolysis of idle KIF13A [102, 141, 142].

Name of the Motor Protein	Family	Function(s)	Related Disease and Disorder	Reference
KIF-5	Kinesin-1	Axonal Transport, SOD1 Transport	ALS	Reid et al. 2002 Shi et al. 2010 López et al. 2015 Bougé & Parmentier 2016 Brenner et al. 2018 Nicolas et al. 2018
KIF-21B	Kinesin-4	Metaplasticity, GluN2B-NMDAR Local Recycling	Autism Spectrum Disorders	Gromova et al. 2018
KIF-7	Kinesin-4	Sonic Hedgehog signaling, Microtubule Dynamics	Joubert Syndrome	Dafinger et al. 2011
KIF-11	Kinesin-5	Nervous System Development	Microcephaly	Ostergaard et al. 2012
KIF-1A	Kinesin-3	The long-distance transport of synaptic vesicle precursors (SVPs) and dense core vesicles (DCVs).	Spastic Paraplegia	Hotchkiss et al. 2016 Yoshikawa et al. 2019
KIF13A	Kinesin-3	Serotonin Type 1A Receptor Transport to the membrane	$KIF13A^{-/-}$ mice exhibit elevated anxiety-related behavioral phenotypes	Zhou et al. 2013
KIF13A	Kinesin-3	Regulation of cell membrane blebbing and migration of neural crest cells through recycling of RhoB to the plasma membrane. Melanosome biogenesis.	Hypomelanosis of Ito	Lam et al. 2021

Table 2: Kinesin motor proteins and related disease and disorders.

CHAPTER 1: INTRODUCTION

1.7. Induced Pluripotent Stem Cells

Stem cells are undifferentiated or partially differentiated cells of multicellular organisms. Stem cells are characterized by their ability to proliferate indefinitely to produce more of the same stem cell and their capacity to differentiate into various types of cells [143].

Stem cells are broadly divided into two main categories called adult and embryonic stem cells (ESCs). Adult stem cells can give rise to a limited number of mature cells (referred to as somatic cells) for wound healing or regeneration of organs and tissues (for example, hematopoietic stem cells can only differentiate into blood cells). Embryonic stem cells (ESC), the cells of the inner cell mass, give rise to all types of cells, which eventually become the adult organism. Even a single stem cell can give rise to a functioning tissue or an organ via a process called differentiation. However, a stem cell's differentiation capacity is limited as the more a stem cell dedicates itself to differentiate into a cell with a specific function, the more it loses its potential to differentiate to other types of cells.

1.7.1. The Potency of Stem Cells

During vertebrate embryonic development, cells of the inner cell mass form three primary layers of cells, which give rise to all an animal's organs and tissues. These three germ layers are named endoderm, mesoderm, and ectoderm. The potential to differentiate into the cells of the three germ layers is referred to as pluripotency. Being able to differentiate into cells of the three germ layers is the hallmark of pluripotency (Figure 4).

1.7.2. The iPSC Technology

Induced pluripotent stem cells (iPSCs) are a type of pluripotent stem cells that are generated directly from a somatic cell. Somatic cells can acquire embryonic stem cell-like pluripotency with the introduction of four specific genes (c-Myc, Oct3/4, Sox2, and Klf4), collectively known as **Yamanaka factors** [144]. iPSCs prove to be a valuable tool in disease modeling and personalized medicine studies as the genome of induced pluripotent stem cells (iPSCs) are

identical to the source organism, and “pluripotent” stem cells can be virtually differentiated into every cell line. Human iPSCs can be safely and efficiently differentiated into neurons and subtypes of neurons to develop and use as models of neurodegenerative diseases, which are otherwise impossible to obtain.

1.7.3. Somatic Cell Source for iPSC Generation

iPSCs can be generated from different types of somatic cells, including fibroblasts, keratinocytes, cord blood cells, peripheral blood mononuclear cells (PMNCs). Although peripheral mononuclear cells (PMNCs) are the most attractive source to use for generation iPSCs because of the low invasiveness of their collection, dermal fibroblasts (skin fibroblasts) serve as a more stable somatic cell source. Fibroblasts can be cultured and stored for extended periods with ease, and patient-specific fibroblasts can serve as a model for simple experiments as well as proof of concept experiments. Thus, the reprogramming of dermal fibroblasts is a more feasible and failsafe approach of iPSC generation, with fewer drawbacks, compared to reprogramming of peripheral blood mononuclear cells (PMNCs) [145-147].

1.7.4. Reprogramming: iPSC Generation

Reprogramming is conducted with the introduction of **Yamanaka factors**. Delivery methods of Yamanaka factors (reprogramming factors) include transfection, nucleofection, viral vector delivery (lentiviral, retroviral, Sendai virus), and mRNA-based genetic reprogramming. Except for the Sendai virus, the use of viral vectors leads to random integration of exogenous DNA into the genome. For disease modelling studies, this may disrupt the functionality of the important genes and hinder efforts to model or discover pathways that cause the disease. In addition, the integration of exogenous DNA into the tumor suppressor genes may also disrupt the functionality of tumor-suppressor genes, therefore, leading to tumor formation or may cause safety problems in possible therapeutic applications. Nucleofection eliminates the use of retro- or lentivirus for Yamanaka factor introduction, reprogramming via nucleofection is considered to be integration-free, meaning that genomic integrity of cells is not affected, and cells/tissues/organs that are derived from those iPSCs are safe to study without loss of gene function and safe for transplantation [148].

CHAPTER 1: INTRODUCTION

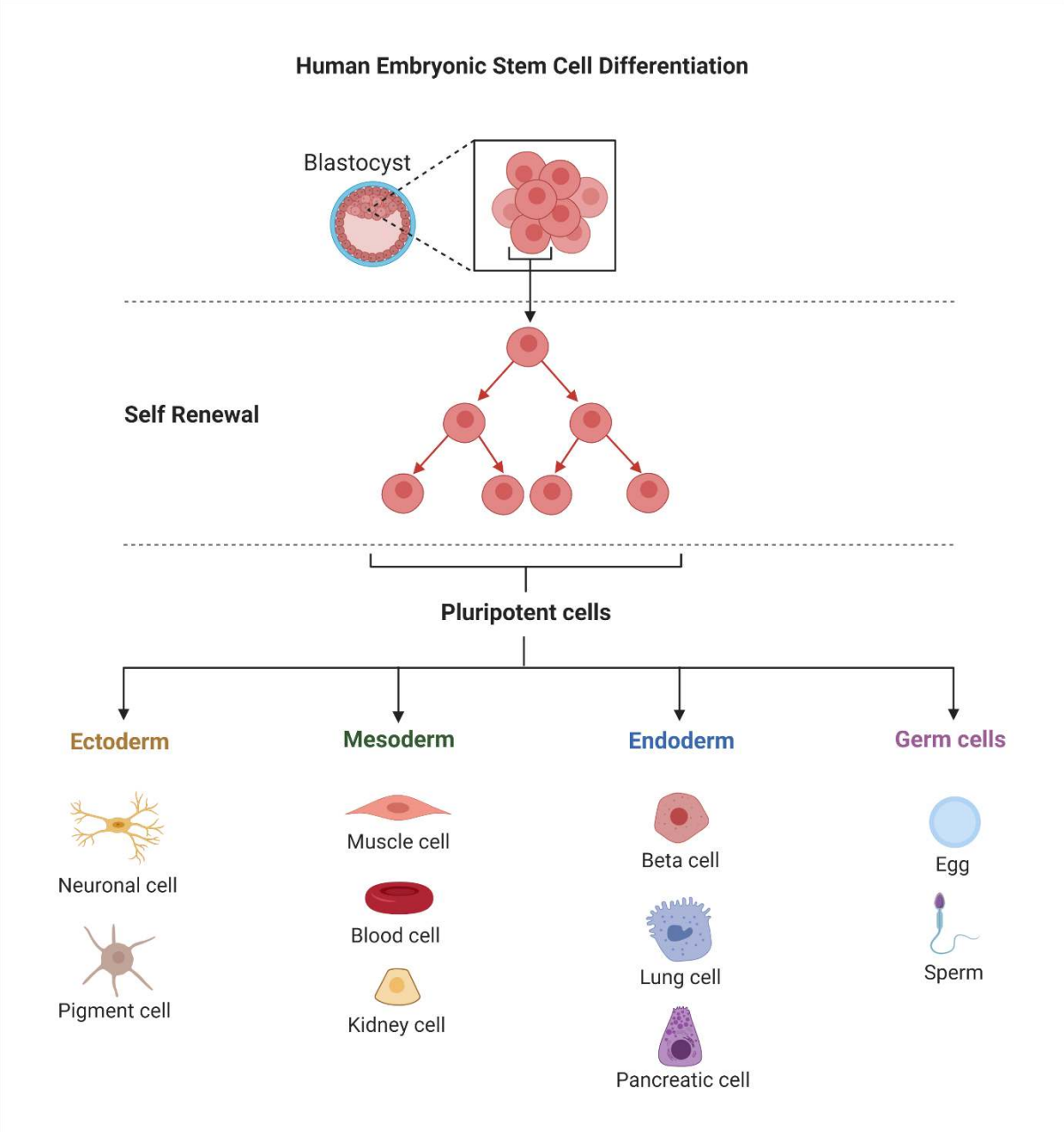

Figure 4: Human embryonic stem cell differentiation. Both ES and iPSCs are pluripotent, meaning that they can virtually differentiate into all other cell lines (Adapted from "Human Embryonic Stem Cell Differentiation", by BioRender.com (2021). Retrieved from https://app.biorender.com/biorender-templates).

CHAPTER 1: INTRODUCTION

1.8. ES & iPSC Based Disease Modeling

In vitro model cell lines were mostly limited to primary cell cultures and immortalized cell lines before the development of embryonic stem cell culture. This limitation has hindered efforts to understand the molecular basis of many diseases due to the generation of appropriate model cell lines that accurately reflect disease phenotypes lacked. iPSCs provide a basis for the ideal in vitro cell culture models as the genome of iPSCs are identical to the genome of the host organism and can be virtually differentiated into any other cell line and can be expanded indefinitely. Importantly, iPSCs that carry disease-causing mutation can be differentiated into in vitro model cell lines and tissues that accurately reflect disease phenotype, including cell lines and tissues that normally cannot be taken samples of from human patients, such as the nervous system. As understanding of cellular differentiation increased, more accurate models of in vitro cell cultures that accurately reflect disease phenotypes were generated. These two advancements led to the golden age of disease modelling and personalized medicine.

CHAPTER 1: INTRODUCTION

1.9. In vitro models of Motor Neuron Diseases

In recent years, studies conducted to understand the molecular basis of neurodegenerative diseases shifted towards iPSCs, and iPSC derived in vitro cell cultures and organoids. According to National Health Services UK, there are more than 600 neurological diseases and disorders. Studying those diseases and disorders brings hope for the future of medicine and sheds light on a wide range of molecular processes. Many neurodegenerative diseases are being studied using iPSCs and neurons derived from iPSCs, including common neurodegenerative disorders such as Acute Lateral Sclerosis, Alzheimer's Disease, Parkinson's Disease, and rarer disorders such as Brown-Violetto-Van Laere Syndrome and Friedreich Ataxia [149-153].

BVVL was not intensely studied as ALS due to the fact that it is a very rare disease compared to ALS. There are not many studies on BVVL, and hardly any BVVL studies include ESCs, iPSCs, and induced neuron lines. The first iPSCs from BVVL patients were generated by Rizzo et al. in 2017. In that study, iMNs derived from iPSCs generated from BVVL patients carrying SLC52A2 or SLC52A3 mutations. In that study, a reduction in axon elongation coupled with perturbations in neurofilament composition and reduced autophagic/mitophagic flux was observed [154]. In a recent study, Marioli et al. (2020) iMNs derived from iPSCs generated from BVVL patients carrying SLC52A2 or SLC52A3 mutations. In that study, possible beneficial effects of several antioxidants Vitamin C, Idebenone, Coenzyme Q10 and EPI-743, either alone or in combination with riboflavin on the morphology and function of motor neurons derived from iPSCs generated from BVVL patients carrying SLC52A2 or SLC52A3 mutations [155]. Due to the limited literature on BVVL consisting of iPSC and iMN based studies and the similarity of the symptoms with ALS, studies on ALS could be taken into consideration. Those studies could be valuable guides to study KIF13A protein's involvement in crucial biological processes and molecular pathways that are crucial for a healthy, functioning nervous system (Table 3) [150, 154-171].

CHAPTER 1: INTRODUCTION

1.10. Motor Neuron Differentiation Methods in Literature

Forced Expression of Exogenous Transcription Factors

In vitro cell engineering offers tremendous potential not only for the investigation of molecular pathways and diseases but also for cell-based transplantation therapies and therapeutic applications. Transcription factors were extensively studied to unlock this potential, and pioneering works in 1987 and 2006 showed that cell identity could be altered, and cell fate can be reversed with the forced expression of transcription factors. Somatic cells can be **trans**differentiated into somatic cell lines or reprogrammed into pluripotent stem cells via forced expression of exogenous transcription factors [144, 172-174]. Relatively straightforward, forced expression of exogenous transcription factors eliminates the restriction to stem cells for the generation of neurons [173]. In addition, forced expression of exogenous transcription factors has been a practical approach in producing specific subtypes of neurons, including motor neurons, dopaminergic neurons, sensory neurons, and striatal neurons [175-178].

Although their use is not essential, ESCs or iPSCs can be used as the initial cell source to increase differentiation efficiency as ESCs and iPSCs are in a naiver state since they contain fewer epigenetic barriers for differentiation.

Many somatic cells and stem cells cannot be transduced efficiently, and the use of retroviral and lentiviral vectors bear the risk of the integration of exogenic DNA into a critical genomic region. In addition, forced expression of multiple viral constructs contains two other hurdles to be considered; dosing and efficient transduction of multiple constructs which are used simultaneously. The use of Sendai virus (Murine respirovirus) transduction, nucleofection, and synthetic mRNA-based forced expression methods can eliminate the risk of integration.

CHAPTER 1: INTRODUCTION

Targeted Transcription Factor Activation for Neuronal Differentiation

Instead of overexpressing the exogenous copies of transcription factors, endogenous transcription factors can be activated with the CRISPR-Cas9 system to (trans-)differentiate somatic cells or stem cells into neurons. Differentiation is achieved with the selective activation of key transcription factors with catalytically deactivated Cas9 (dCas9) and transcriptional activators such as VPR and VP64 fused to it. Multiple sgRNAs can be utilized to activate multiple transcription factors simultaneously, thus allowing (trans-)differentiation into cell lines whose fate is determined by multiple transcription factors [174, 179-191].

Differentiation into neurons can be achieved by targeted activation of NEUROG2 gene encoding Neurogenin-2 and NEUROD1 gene encoding Neurogenic Differentiation 1 transcription factors using dCas9-VPR with a lentiviral pool of gRNAs targeting the aforementioned genes [187, 192]. This relatively new approach virtually enables the production of specific subtypes of neurons without the exogenous transcription factor overexpression [193]. However, the design of robust gRNAs and more potent dCas9-fused activators, such as VPR, are required to achieve similar differentiation efficiency as transcription factor overexpression methods [194].

Small-Molecule-Based Differentiation

Stem cells can be differentiated into neurons via small-molecule-based differentiation methods. The differentiation relies on the addition of the small molecule combinations into the culture medium, which regulate key signaling pathways. With the flexibility of using different combinations of transcription factor modulators at different time points, small-molecule-based methods enable the generation of more specific subtypes of neurons and glia. ESCs and iPSCs can be efficiently differentiated into neural progenitor cell populations via Dual SMAD inhibition. BMP and TGF-B signaling pathways utilize SMADs for transduction. Dual SMAD inhibition, inhibition of both pathways lead to rapid differentiation of pluripotent stem cells into neural progenitor cells (NPCs). NPCs can be further differentiated into specific neuronal subtypes by inhibiting signaling pathways such as GSK-3β, Hedgehog, Notch, and TGFβ [193, 195-197].

This method requires potent stem cells but eliminates the use of viral constructs for differentiation. Thus, eliminate the need for an appropriate biosafety infrastructure, labor for viral packaging, and optimization to achieve standardization of the differentiation method between new differentiation series.

The following subjects could be considered prior to beginning a disease modeling study to achieve model cell lines that accurately reflect motor neuron disease phenotypes:

Disruption of the genomic integrity may result from the use of lentiviral and retroviral vectors. Except for the Sendai virus, the use of viral vectors leads to random integration of exogenous DNA into the genome. For disease modeling studies, this may disrupt the functionality of the important genes and hinder efforts to model or discover pathways that cause the disease. Non-integrating methods of gene delivery could be used for forced expression of transcription factors and targeted transcription factor activation for neuronal differentiation methods. This is not a concern in small-molecule-based differentiation methods cross this hurdle as no exogenous genetic material is used in this method.

Using the correct cell line is crucial to disease modeling studies. Although present in the genome, mutations that cause diseased phenotype are not expressed or not as crucial as to some neuronal subtypes of neurons and glia. Thus, neurodegenerative diseases take a toll on a specific subset of neurons and glia while sparing others.

The purity of the cell population is another concern in the accurate modeling of neurodegenerative diseases. Although highly efficient, differentiation methods are not 100% efficient, and disease-causing gene mutations may further lower differentiation efficiency or cause premature death of cells interest in the bulk population of cells. Population heterogeneity may cause inaccurate reflection of diseased phenotype and result in variations between experimental replications.

The level of representation of the diseased phenotype also varies between cells, as each cell is at a different stage of differentiation/maturation and disease progression. Fluorescence-activated cell sorting (FACS) can be used to purify specific subtypes of neurons and glia.

However, cellular heterogeneity remains in terms of disease progression as it is unlikely to initiate synchronized differentiation of all cells. On the other hand, population heterogeneity can be exploited by profiling gene expression within individual cells and using high content imaging. These methods allow researchers to study each “patient” cell individually to identify the progression of disease-relevant processes [152, 198, 199].

Neurotrophic Factors are used to improve the survival rate and efficiency of neuronal differentiation, neurotrophic factors, such as brain-derived neurotrophic factor (BDNF), ciliary neurotrophic factor (CNTF), glial cell line-derived neurotrophic factor (GDNF), may provide a comfortable micro-environment to study neurodegeneration. The combined effect of neurotrophic factors may prolong survival time and obscure early markers of degeneration. Thus, they should be withdrawn from the medium for a certain amount of time before initiating functional experiments.

CHAPTER 1: INTRODUCTION

1.11. Main Question Adressed

KIF13A is an important player in the endosomal – lysosomal system. The importance of KIF13A for a healthy, functioning nervous system becomes more apparent as knowledge on KIF13A interaction partners improves and KIF13A's involvement in critical cellular processes is revealed. However, its importance to neuronal survival remains unexplored.

I hypothesize that c.4966G>A mutation in the *KIF13A* gene, encoding Kinesin-like motor protein 13A, alters protein-protein interaction dynamics, resulting in vesicular trafficking deficiency of an important cargo for cellular homeostasis, and lead to neurodegeneration in patients diagnosed with The Brown-Vialetto-Van Laere syndrome. To address this question, I generated iPSCs and iPSC-derived motor neuron from patients carrying KIF13A mutations as well as healthy controls.

Table 3: ALS studies based on patient specific induced motor neurons. (adapted from Hawrot et al. 2020).

Reference	*Type of Study*	*Differentiation Method*	*Date of Analysis (After Diff.)*
Burkhardt et al. 2013	ALS Disease Modelling - Screen of 1757 compounds	Small Molecule Based – 18 Days	Days 7, 25, 32, 97, 104
Fujimori et al. 2018	ALS Disease Modelling - Screen of 1232 compounds	Small Molecule Based – 19 Days	Days 5-50 Day 31
Imamura et al. 2017	ALS Disease Modelling - Screen of 1416 compounds	Forced Expression of Transcription Factors - 7 days	Day 7
Marrone et al. 2018	ALS Disease Modelling - Screen of ~1000 compounds	Small Molecule Based – 6 Days	Day 21
Shi et al. 2018	ALS Disease Modelling - Screen of 800 compounds	Forced Expression of Transcription Factors - 15 days	Days 0-10 longitudinal
Bhinge et al. 2017	ALS Disease Modelling - Candidate evaluation based on pathways identified by RNA-seq	Small Molecule Based – 10 Days	Day 20, 34
Egawa et al. 2012	ALS Disease Modelling - Candidate evaluation based on pathways identified by RNA-seq	Small Molecule Based – 35 Days	Day 22
Guo et al. 2017	ALS Disease Modelling - Candidate evaluation based on Charcot Marie Tooth and SOD1 mouse studies	Small Molecule Based – 9 Days	Days 15, 22, 29
Kiskinis et al. 2014	ALS Disease Modelling - Candidate evaluation based on pathways identified by RNA-seq	Small Molecule Based – 24 Days	Days 3, 15, 21, 30
Lopez-Gonzalez et al. 2016	ALS Disease Modelling - Candidate evaluation based on pathways identified by oxidative stress and DNA damage	Small Molecule Based – 31 Days	Days 14, 28, 56, 84, 120
Naujock et al., 2016	ALS Disease Modelling - Candidate evaluation based on mechanism of hypoexcitability	Small Molecule Based – 52 Days	Day 11-18, 22, 32-39, 81-88
Naumann et al. 2018	ALS Disease Modelling - Candidate evaluation based on pathways identified by DNA damage	Small Molecule Based – 9 Days	Days 0, 5, 12, 21, 26, 47, 51, 101
Wainger et al. 2014	ALS Disease Modelling - Candidate evaluation based on mechanism of hyperexcitability	Small Molecule Based – 24 Days	Days 4, 8, 12, 16, 20, 24, 28, 30
Bianchi et al. 2018	Neural Injury Modeling	Small Molecule Based – 35 Days	Day 35
Du et al. 2014	Differentiation of Specific Motor Neuron Subtypes	Small Molecule Based – 28 Days	Days 6, 12, 18, 28
Qu et al. 2014	Investigation of Islet-1 Function on Motor Neuron Differentiation	Small Molecule Based – 20 Days	Days 1, 2, 3, 4, 5, 6, 9, 20
Rizzo et al. 2017	Genome-wide RNA-Sequencing	Small Molecule Based – 24 Days	Day 32
Marioli et al. 2020	Investigation of Antioxidant Amelioration of Vitamin C, Idebenone, Coenzyme Q_{10}, EPI-743, Riboflavin	Forced Expression of Transcription Factors - 21 days	Day 21

CHAPTER 2: MATERIALS AND METHODS

2.1. Molecular Cloning Experiments

2.1.1. Competent Bacteria Preparation

Competent Bacteria preparation protocol was adapted from Hanahan et al.'s method [200]. STBL3 strain *E. Coli* were spread on an antibiotic-free LB agar plate and incubated at 37^{O}C for 18hr to form colonies. A single bacteria colony was picked and cultured in 2ml LB broth overnight at 37^{O}C overnight in a bacterial shaker (225rpm). The following day, approximately 12hr later, 0.5ml of the suspension was added on 100ml of fresh LB broth (BD). The bacterial suspension was incubated at a 37^{O}C bacterial shaker for 3hr. During incubation, the optical density of the bacterial suspension was measured at the wavelength of 600nm (OD600) regularly with 30-minute intervals to assess if the bacteria is at the logarithmic phase, the growth phase characterized by cell doubling. When the OD600 value reaches 0.4 to 0.6, the bacterial suspension was incubated on ice for 15min and centrifuged at 3000rpm 4^{O}C for 15min. The bacterial pellet was resuspended with 33ml of ice-cold RF1 buffer and incubated on ice for 15min. The bacterial suspension was centrifuged the same as the previous step, and the bacterial pellet was resuspended with 8ml of ice-cold RF2 buffer. RF2 bacterial suspension was aliquoted into 1.5ml microcentrifuge tubes as 100µl aliquots and snap-frozen using liquid nitrogen. The bacterial suspensions were stored in -80^{O}C. RF1 and RF2 buffers were specified in Table 4 and Table 5, respectively.

CHAPTER 2: MATERIALS AND METHODS

RF1 Buffer		
	Amount	Final Concentration
RbCl	12 g	100 mM
MnCl2.4H2O	9.9 g	50 mM
CH3CO2K	30 ml from 1M stock	30 mM
CaCl2	1.1 g	10 mM
Glycerol	150 g	15% (w/v)
dH2O	-	up to 1 L
pH was adjusted to 5.8 with 0.2 M CH3COOH		

Table 4: RF1 Buffer components.

RF2 Buffer		
	Amount	Final Concentration
MOPS	20 ml of 0.5 M stock	10 mM
RbCl2	1.2 g	10 mM
CaCl2	8.25 g	75 mM
Glycerol	150 g	15% (w/v)
dH2O	-	up to 1 L
pH was adjusted to 5.8 with 0.2 M CH3COOH		

Table 5: RF2 Buffer components.

2.1.2. Bacterial Transformation & Plasmid DNA Purification

To prepare plasmid DNAs Stbl3 *E. coli* strain competent bacterial suspensions were thawed on ice, 10ng of plasmid DNA was added on 50µl of the bacterial suspension. The mixtures were placed on ice for 30min. The plasmid-bacteria mixtures were heat-shocked at 37^{O}C for 30sec and immediately put on ice for 5min. 150 µl super optimal broth with catabolite repression medium (SOC) was added on the heat-shocked bacteria suspension, and the bacteria were incubated at 37^{O}C, using a bacterial shaker (225rpm) for 1hr. The transformed bacteria were spread on the kanamycin or ampicillin antibiotic supplemented LB agar plates, depending on the antibiotic resistance gene of the plasmid construct. The plates were incubated overnight at 37^{O}C. Single colonies formed by the seeded bacteria were picked and inoculated into the desired amount of antibiotic supplemented LB broth (5ml for mini prep, 200ml for midi prep) in bacterial flasks. The bacterial inoculations were incubated overnight at 37^{O}C, using a bacterial shaker (225rpm). Following the incubation, the bacteria were centrifuged at 3750rpm for 15 min. Plasmid DNA was isolated from the precipitated bacteria using Nucleospin Plasmid mini or midi kits (Macherey-Nagel).

CHAPTER 2: MATERIALS AND METHODS

2.1.3. Cloning Experiments

Cloning of KIF13A targeting CRISPR-Cas9 Constructs

I designed four CRISPR-Cas9 constructs targeting four different exons of the *KIF13A* gene using the Chop Chop design tool (Figure 5, Table 6). CHOPCHOP v3 can be found at https://chopchop.cbu.uib.no [201]. The *KIF13A* targeting gRNA oligo pairs were inserted into pLentiCRISPR.v2 plasmid (Addgene: 52961), following BsmBI enzyme restriction (NEB-r0580) using T4 DNA Ligase (NEB-m0202). Ligated constructs were transformed, reproduced into Stbl3 *E.Coli* strain, and sent to Macrogen Europe Labs (Netherlands) for sequencing. Validated ligation constructs added to inventory (Figure 6).

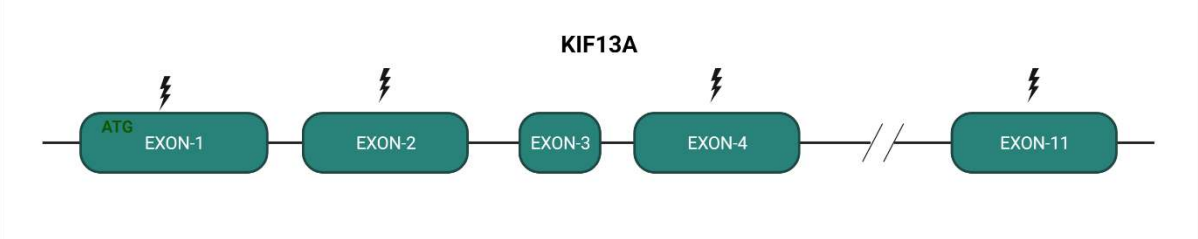

Figure 5: Visual representation of CRISPR-Cas9 targets on KIF13A gene.

CHAPTER 2: MATERIALS AND METHODS

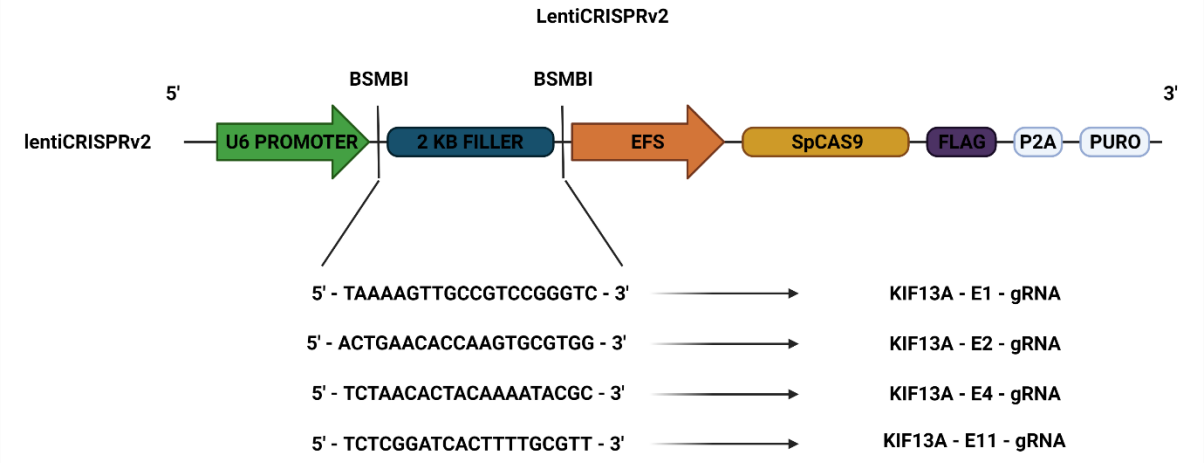

Figure 6: LentiCRISPRv2 partial cDNA map. gRNA were replaced with 2kb filler sequence.

OLIGO NAME	SEQUENCE
KIF13A Exon-1 Guide 1 Oligo 1	caccGTAAAAGTTGCCGTCCGGGTC
KIF13A Exon-1 Guide 1 Oligo 2	aaacGACCCGGACGGCAACTTTTAC
KIF13A Exon-2 Guide 1 Oligo 1	caccGACTGAACACCAAGTGCGTGG
KIF13A Exon-2 Guide 1 Oligo 2	aaacCCACGCACTTGGTGTTCAGTc
KIF13A Exon-4 Guide 1 Oligo 1	caccGTCTAACACTACAAAATACGC
KIF13A Exon-4 Guide 1 Oligo 2	aaacGCGTATTTTGTAGTGTTAGAc
KIF13A Exon-11 Guide 1 Oligo 1	caccGTCTCGGATCACTTTTGCGTT
KIF13A Exon-11 Guide 1 Oligo 2	aaacAACGCAAAAGTGATCCGAGAc
U6 Promoter-Sequencing Primer	GAGGGCCTATTTCCCATGATT

Table 6: The Sequences of KIF13A gRNA oligo pairs and U6 Promoter-Sequencing Primer.

2.1.4. Site-Directed Mutagenesis

Wild type KIF13A-GFP construct (Addgene: 90199) was changed into mutant KIF13A plasmid construct carrying c.4966G>A mutation using Q5® Site-Directed Mutagenesis Kit (NEB) (Figure 7). The mutagenesis primers “G > A” with substitution mutation were designed using NEBaseChanger Tool (Table 7). The plasmid DNA was amplified using the mutagenesis primers. The circularization and template removal of the amplified material was achieved with Kinase-Ligase-DpnI (KLD) enzyme mix treatment (RT, 5 minutes). Circulized DNA transformed into high-efficiency NEB 5-alpha Competent E. coli, provided with the kit, as previously described on “*2.1.2. Bacterial Transformation & Plasmid DNA Purification*”.

CHAPTER 2: MATERIALS AND METHODS

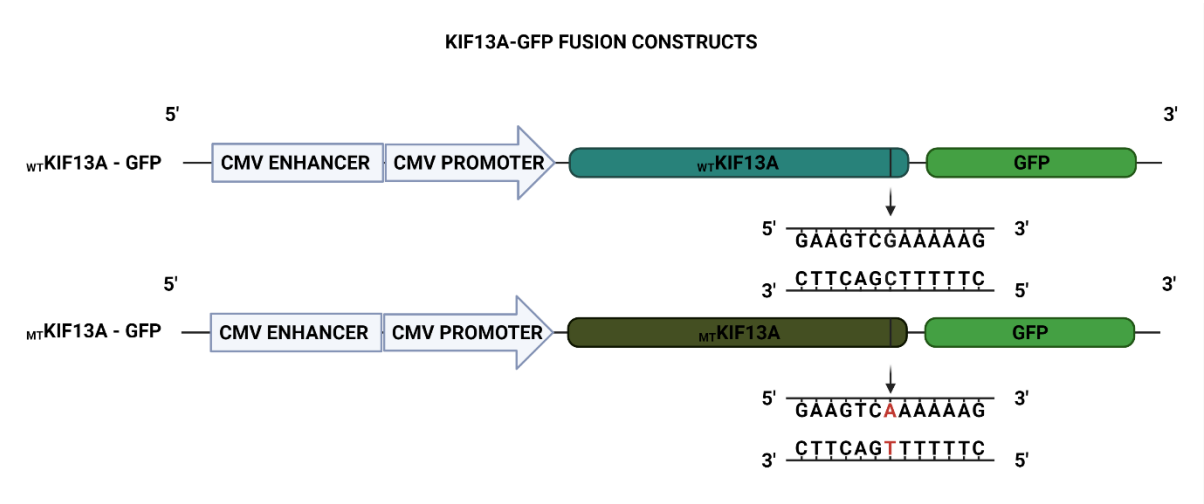

Figure 7: Representative maps of wild type and mutant KIF13A-GFP constructs.

Primer	Sequence
KIF13A – Q5 - FWD	GACAGAAGTCaAAAAAGGCTTG
KIF13A – Q5 - RVS	AACTCTTTGTTTGAGGAC
KIF13A Seq Primer (RVS) - 1	AAAGCACAGCAGAGCCTTGG
KIF13A Seq Primer - 2	CCAAGGCTCTGCTGTGCTTT
KIF13A Seq Primer - 3	CACAGGAAAGACAACGAC
KIF13A Seq Primer - 4	CCTCAGTGCCAATAGGAA
KIF13A Seq Primer - 5	GGAGAGTATGCTGCAGTGG
KIF13A Seq Primer - 6	ACGCAGAGTTTGAAGAGG
KIF13A Seq Primer - 7	CCTTCTAGTGACAGCTCA
KIF13A Seq Primer - 8	GCTTATGTCGGATACCAAGG

Table 7: The list of *KIF13A* site-directed mutagenesis and sequencing primers.

CHAPTER 2: MATERIALS AND METHODS

2.2. Cell Culture Experiments

2.2.1. Human Embryonic Kidney 293T & HeLa Cell Culture

Both human embryonic kidney 293T cells (HEK293T) and HeLa cells were kindly gifted by Robert Weinberg and Ayşe Nazlı Başak to our laboratory, respectively. Both cell lines were cultured in "Complete DMEM Medium" (also referred to as D10 Medium), consisting of DMEM, (Gibco) supplemented with 10% Fetal Bovine Serum (Gibco) and 1% penicillin/streptomycin (Gibco), at 37°C with 5% CO_2, Split 1:6 to 1:8 ratio and frozen using freezing medium consisting of 10% DMSO FBS solution.

2.2.2. Transfection of Plasmids

FuGENE® 6 (FuGENE, Promega) transfection reagent was used for transfection experiments. Briefly, 3µl of FuGENE 6 was mixed with 1µg of plasmid DNA to be transfected. Transfection dosings were adjusted depending on the size of the plasmid and the cell line to be transfected (Example: Table 8).

Plasmid / Reagent Name		Mass or Volume
Lentiviral Plasmid		2500ng
pCMV-VSV-G	Addgene 8454	225ng
pCMV-dR8.2 dvpr	Addgene 8455	2250ng
FuGENE (Promega E2691)		15µl
DMEM 1X		Up to 400µl

Table 8: FuGene Transfection Mix.

2.2.3. Viral packaging of Lentiviral Constructs

$2x10^6$ HEK293T cells were seeded to five 10-cm Petri dishes for each packaging process. Each plate of cells was cotransfected with lentiviral protein-encoding cDNAs [(pVSVg (AddGene 8454), psPAX2 (AddGene 12260)] and lentiviral constructs. FuGENE transfection mix is prepared and incubated at RT for 30 min (Table 8,9). FuGENE transfection mixes were applied dropwise on HEK293T cells following the incubation. The medium was changed with fresh D10 after 12 hours. Virus containing medium were collected at 48h and 72h after transfection. The collected medium was centrifuged at 1500rpm for 5 min, and viral supernatants were filtered through 0.45µm pore-sized filters to remove HEK293T cells and prevent cross-contamination. Concentrated viral solutions were prepared using polyethylene glycol, PEG 8000 (Sigma 1546605). The one-fifth volume of 50% PEG PBS solution was added onto the filtered viral supernatants and incubated for 48 hours at +4ºC. Viruses in PEG solution were then precipitated by centrifugation at 2500rpm for 20min and supernatant was removed. Pellet was dissolved in one-hundredth of the initial volume, using 1X PBS, aliquoted, and stored at - 80ºC. The success of the transduction efficiency of the newly generated virus was determined by assessing the transduction efficiency of EGFP containing lentivirus, prepared in parallel. Following the EGFP lentivirus transduction, HEK293T cells were either counted as a population in flow cytometry or imaged using a fluorescent microscope. Untreated HEK293T Cells were used as the control for both flow cytometry and imaging experiments. Viral packaging is considered successful if ~80 % of the post-transduction samples are GFP positive.

2.2.4. Viral Transduction and Antibiotic Selection

$1x10^5$ of cells were seeded into 1 well of 6-well plate. Following day, 10µl of the concentrated virus and 1 µl of protamine sulfate (PS) (8 mg/ml) were added to the medium. Cells were incubated overnight, and the medium was changed the following morning. Virus (10µl) and PS (8 mg/ml) were added to the medium for the second time, and the medium changed the following morning again. After sequential infection, cells were passaged to a 10-cm petri dish. Antibiotic selection began the next day with the addition of appropriate amount (2 µg/ml for iPSCs, iMNs, HEK293Ts, and HeLa) of puromycin (Gold Biotechnology P-600-100) to the medium of infected and uninfected cells. The selection ended when all uninfected cells were eliminated (~3days). Cells were expanded, stored, and used for further experiments. Knockout (KO) cell lines were cultured for 14 Days before the western blot characterization experiment to provide time for CRISPR-Cas9 construct activity.

Plasmid Name	Source
pLenti-CRISPRv2 KIF13A-E1	Addgene: 52961 - Modified
pLenti-CRISPRv2 KIF13A-E2	Addgene: 52961 - Modified
pLenti-CRISPRv2 KIF13A-E4	Addgene: 52961 - Modified
pLenti-CRISPRv2 KIF13A-E11	Addgene: 52961 - Modified
pLenti-CRISPRv2 NT-I	Addgene: 52961 - Modified
pLenti-CRISPRv2 NT-II	Addgene: 52961 - Modified
pTet-O-Ngn2-puro	Adgggene: 52047
Lenti-MNX1(HB9):RFP	Addgene: 37081

Table 9: The list of lentiviral constructs used in this study.

2.2.5. Mouse Embryo Fibroblast Culture

Primary Mouse Embryo Fibroblast Culture

Mitomycin inactivated mouse embryo fibroblast (MEF) feeder layer preparation protocol was based on Jozefczuk et al. [202]. Balb/C Mouse embryos were collected at mouse embryonic day 13.5 (E13.5) of embryonic development. Embryos were washed with 1% penicillin/streptomycin PBS solution. The Head and visceral tissues of embryos were removed, and the remaining tissues were minced using sterile razor blades. Cell clumps were incubated with 0.25% trypsin at 37ºC for 10 min for further dissociation. Trypsin was inactivated with 10% FBS-containing D10 medium (DMEM, 10% FBS, 1% penicillin/streptomycin). Primary mouse embryo fibroblasts were frozen using freezing medium consisting of 10% DMSO FBS solution.

Mitomycin Inactivation

MEFs were expanded on 15 cm plates in a 1:4 ratio up to three passages. Once MEFs expanded to the desired amount and reached 80% confluency, the medium was replaced with 10ml fresh D10 medium. A carcinostatic agent, Mitomycin C (Millipore 475820), was added to the medium (10 µg/ml), and cells were incubated for 2 h at 37ºC. Mitomycin C treated cells were washed twice with 1X PBS, dissociated with 0.05% Trypsin, counted using a hemocytometer, aliquoted, and frozen as multiples of 1 million using 10% DMSO DMEM FBS solution (10% DMSO, 50% DMEM, 40% FBS).

2.2.6. Primary Fibroblast Culture

Skin biopsy samples of six individuals were collected by Koç University Research Center for Translational Medicine via the skin punch biopsy method (Ethical Review Board Number: 2016.247.IRB2.119).

Skin samples were washed in PBS and transferred to a petri dish, where they were cut into small, straight-edged, rectangular pieces using sterile razor blades. The pieces were transferred to individual wells of 6-well plates under coverslips. Samples were cultured in D10 medium (DMEM, 10% FBS, 1% penicillin/streptomycin), at 37°C with 5% CO_2. The medium was changed every other day, and cells were passaged at an appropriate ratio (1:2 to 1:6) when the monolayer of cells reached 70-80% confluency, using 0.05% Trypsin EDTA solution (Gibco). The ensuing cell culture predominantly contains fibroblasts and keratinocytes. Pure fibroblast population achieved by continual culturing and passaging of the cells as D10 medium favors fibroblast growth instead of keratinocyte. Patient-specific fibroblasts were frozen using freezing medium consisting of 10% DMSO FBS solution.

CHAPTER 2: MATERIALS AND METHODS

2.3. Reprogramming of Patient-Specific Fibroblasts Into iPSCs

$3x10^5$ Patient fibroblast were nucleofected with 1000ngs of each reprogramming factor, pCXLE-hOCT3/4-shp53-F (Addgene: 27077), pCXLE-hUL (Addgene:27080), pCXLE-hSK (Addgene: 27078), and pCXWB-EBNA1 (Addgene: 37624), as triplicates, using Amaxa 4D Transfector System (Lonza), with 1400 V, 20 ms, 2 pulse parameters. Following nucleofection, cells were transferred to 6-well plate and cultured in D10 medium without penicillin/streptomycin. The medium was replaced with Complete D10 medium with penicillin/streptomycin the following day. The medium was changed every other day for 6 days. On day 7, Fibroblasts were transferred onto plates with MEF (Mouse embryonic fibroblast) feeder layer. At day 8 D10 medium was substituted with human embryonic stem cell (hESC) medium (20% KOSR, 1% L-glutamine, 1% non-essential amino acids, 0.1 mM β-mercaptoethanol, 10 ng/ml bFGF in DMEM/F12). Newly formed iPSC colonies were isolated and transferred to individual MEF plates using a sterile syringe needle and micropipette under sterile conditions. After this point, isolated colonies were named and treated as different cell lines. To increase reprogramming efficiency, 3μM Dot1L inhibitor (EPZ004777, iDot1L) was added to the medium for the first two weeks of the reprogramming (Onder ve Daley 2012). iPSCs were cultured on MEF feeder layer using hESC and Matrigel (Corning) plates using mTeSR™ Plus medium (Stemcell Technologies) at 37°C with 5% CO_2. iPSCs were frozen using freezing medium consisting of 10% DMSO FBS solution. For IF staining, karyotype analysis, DNA/RNA isolation, and differentiation experiments, iPSCs were expanded on Matrigel (Corning) plates using mTeSR™ Plus medium.

CHAPTER 2: MATERIALS AND METHODS

2.4. Differentiation of iPSCs into Motor Neurons

Patient-specific iPSCs were cultured and maintained on Matrigel (Corning) coated plates in mTeSR™ Plus (STEMCELL Technologies) medium at 37°C with 5% CO_2. Differentiation of iPSCs into MNs protocol was primarily based on Du et al., 2015 method paper [162]. However, the suspension culture step was substituted with adherent culture on Matrigel-coated plates to standardize the differentiation process among different cell lines and replicates.

IPSCs and derivatives were cultured on Matrigel coated plates in the same base medium (referred to as NBM), which consisted of 1:1 DMEM-F12 and Neurobasal Plus Medium (Thermo Fisher Scientific) supplemented with N2 (0.5%), B27 Plus (0.5%), Glutamax (1%) and penicillin/streptomycin (1%), at 37°C with 5% CO_2, throughout the process. Neuronal differentiation was achieved by the differential usage of small molecule cocktails of CHIR99021, Dorsomorphin Homolog 1, SB431542, Retinoic Acid, Purmorphamine, and Compound E (See below). Valproic acid added to media during the expansion period of MNPs to keep them from further differentiation, and Y Compound (Y-27632) (STEMCELL Technologies) to eliminate cell death due to stress caused by passaging and improve passaging, and cell thawing efficiency. Cells were dissociated via incubation with Accutase™ Cell detachment solution (STEMCELL Technologies) at 37° C for 4 minutes. Suspensions of cells were diluted with DBPS and centrifuged at 1300rpm for 4 minutes to discard Accutase™. Cells were resuspended and seeded using an appropriate mixture of NBM and chemical cocktail, depending on the differentiation stage.

Cells were passaged as duplicates or triplicates minimum to have adequate amounts of cells or wells for characterization purposes. Motor neurons in the population were identified using motor neuron-specific MNX1-RFP reporter construct (Addgene 32930). Further characterization experiments involved RT-qPCR and Immunofluorescence of specific markers.

Neuronal Induction (NI)

Patient-specific iPSCs were cultured and maintained on matrigel (Corning) coated plates in mTeSR™ Plus. IPSCs were collected before they exceeded 70-80% confluency and $1x10^6$ cells seeded on two wells of a matrigel coated 6-well plates in mTeSR™ Plus containing 10µM Y Compound. On the following day, media was replaced with NBM containing “Neuronal

Induction Cocktail" which consists of CHIR99 (3μM), DMH1 (2μM), and SB43 (2μM) to initiate neuronal differentiation. The medium was changed every other day for 6 days. On day 7, Cells on the other well were split at a 1:6 ratio, and cells on the other were collected for RNA isolation.

MN Specification (Caudalization)

"NI-Molecule Cocktail" was switched with "Caudalization Cocktail" which consists of CHIR99 (1μM), DMH1 (2μM), Purmorphamine (0.5μM), Retinoic Acid (0.1μM), and SB43 (2μM). The medium was changed every other day for 6 days. On day 13, RNA was isolated from one of the wells, another was passaged at 1:6 ratio, and the remaining four were frozen using a freezing medium consisting of 10% DMSO FBS solution.

Cells at this stage could be frozen and passaged up to 3 times, conserving their differentiation capacity. To minimize cell death and keep MNPs from further differentiation during thawing and passaging processes, Valproic acid (0.5 μM) must be added to "Caudalization Cocktail" to form "Expansion Cocktail".

MN Maturation

"Expansion Cocktail" was switched with "Maturation Cocktail", which consists of Purmorphamine (0.1μM), and Retinoic acid(0.5μM) to achieve $MNX1^+$ early stage (immature) esMNs. The medium was changed every other day for 6 days. On day 19, $MNX1^+$ esMNPs were seeded onto wells at 21,000 cells/cm^2 density (Figure 24). "Maturation Cocktail" was switched with "Final Maturation Cocktail", which contains Purmorphamine (0.1μM), Retinoic acid(0.5μM), and Compound E (0.1μM) to further maturate the newly formed MNX1 expressing esMNs into mature, CHAT, and MNX1 expressing, late-stage lsMNs. Insulin-like growth factor 1(IGF-1), brain-derived neurotrophic factor (BDNF), and ciliary neurotrophic factor (CNTF) (R&D, 10 ng/ml each) were also included in the final maturation cocktail to enhance neuronal survival during the final maturation stage.

CHAPTER 2: MATERIALS AND METHODS

2.5. Characterization and Molecular Biology Methods

2.5.1. Immunofluorescence

Cells were fixed via 2% paraformaldehyde (PFA) incubation for 30 min at room temperature. PFA was withdrawn, and samples were washed three times with PBS. Fixed cells were permeabilized via 10 min RT incubation using 0.5% Triton-X100 PBS solution (Perm Buffer). Following permeabilization, samples were blocked via 1hr RT incubation with blocking buffer, 5% Goat Serum, 0.2% Triton-X100 PBS Solution. Samples were washed three times with PBS and then incubated with 1:100 dilutions of primary antibodies at +4 °C overnight. Sample coverslips were placed on 15µl of antibody solutions, facing downwards, in a sealed container. The following day, samples were transferred to 24 well plates washed three times with PBS. Samples were incubated with 1:500 dilutions of secondary antibodies, in the same fashion to primary antibody treatment stage, at RT for 1hr. Samples were washed three times with PBS. Coverslips were placed on 10µl VECTASHIELD® Antifade Mounting Medium with DAPI (VECTOR Laboratories) and sealed with colorless nail polish. Samples and slides were protected from the light during and after the secondary antibody treatment stage. Co-staining of specific proteins was achieved by using a selection and combination of antibodies whose host organisms do not coincide (Table 10).

CHAPTER 2: MATERIALS AND METHODS

#	Antibody	Catalog Number	Source	Used In	Working Concentration
1	**SSEA4**	BD560218	Mouse	IF	1:100
2	**NANOG**	Abcam ab21624	Rabbit	IF	1:100
3	**OCT4**	Abcam ab19857	Rabbit	IF	1:100
4	**KIF13A**	Thermo Fischer PA5-30874	Rabbit	IF / WB	1:100 / 1:1000
5	**TUJ1 (Beta-III-Tub.)**	Abcam ab78078	Mouse	IF	1:100
6	**MNX1**	Sigma HPA071717-100uL	Rabbit	IF	1:100
7	**HA-Tag**	Abcam ab9110	Tag Specific	IF / WB	1:100 / 1:1000
8	**HRP Streptavidin**	Biolegend 405210	WB	WB	1:10000
9	**Alexa Fluor 488 Anti-Rabbit**	Thermo Fischer A27034	Goat	IF	1:500
10	**Alexa Fluor 555 Anti-Rabbit**	Thermo Fischer A27039	Goat	IF	1:500
11	**Alexa Fluor 488 Anti-Mouse**	Thermo Fischer A28175	Goat	IF	1:500
12	**Alexa Fluor 555 Anti-Mouse**	Thermo Fischer A28180	Goat	IF	1:500

Table 10: The list of antibodies.

2.5.2. Real-Time Quantitative PCR (RT qPCR)

RNA was isolated from harvested cells using Nucleospin RNA kit (Macherey-Nagel). RNA was simultaneously isolated from the last well(s) remaining or simultaneously from all wells to prevent the toxic effect of TRIzol (present in the lysis buffer) on the neighboring wells. The concentration of the collected RNA was measured via Nanodrop 200 (Thermo Scientific).

cDNA Synthesis, Reaction mixes of, 1µg RNA, 2.5µl 2 mM dNTP (Life Technologies), and 2 µl 50 µM hexanucleotide mix (Invitrogen) were prepared, and dH_2O was added to reach total reaction mix volume to 16.5µl. The mixture was incubated in a Thermal Cycler (BIO RAD T100) at 65°C for 5 min, and samples were quickly cooled on ice. Reverse Transcription master mix consisting of 5 µl 5X First Strand Buffer (Invitrogen), 2 µl 0.1M DTT (Invitrogen), and 0.5 µl RNasin (Promega), was added to the samples and incubated for 10 minutes at room temperature. 1 µl of MMLV-RT enzyme (Invitrogen) was added to each sample. The samples were incubated in a Thermal Cycler at 37°C for 1 hour for the cDNA synthesis and 70°C for 15 minutes for inactivation of the enzymes. The reaction products were diluted to 100 µl with dH_2O.

RT-qPCR, Relative mRNA levels were quantified with quantitative real-time PCR. Primer master mixes for each specific primer pair (Table 11, 2.5µM each) were prepared to consist of 1X LightCycler® 480 SYBR Green I Master (ROCHE) and dH_2O with a total reaction volume of 18µl, for each reaction. cDNAs synthesized from 1 µg RNA were used as the template. Primer master mixes of 18µl were mixed with 2µl of cDNA sample in 96-well opaque plates (Roche). qPCR reaction was run on LightCycler 480 (ROCHE), as reaction conditions specified (Table 12). Relative gene expression was analyzed using the comparative C(T) method [203]. C(T) stands for threshold cycle where fluorescent first reaches a predetermined level. cDNA amounts between test and control samples were normalized using Beta-Actin expression as the internal control. qPCR reactions with a threshold cycle above 33 were considered not detected (false positive), and the gene tested for expression was assumed not expressed.

CHAPTER 2: MATERIALS AND METHODS

#	Name	Sequence
1	**hActin-qPCR-FWD**	GGAGGAGCAATGATCTTGAT
2	**hActin-qPCR-RVS**	TGAAGTGTGACGTGGACATC
3	**hNanog-qPCR-FWD**	TGATTTGTGGGCCTGAAGAAAA
4	**hNanog-qPCR-RVS**	TGGTGGTAGGAAGAGTAAAG
5	**hKIF13A-qPCR-FWD**	GAGAATGACCAGGGAGGCAC
6	**hKIF13A-qPCR-RVS**	AAGGTGACCAGGCGAACAAA
7	**hSOX1-qpcr-FWD**	GAGTGGAAGGTCATGTCCGAGG
8	**hSOX1-qpcr-RVS**	CCTTCTTGAGCAGCGTCTTGGT
9	**hPAX6-qpcr-FWD**	CCGTGTGCCTCAACCGTA
10	**hPAX6-qpcr-RVS**	CACGGTTTACTGGGTCTGG
11	**hOLIG2-v2-qpcr-FWD**	ATGCACGACCTCAACATCGCCA
12	**hOLIG2-v2-qpcr-RVS**	ACCAGTCGCTTCATCTCCTCCA
13	**hMNX1-qpcr-FWD**	GCACCAGTTCAAGCTCAAC
14	**hMNX1-qpcr-RVS**	GCTGCGTTTCCATTTCATCC
15	**hCHAT-qpcr-FWD**	TGAGTACTGGCTGAATGACATG
16	**hCHAT-qpcr-RVS**	AGTACACCAGAGATGAGGCT
17	**hGFAP-qpcr-FWD**	TGCCTATAGACAGGAAGCAGA
18	**hGFAP-qpcr-RVS**	GGACGCCATTGCCTCATACT
19	**hGRIA1-qpcr-FWD**	GGGGAGGTGATTCCAAGGAC
20	**hGRIA1-qpcr-RVS**	CCAGTTACAATCCCGTGGCT

Table 11: The list of RT-qPCR Primers.

Program Name	Cycle(s)	Temperature	Ramp Rate (ºC/s)	Hold (hh:mm:ss)
Pre-Incubation	1	95ºC	4.4	00:05:00
		95ºC	4.4	00:00:30
Amplification	45	55ºC	2.2	00:00:30
		72ºC	4.4	00:00:30
		95ºC	4.4	00:00:10
Melting Curve	1	65ºC	2.2	00:01:00
		97ºC	0.11	Continuous
Cooling	1	40ºC	2.2	00:00:30

Table 12: RT-qPCR conditions.

2.5.3. Test of Episomal Vector Integration into Genome

Reprogramming factors, pCXLE-hOCT3/4-shp53-F (Addgene: 27077), pCXLE-hUL (Addgene:27080), pCXLE-hSK (Addgene: 27078), and pCXWB-EBNA1 (Addgene: 37624) all contain Epstein–Barr nuclear antigen 1 (EBNA) encoding sequence. Therefore, the presence of EBNA sequence was used as a marker of integration of the constructs into the genome. DNA was isolated from iPSCs by using Nucleospin Tissue kit (Macherey-Nagel). The concentration of collected DNA was measured via Nanodrop 200 (Thermo Scientific). PCR was conducted under specified conditions, using Phusion® High-Fidelity DNA Polymerase (NEB), and listed EBNA and GAPDH primers (Table13-16). GAPDH amplification was used as the positive control. pCXLE-hSK plasmid (10ng) DNA was used as the control for EBNA sequence PCR amplification, and 200ng iPSC genomic DNA was used.

2.5.4. Re-validation of the Genomic State of Patient-Specific iPSCs

To validate the mutations in *KIF13A* and *SLC52A3* genes, gene regions of concern were amplified with PCR, under specified conditions, using Phusion® High-Fidelity DNA Polymerase (NEB), with the specified primers (Table14,17-19). PCR products were sent to Macrogen Europe (Netherlands) for sequencing.

Primer Name	Primer Sequence
EBNA-Fwd	AGGGCCAAGACATAGAGATG
EBNA-Rev	GCCAATGCAACTTGGACGTT
GAPDH-Fwd	ATCACCATCTTCCAGG AGCGA
GAPDH-Rev	TTCTCCATGGTGGTGAAGACG

Table 13: Primers used in PCR amplification and EBNA integration test.

Component	50 µl Reaction	Final Concentration
Nuclease-free water	to 50 µl	
5X Phusion HF	10 µl	1X
10 mM dNTPs	1 µl	200 µM
10 µM Forward Primer	2.5 µl	0.5 µM
10 µM Reverse Primer	2.5 µl	0.5 µM
Template DNA	200ng gDNA 10ng Plasmid DNA	<250ng
DMSO (optional)	1.5 µl	3%
Phusion DNA Polymerase	0.5 µl	1.0 units/50 µl PCR

Table 14: Phusion Polymerase PCR Reaction Mix.

GAPDH	Cycle(s)	Temperature	Duration (hh:mm:ss)
Initial Denaturation	1	95°C	00:03:00
		95°C	00:00:30
Amplification	30	64°C	00:00:30
		72°C	00:01:00
Final Extension	1	72°C	00:10:00
Hold	1	4°C	Continuous

Table 15: GAPDH PCR Conditions.

EBNA	Cycle(s)	Temperature	Duration (hh:mm:ss)
Initial Denaturation	1	95°C	00:03:00
		95°C	00:00:10
Amplification	30	65°C	00:00:30
		72°C	00:00:30
Final Extension	1	72°C	00:05:00
Hold	1	4°C	Continuous

Table 16: EBNA PCR Conditions.

CHAPTER 2: MATERIALS AND METHODS

Primer Name	Primer Sequence
KIF13A-Fwd	CTGTCTGACATGGTGGTCCC
KIF13A-Rvs	TCAGGGATGCTCTGGGATGA
SLC52A3-Fwd	GCAGTCATTATTGCCACCTTG
SLC52A3-Rvs	AGGCCACCAGGGTATAGA

Table 17: Primers used in PCR amplification and sequencing.

KIF13A PCR	Cycle(s)	Temperature	Duration (hh:mm:ss)
Initial Denaturation	1	95°C	00:03:00
		95°C	00:00:30
Amplification	30	64°C	00:00:30
		72°C	00:01:00
Final Extension	1	72°C	00:10:00
Hold	1	4°C	Continuous

Table 18: KIF13A PCR Conditions.

SLC52A3	Cycle(s)	Temperature	Duration (hh:mm:ss)
Initial Denaturation	1	95°C	00:03:00
		95°C	00:00:10
Amplification	30	65°C	00:00:30
		72°C	00:00:30
Final Extension	1	72°C	00:05:00
Hold	1	4°C	Continuous

Table 19: SLC52A3 PCR Conditions.

2.5.5. Karyotype Analysis

Karyotype analysis of the iPSCs was conducted at Koç University Genetic Diagnosis Centre. Samples were delivered in Matrigel-coated T25 flasks in mTeSR™ Plus. Cell cycles of the dividing cells were arrested at metaphase using colchicine. The cells arrested in metaphase were treated with hypotonic KCl solution that causes their nuclei to swell and the cells to burst. The isolated nuclei were treated with a chemical fixative, dropped on a glass slide, and stained using Giemsa stain that reveals structural features of the chromosomes. Chromosomes were investigated and imaged under a microscope.

2.5.6. Teratoma Assay

Confluent iPSCs in 10cm Petri dishes were collected and injected into SCID mice intramuscularly. Animals were sacrificed when the teratomas reached 2 centimeters in their greatest dimension or at day 90, whichever comes first. Teratomas were washed in sterile PBS, fixed in 10% formalin solution, and sent for H&E staining to KUTTAM Koç University Hospital Pathology Department. Samples were examined for the formation of cells derived from endoderm, ectoderm, and mesoderm.

2.5.7. Western Blot

Cell Lysis, Medium was withdrawn, and cells were washed with PBS twice, ice-cold PBS added on plates, and cells detached from plates using scrapers. Cells were pelleted by centrifugation at 1500rpm for 5 min. Supernatants were removed, and cell lysis was immediately initiated with NP40 whole cell lysis buffer (

Table ***20***). Cell suspensions were incubated for 1 hour on ice with gentle agitation (~20 rpm) in addition, cell suspensions were vigorously vortexed 3 times with 20min intervals during 1 hour incubation.

Blotting, control and overexpression protein samples not exceeding 100µg protein were used in a 1:2 ratio. Whole-cell lysates of 100µg for control and 50µg for overexpression sample proteins were boiled for 10 min with loading buffer (4X Laemmli sample buffer, Bio-Rad). Precision Plus Protein Dual Color Standards (Bio-Rad) were used as a molecular weight ladder. Samples and color standards were loaded onto 4–15% Mini-PROTEAN TGX Precast Protein Gels (Bio-Rad). Both running of protein gels and protein transfer onto membranes

were conducted using Mini-PROTEAN Tetra electrophoresis system (Bio-Rad). Protein gels were run using TGS buffer (diluted from 10X stock, Bio-Rad). Proteins were transferred onto Immun-Blot PVDF Membrane (Bio-Rad) via wet transfer technique (15volt overnight incubation in +4ºC) using wet transfer buffer (20% methanol (v/v) - TG diluted from 10X, Bio-Rad). Membranes were incubated with Ponceau S Solution (Abcam) for 5min at RT to reversibly stain and visualize the proteins bands to assess successful transfer. Membranes were washed with TBS-T (20 mM Tris, 150 mM NaCl, 0.1% Tween 20 –pH 7.6) and were blocked via incubation with 5% blotting grade blocker (Bio-Rad) dissolved in TBS-T (20 mM Tris, 150 mM NaCl, 0.1% Tween 20 –pH 7.6) for 2 hours at RT with gentle agitation (~20rpm). To prevent biotin contamination, membranes to be incubated with Streptavidin-HRP antibody were blocked using 2% bovine serum albumin (BSA, Sigma) dissolved in TBS-T. Following the blocking step, membranes were incubated overnight at 4°C with primary antibody solution (1:1000 primary antibody in 2% BSA, 0.02% NaN3 in TBS-T. After primary antibody incubation, membranes were washed with TBS-T solution 3 times with 15 min intervals on ~20 rpm shaker at room temperature and incubated with secondary antibody solution (1:5000 secondary antibody in 5% blotting grade blocker in TBS-T) at room temperature for 2 hours. Membranes incubated with streptavidin-HRP conjugated antibody were washed with TBS-T solution 3 times at 15 min intervals on ~20 rpm shaker at room temperature. Proteins were visualized using Odyssey Fc Imaging System (LiCor) following 1 min RT incubation with Pierce ECL Western Blotting Substrate (Thermo Scientific). See Table 10 for the list of antibodies.

Whole Cell Lysis Buffer
50mM TRIS (pH 8.0)
250mM NaCl
5mM EDTA
50mM NaF
1% NP-40
0.02% NaN_3
1mM PMSF
1X Protease Inhibitor (Roche)
dH_2O

Table 20: Whole cell lysis buffer content.

2.6. Statistical Analysis

For all other experiments, differences between two groups were analyzed using a two-tailed Student's t-test, unless the data were non-normally distributed, for which two-sided Mann-Whitney testing is used. Differences between more than two groups were analyzed by one-way ANOVA with Tukey correction for multiple testing. Significance assumed at $P < 0.05$. Error bars represent the standard error (s.err.) unless otherwise stated.

CHAPTER 3: RESULTS

3.1. Generation & Characterization of Integration free Patient-Specific iPSC Lines

3.1.1. Patient-Specific Primary Fibroblast Culture

To generate patient-specific iPSCs, skin biopsy samples, from one healthy four *KIF13A* mutants from KU-BVVL-Family and one "conventional BVVL patient" carrying *SLC52A3* mutation (c.802C>T p.Arg268Trp), were collected by Koç University Research Center for Translational Medicine via the skin punch biopsy method (Ethical Review Board Number: 2016.247.IRB2.119). Patient-specific fibroblasts were expanded and stocked (Figure 2,8 Table 21). Prior to reprogramming the fibroblast into iPSCs, I validated the presence of the mutations of interest in those fibroblasts. Gene regions of interest were amplified with PCR and sequenced. Sequencing results showed that the patient fibroblasts carry mutations that were revealed by whole-exome sequencing (Figure 9,10).

#	Name	Mutation	Nucleotide Change	Change Consequence in the Protein
1	**KU-BVVL - KIF MT - 1 Fibro**	KIF13A Mutant	c.4966G>A	p.Glu1656Lys
2	**KU-BVVL - KIF MT - 2 Fibro**	KIF13A Mutant	c.4966G>A	p.Glu1656Lys
3	**KU-BVVL - KIF MT - 3 Fibro**	KIF13A Mutant	c.4966G>A	p.Glu1656Lys
4	**KU-BVVL - KIF MT - 4 Fibro**	KIF13A Mutant	c.4966G>A	p.Glu1656Lys
5	**KU-BVVL - WT - 5 Fibro**	Wild Type	-	-
6	**KU-BVVL - SLC MT - 6 Fibro**	SLC52A3 Mutant	c.802C>T	p.Arg268Trp

Table 21: The list of patient-specific fibroblast lines.

CHAPTER 3: RESULTS

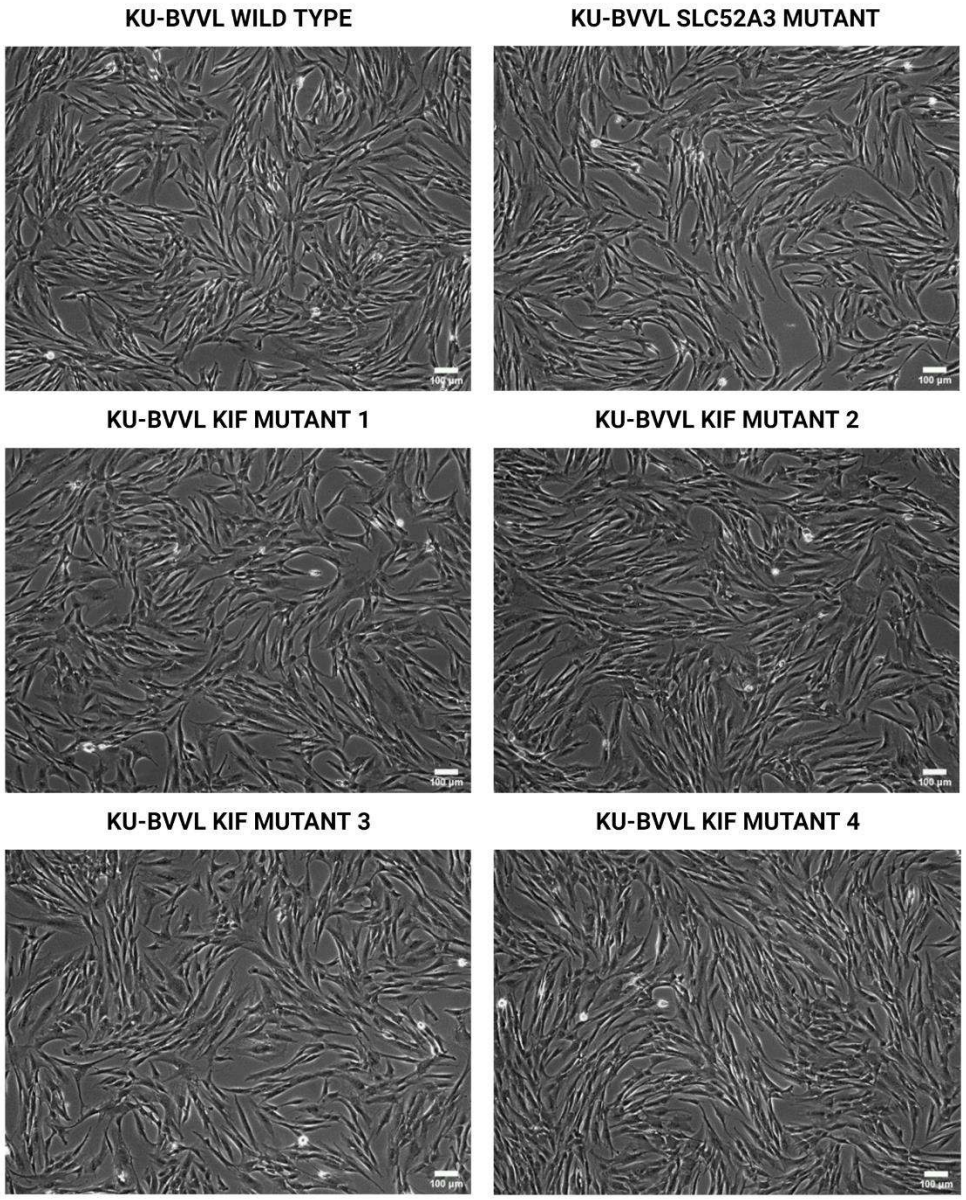

Figure 8: Phase Contrast images of KU-BVVL-Fibroblasts. (Scale Bar: 100µm)

CHAPTER 3: RESULTS

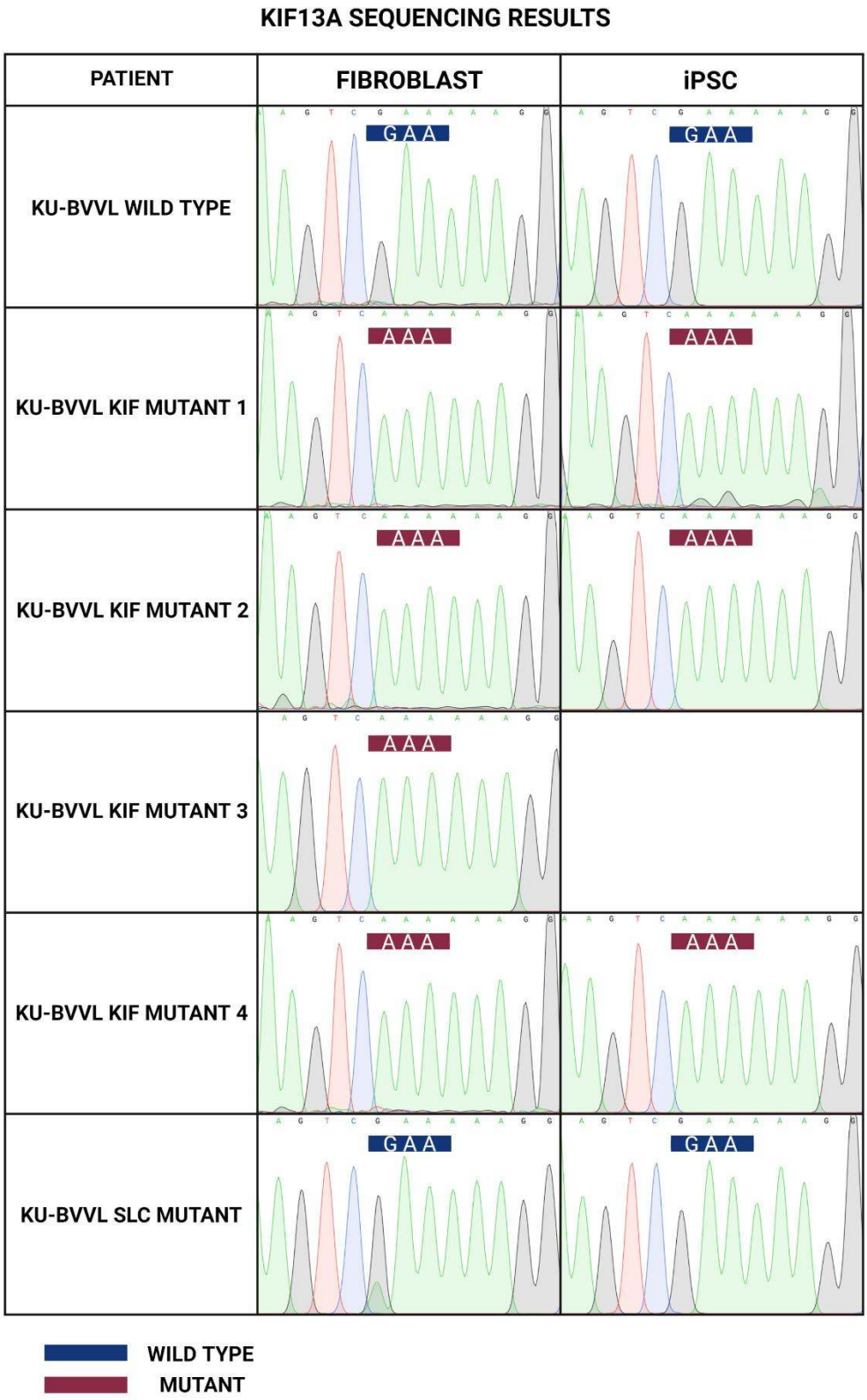

Figure 9: *KIF13A* gene sequencing results. Mutation status of patient specific KU-BVVL Cell lines were validated. Wild-type and mutant codons were highlighted with blue and red bars, respectively.

CHAPTER 3: RESULTS

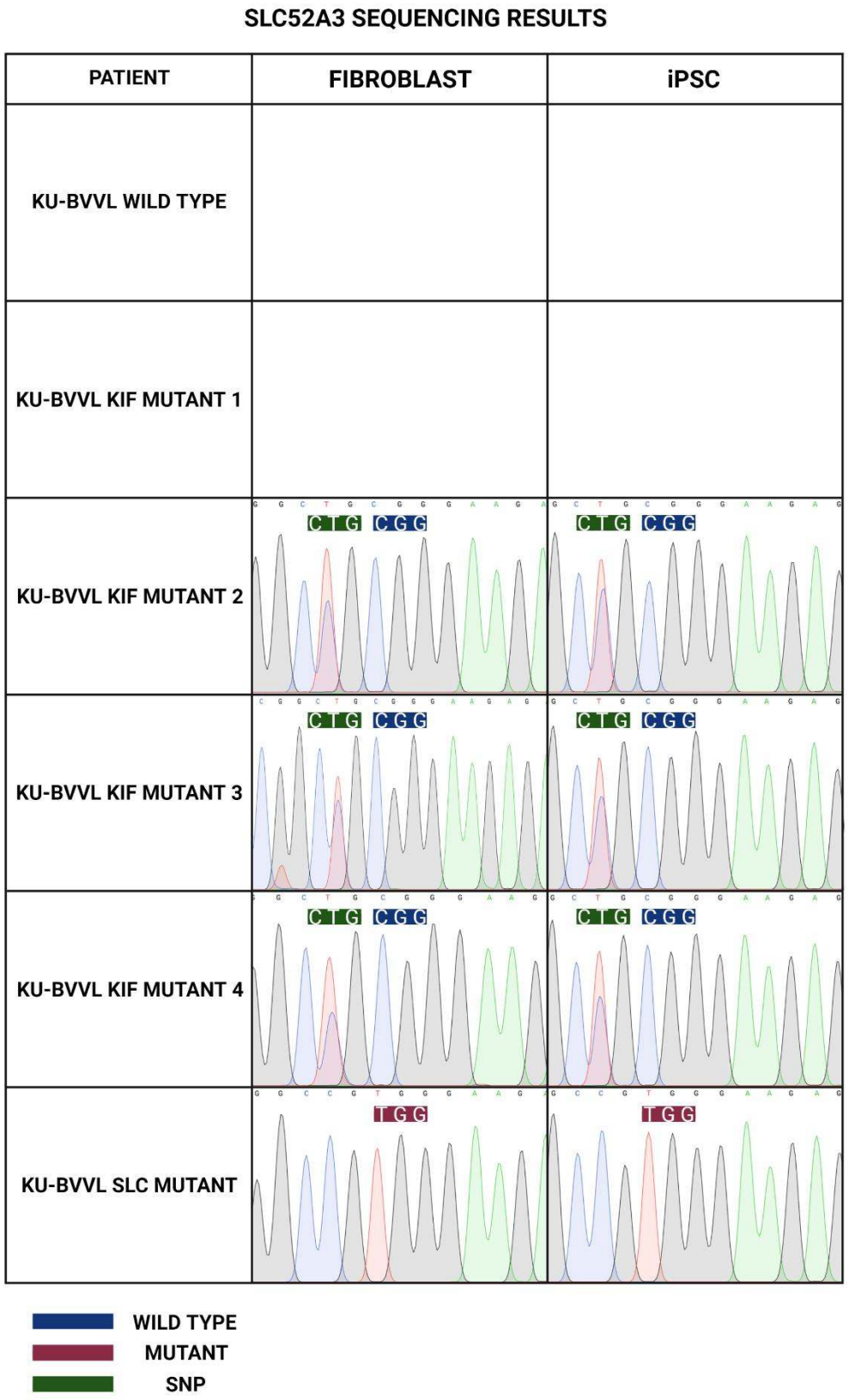

Figure 10: *SLC52A3* gene sequencing results. Mutation status of patient specific KU-BVVL Cell lines were validated. Wild-type, mutant and SNP containing codons were highlighted with blue, red, and green bars, respectively.

CHAPTER 3: RESULTS

3.1.2. The Generation of Patient-Specific iPSC Lines

I generated patient-specific iPSCs by nucleofecting patient fibroblasts with 1000ngs of each reprogramming factor, pCXLE-hOCT3/4-shp53-F (Addgene: 27077), pCXLE-hUL (Addgene:27080), pCXLE-hSK (Addgene: 27078), pCXWB-EBNA1 (Addgene: 37624). On day 21 post-nucleofection, I began to observe newly forming iPSC colonies. I isolated and expanded the twelve embryonic stem cell-like colonies from each patient-derived fibroblast line, considering cell morphology and proliferation rate. I narrowed this number to five clones for each patient during expansion, which were expanded and stocked (Figure 11,12 Table 22).

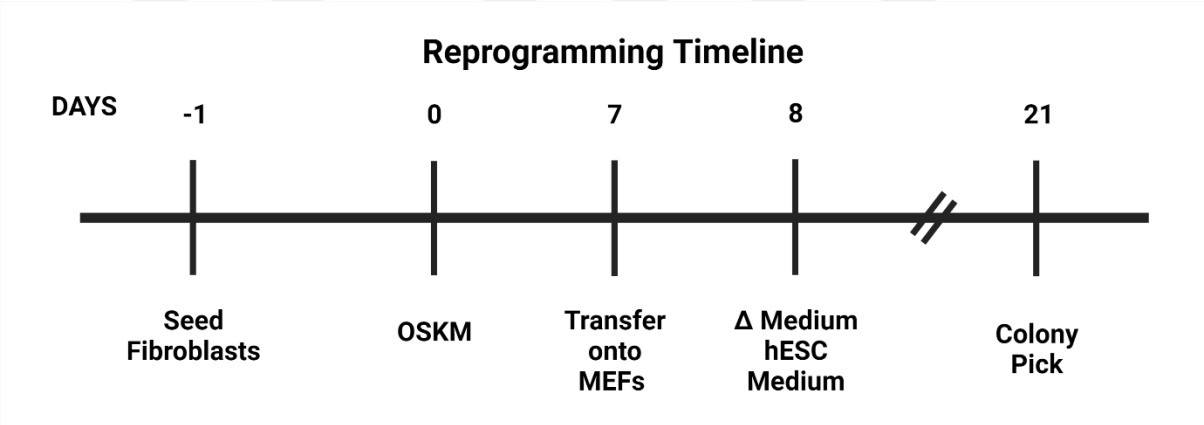

Figure 11: Reprogramming timeline.

#	Name	Colony # (Pat./Col.)	Mutation	Nucleotide Change	Change Consequence
1	**KU-BVVL - KIF MT - 1 iPSC**	1.1	KIF13A Mutant	c.4966G>A	p.Glu1656Lys
2	**KU-BVVL - KIF MT - 2 iPSC**	2.1	KIF13A Mutant	c.4966G>A	p.Glu1656Lys
3	**KU-BVVL - KIF MT - 3 iPSC**	3.1	KIF13A Mutant	c.4966G>A	p.Glu1656Lys
4	**KU-BVVL - KIF MT - 4 iPSC**	4.4	KIF13A Mutant	c.4966G>A	p.Glu1656Lys
5	**KU-BVVL - WT - 5 iPSC**	5.2	Wild Type	-	-
6	**KU-BVVL - SLC MT - 6 iPSC**	6.2	SLC52A3 Mutant	c.802C>T	p.Arg268Trp

Table 22: The list of patient-specific iPSC lines generated and used in this study.

CHAPTER 3: RESULTS

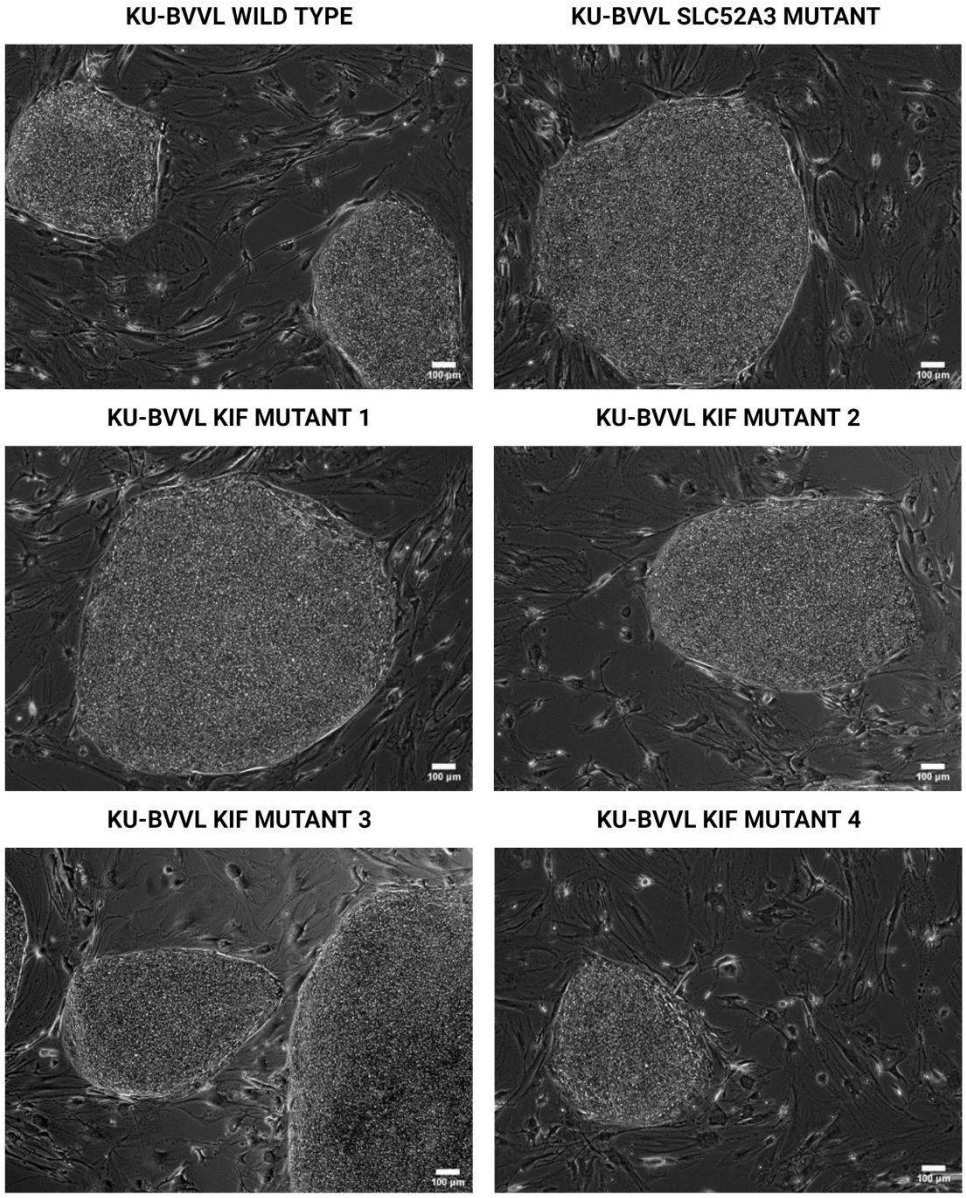

Figure 12: Phase contrast images of KU-BVVL-iPSCs. IPSCs were grown on MEF feeder layer using hESC medium (Scale Bar: 100µm).

CHAPTER 3: RESULTS

3.1.3. Characterization of Patient-Specific IPSC Lines

I conducted a series of characterization experiments on newly generated KU-BVVL-iPSCs to assess whether: (1) these cells still carry mutations of interest, (2) there is an integration of episomal vectors into the genome, (3) that pluripotency related proteins are present, (4) there is any chromosomal abnormality caused during the reprogramming procedure, and (5) these cells are pluripotent.

3.1.4. Re-validation of Disease-Specific Mutations in iPSCs

Whole-exome sequencing conducted by Koç University Neurodegeneration Research Laboratory (KU-NDAL) revealed the presence of disease-related mutations in our patient group. Although the genome of induced pluripotent stem cells (iPSCs) is thought to be identical to the source organism, in this case, our patients, genetic variations can be introduced into the iPSCs from different sources during iPSC generation and maintenance. To re-validate the mutations in *KIF13A* and *SLC52A3* genes, DNA from iPSCs were isolated, gene regions of interest were amplified with PCR and sequenced. Sequencing results show that the patient fibroblasts carry mutations that are revealed by whole-exome sequencing (Figure 9,10).

3.1.5. EBNA Integration Assay

Our reprogramming protocol is based on the transient expression of Yamanaka factors (Oct-4, Sox2, Klf4, c-Myc). Unlike lentiviral transduction, nucleofection of OSKM vectors is known to be non-integrating, meaning; nucleofected constructs will be present in the cells for a limited time, and the vector constructs will dilute out as cells divide. However, there is still a chance of integration. All constructs that were used for reprogramming the fibroblast into iPSCs contain two components of the Epstein-Barr virus, OriP, and EBNA1. OriP/EBNA1 system enables the relatively high and long-term expression of reprogramming factors, ultimately increasing reprogramming efficiency [204]. OriP or EBNA1 sequences in the genomic DNA serves as a marker of the integration of OSKM vectors into the genome.

CHAPTER 3: RESULTS

To test whether the episomal vectors used in reprogramming integrated into the genome of the patient fibroblasts, I conducted EBNA integration assay. KU-BVVL-iPSCs were passaged for at least ten passages to make sure EBNA1 sequence containing OSKM vectors was no longer present in the cells. I then conducted EBNA1 and GAPDH (positive control) PCR amplification on genomic DNA samples of the KU-BVVL-iPSCs and EBNA control plasmid. Agarose gel electrophoresis results show that OSKM vectors did not integrate into the genome of the KU-BVVL-iPSCs (Figure 13).

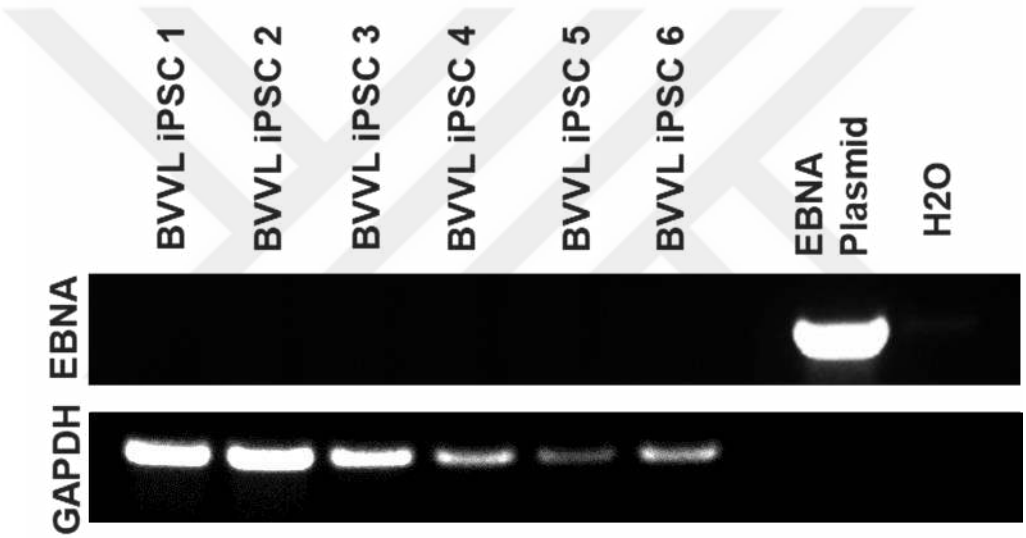

Figure 13: EBNA integration analysis of KU-BVVL-iPSCs. PCR-based method was used to analyze genomic integration of episomal reprogramming vectors. EBNA sequence which is encoded by all reprogramming vectors was used to detect genomic integration. pCXWB-EBNA1 (Addgene: 37624) was used for positive control (10 µg) and only control sample is positive for EBNA sequence.

CHAPTER 3: RESULTS

3.1.6. Karyotype Analysis

Chromosomal abnormalities may occur during the reprogramming, whether the reprogramming procedure is episomal or viral [205]. KU-BVVL-iPSCs were sent to Koc University Hospital Genetics Diagnosis Centre for Karyotyping to analyze chromosomal integrity. No chromosomal abnormality was detected in karyotyping analysis of the select KU-BVVL-iPSCs (Figure 14).

3.1.7. Immunofluorescence Staining of Pluripotency Markers

Although KU-BVVL-iPSCs represent embryonic stem-cell-like morphology, I conducted immunofluorescence (IF) staining of pluripotency related proteins: octamer-binding transcription factor 4 (OCT4), stage-specific embryonic antigen 4 (SSEA4), and homeobox protein NANOG (NANOG), to test whether pluripotency related proteins are present in those cells. OCT4, SSEA4, and NANOG proteins are present in the KU-BVVL-iPSCs, proving that three pluripotency-related genes are active and proteins encoded by these genes are present in the cells (Figure 12,15,16).

3.1.8. Teratoma Formation Assay

During vertebrate embryonic development, cells of the inner cell mass form three primary layers of cells, which give rise to all an animal's organs and tissues. These three germ layers are named endoderm, mesoderm, and ectoderm. The potential to differentiate into the cells of the three germ layers is referred to as pluripotency. Being able to differentiate into cells of the three germ layers is the hallmark of pluripotency. Although KU-BVVL-iPSCs represent embryonic stem cell-like morphology and essential markers of pluripotency are present in the cells, I conducted a teratoma formation assay to test whether these cells are pluripotent. For this purpose, iPSCs were collected and injected into SCID mice intramuscularly. Animals were sacrificed when the teratomas reached 2 centimeters in their greatest dimension or at day 90, whichever comes first. Teratomas were sent for H&E staining to KUTTAM Koç University Hospital Laboratories. Cells that derive from ectoderm (neuroectodermal and pigmented epithelial cells), endoderm (gut-like and secretory epithelial cells), and mesoderm (adipocytes and chondrocytes) were present in the H&E stained samples of all cell lines, proving that KU-BVVL-iPSCs are pluripotent (Figure 17).

CHAPTER 3: RESULTS

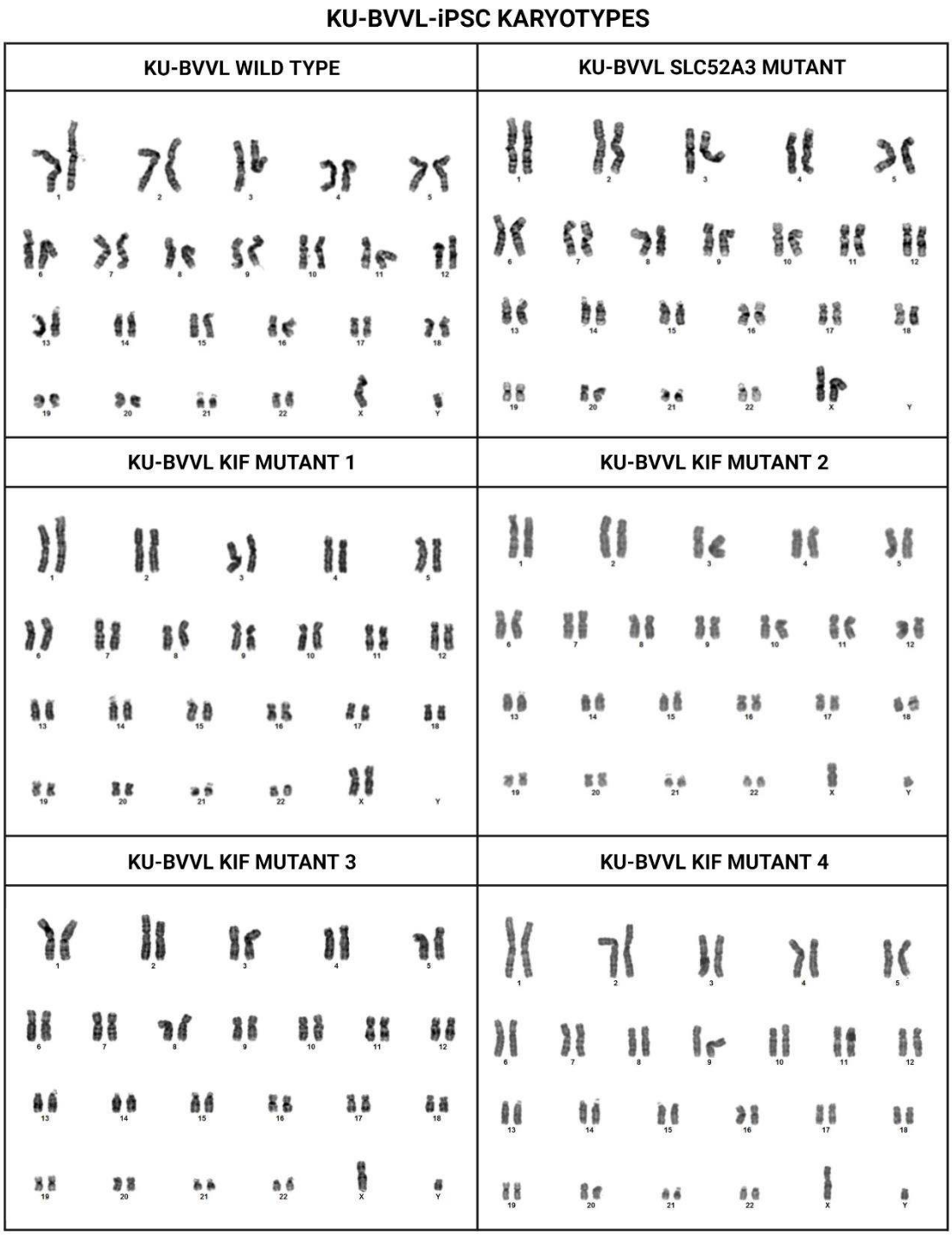

Figure 14: Karyotype analysis of KU-BVVL-iPSCs. All iPSCs included in the study have normal karyotype (44+XY or 44+XX).

CHAPTER 3: RESULTS

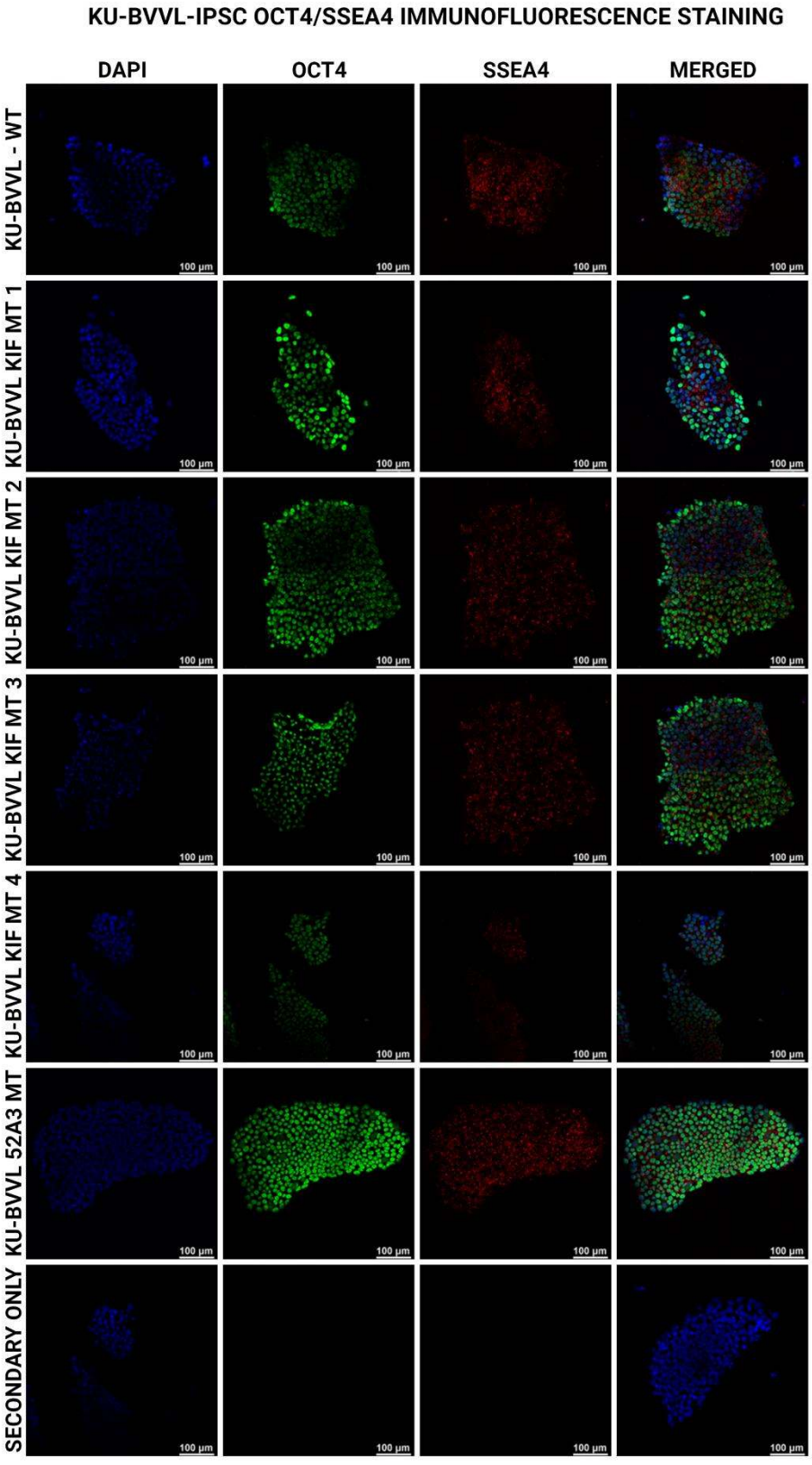

Figure 15: Immunofluorescence staining of KU-BVVL-iPSCs. Pluripotency related proteins Oct4 and SSEA4 are stained (Scale Bar: 100µm).

CHAPTER 3: RESULTS

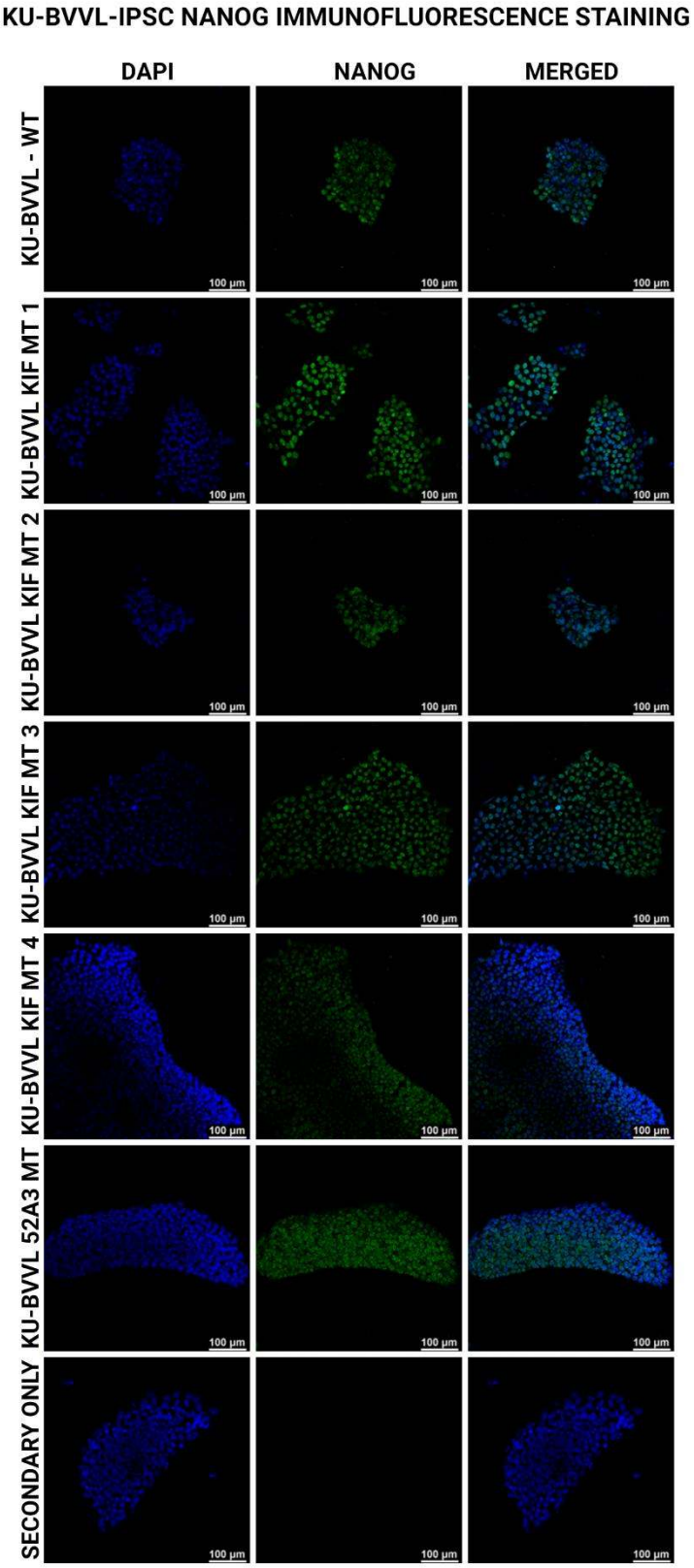

Figure 16: Immunofluorescence staining of KU-BVVL-iPSCs. Pluripotency related protein Nanog is stained (Scale Bar: 100µm).

CHAPTER 3: RESULTS

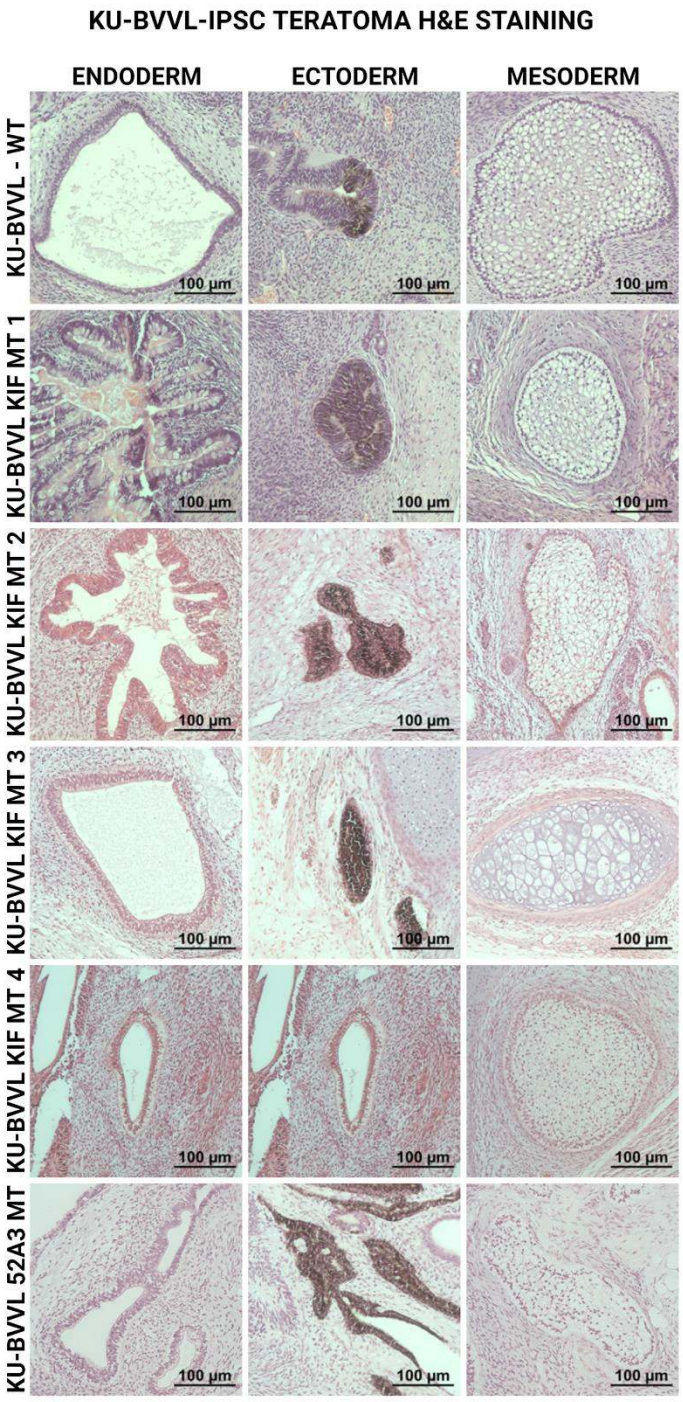

Figure 17: Teratoma formation after in vivo implantation of iPSCs into SCID mice. All three germ layers, including endoderm, mesoderm, and ectoderm, are observed in the teratoma (Scale Bar: 100µm).

CHAPTER 3: RESULTS

3.2. Generation & Characterization of Patient-Specific Motor Neurons

I aimed to establish a neuronal differentiation protocol to be used as a stable source of patient-specific neurons, preferably motor neurons, considering the nature of BVVL disease.

The MN Differentiation protocol I established is based on Du et al.'s small-molecule-based MN differentiation protocol, which is based on the use of different small-molecule combination cocktails, added on a simple base medium throughout different stages of differentiation [162]. This protocol also contains two different MN specification stages following the Neural Induction stage, enabling us to specify Motor Neuron Progenitor (MNP) lineage, between Caudal (lower motor neuron) and, Rostral (upper motor neuron). These MNPs can be expanded for three passages and can be differentiated into highly pure MN populations, with low numbers of glial cells present in the population. I modified this protocol according to our optimization experiment results and experimental needs at four different stages, covering the whole differentiation process (Figure 18).

CHAPTER 3: RESULTS

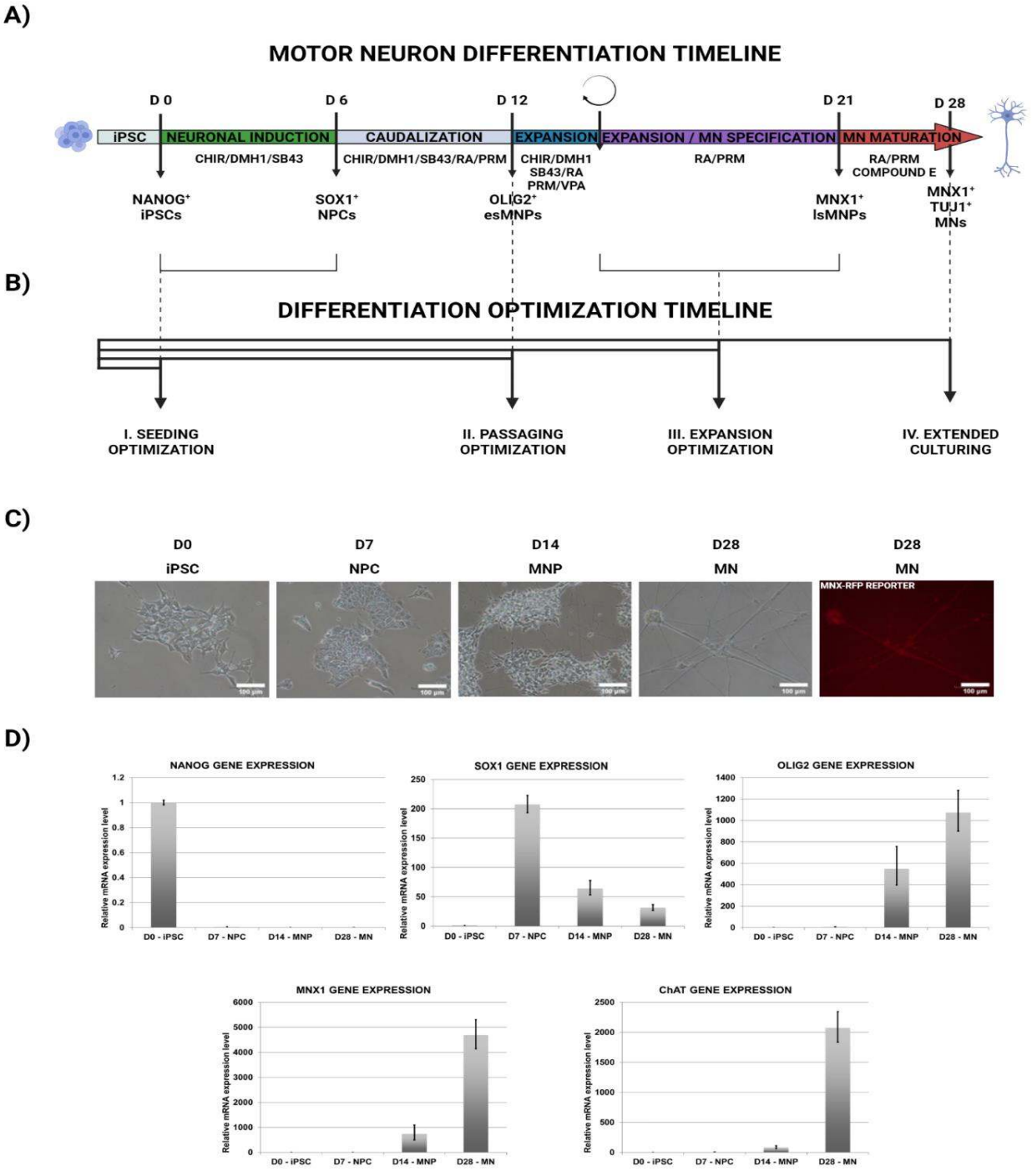

Figure 18: Experimental timeline for the generation of patient-specific motor neurons. **A)** Motor neuron differentiation timeline. **B)** Differentiation optimization timeline, aligned to corresponding critical stages of differentiation. **C)** Bright-field and fluorescent microscopy images of a KU-BVVL iPSC line throughout the differentiation procedure. RFP signal was observed in MNPs transduced with MNX1-RFP reporter construct (Scale Bar: 100µm). **D)** RT-qPCR results conducted during pilot differentiation experiments using WT-KU-BVVL iPSC Line. Results provide a baseline for characterization of KU-BVVL iPSCs throughout iMN differentiation process.

CHAPTER 3: RESULTS

3.2.1. Optimization of Motor Neuron Differentiation Method

Each stage from iPSC generation to final maturation contributes to interindividual interclonal variability. Optimization and standardization of each step in a differentiation protocol are essential for generating reproducible in vivo disease models. I addressed the sources of variance in two subjects:

I. Interindividual and interclonal variability of iPSCs: Although not preventing iPSCs from fulfilling criteria for pluripotency, variability occurs between iPSC lines from different donors as well as iPSC lines from the same donor. Factors such as genetic stability and experimental variability contribute to interindividual and interclonal variability by influencing differentiation potency, cellular heterogeneity, morphology, transcript, and protein abundance. These factors may influence the reprogramming stability, differentiation efficiency, and proliferation rates of iPSCs. Interindividual and interclonal variability could hinder the efforts to generate reproducible in vivo disease models in the absence of appropriate experimental strategies [206, 207].

II. Culture Conditions: Although highly efficient, differentiation methods are not 100% efficient, as it is unlikely to initiate differentiation simultaneously in every cell in the culture. Disease-causing gene mutations may further lower differentiation efficiency or cause premature death of cells of interest in the bulk population. Optimization of culture conditions is essential to minimize the variance and maintain a pure cell population, which ultimately influences the level of representation of the diseased phenotype [152, 199].

CHAPTER 3: RESULTS

3.2.1.1. Seeding Optimization of the iPSCs

The proliferation rate of the iPSC lines may vary, and the neuronal induction stage of the motor neuron differentiation protocol is six days long, which could affect differentiation efficiency. A six-day culture in the same well could harm differentiation efficiency as, when compared to the slow dividing cells, overcrowding of fast-dividing cells could affect differentiation rate and cause mis-differentiation.

To elucidate the possible effect of varying seeding density and proliferation rates on differentiation, BVVL-WT-iPSCs were seeded on Matrigel-coated 6 well plates at concentrations of $1x10^6$ and $2x10^6$ and incubated for 24 and 48 hours prior to initiation of the neuronal induction.

At Day 6 The *SOX1* gene expression was observed, and the *NANOG* gene declined, although it did not diminish at all wells that underwent neuronal induction. The most drastic change in gene expression pattern was observed in the wells with $1x10^6$ initial cell concentration and incubated for 24 hours. The most robust *SOX1* Gene expression was observed in this group, along with the most extensive downregulation of the pluripotency marker *NANOG* gene (Figure 19). This result suggests that neuronal induction and starting iPSC concentration of $1x10^6$ yields the highest differentiation efficiency at this setting.

CHAPTER 3: RESULTS

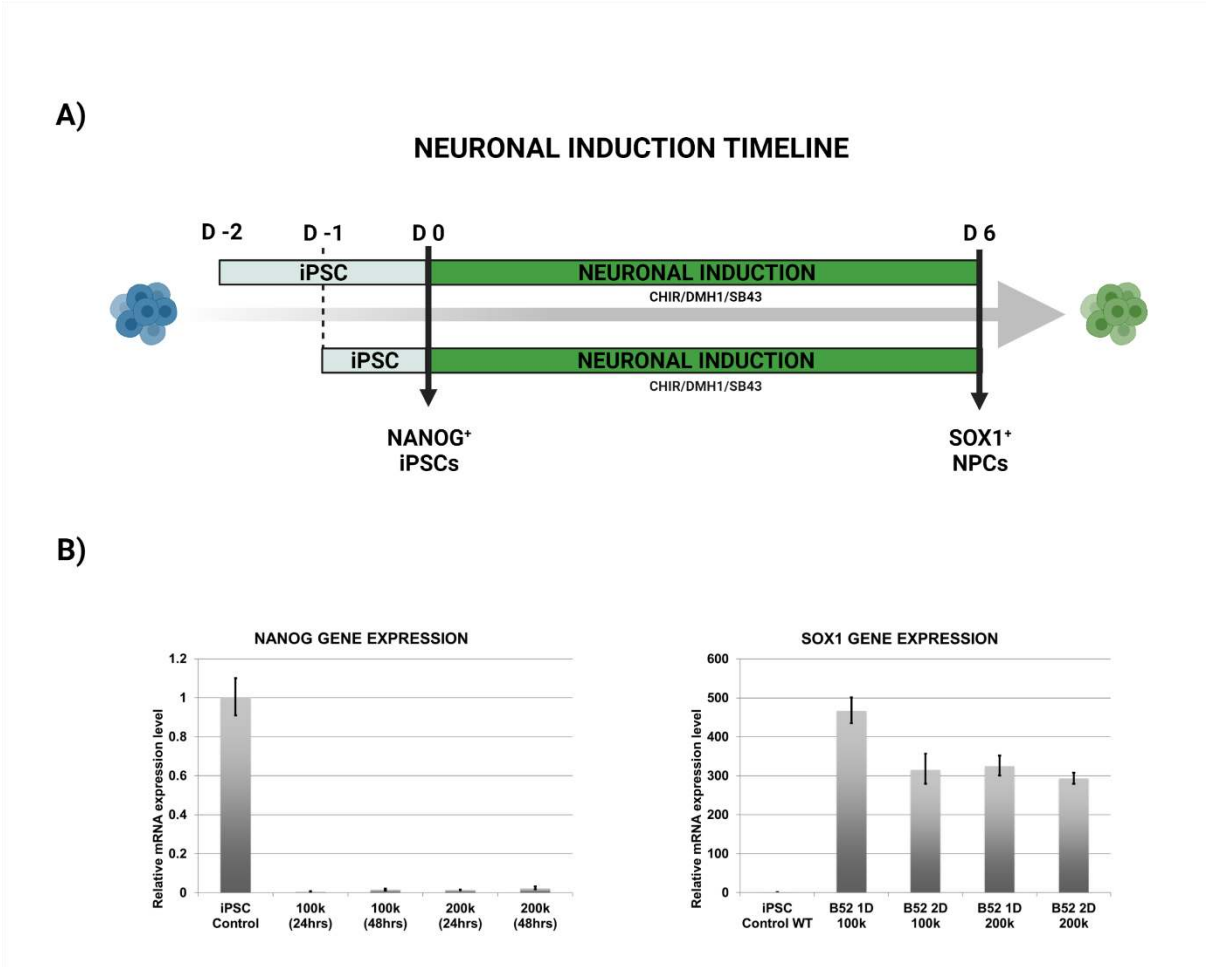

Figure 19: Neuronal induction optimization experiment. **A)** Neuronal induction timeline. **B)** RT-qPCR Results of the Neuronal Induction Initial Seeding Experiment. Relative gene expression levels of NANOG. B) Relative gene expression levels of SOX1 (n=3).

3.2.1.2. Optimization of the Passaging

I have observed several obstacles during culturing and expansion of the NPCs and MNPs. First, the effect of the differential proliferation rate of the iPSCs carried on with NPCs and MNPs. Second, when I used Dispase as a dissociation medium during passaging, I have observed excessive cell death and slowing down in the proliferation of the passaged cells. Third, related with the previous issue, NPCs and MNPs prematurely differentiated into neurons or mis-differentiated into other cell types, in cases where those cells dispersed in the culture too sparse or too dense, respectively, hindering the efforts to passage and expand MNPs while maintaining their undifferentiated status. In addition, unlike Accutase and Trypsin, Dispase dissociates cells as clusters which could hinder the efforts to generate stable gene expressing cell lines in downstream applications as cells do not distribute homogeneously. Homogenous transduction of cells is unlikely for a cluster of cells compared to cells dispersed singularly.

To overcome all the mentioned obstacles, I tested Accutase, Dispase, and Trypsin as cell dissociation reagents and optimized the passaging procedure. In addition, I also tested the short-term (24 hours) effect of Rho-associated, coiled-coil containing protein kinase (ROCK) -specific inhibitor Y-27632 (Y compound) to test whether its use significantly improves cell survival and proliferation rate.

I passaged the NPC populations during general differentiation experiments at the end of the Neuronal Induction stage 1:6 in ratio, on Day 6. I did not attempt to dissociate those cells completely and count the cells at this stage in order not to adversely affect cell viability or the differentiation process. However, I have adjusted the 1:6 passaging to achieve similar cell density between the different cell lines to standardize the differentiation process among them.

I have passaged the slowing dividing cell population NPCs 1:6 in ratio. I have attempted to achieve standardization across cell lines by passaging the slowest dividing cell line 1:6 in ratio and achieving similar confluency with the other relatively faster-dividing cell lines. MNPs are resistant to fluctuations in seeding density. MNPs at 80-85% confluency can be passaged in 1:4 to 1:9 ratio. As previously mentioned, MNPs prematurely differentiate into neurons or mis-

differentiate into other cell lines in cases where those cells disperse in the culture too sparse or too dense, respectively.

I have optimized the passaging condition for NPCs and MNPs by testing the effect of passaging MNPs using Accutase, Dispase, and Trypsin. In addition, I have tested the effect of 10 µM Y-Compound on the passaging outcome. I assessed the two qualitative variables; maintaining characteristic early-stage MNP morphology with few neurite formation and confluency in 7 Days as the determinant factors of successful outcome in this experiment (Figure 18-C).

Ranging from 0-100%, the success rate of passaging varied greatly between experimental settings. When applied for the first 24 hours following the passaging, ROCK-inhibitor Y-Compound improved cell viability with all three dissociation reagents. Moreover, MNPs in the Y-Compound treated wells retained their healthy morphology the following day compared to other wells, which required one to three days to retain their healthy morphology, following the passaging. In our experimental settings, Accutase was the most efficient one for passaging MNPs, with a higher survival rate and fewer morphological changes among all three dissociation mediums. Although the survival rate of the passaged MNPs was at desirable levels, MNPs passaged using Trypsin presented more neurite formation, an undesired outcome during MNP expansion. Among the three dissociation reagents, Dispase was the least efficient one. None of the Dispase passaged MNPs met our criteria for successful passaging. Almost all MNPs died following the passaging using Dispase and without Y-Compound application, and the MNPs passaged using Dispase and with Y-Compound treatment failed to expand as rapidly as MNPs passaged using Accutase. These results indicate that using Accutase as a dissociation reagent and supplementing the culture medium with 10 µM Y-Compound is the most efficient and stable method of passaging the NPCs and MNPs (Figure 20).

CHAPTER 3: RESULTS

A)

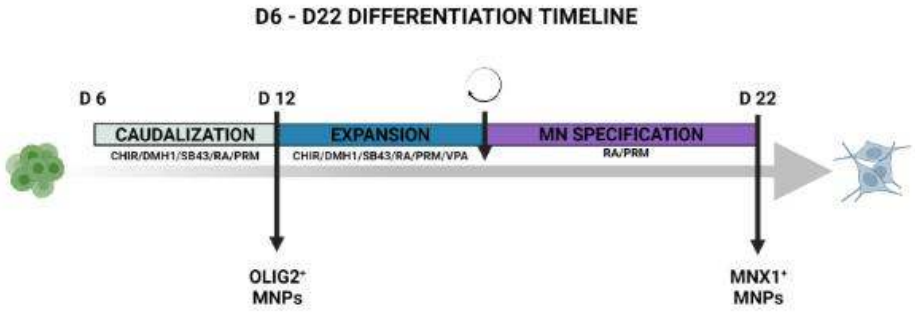

B)

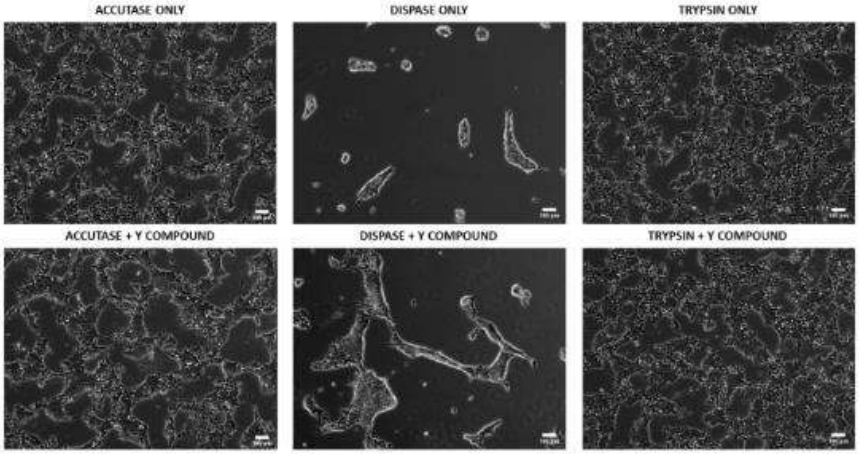

C)

Experiment	Accutase		Dispase		Trypsin	
	- Y	+Y	- Y	+Y	- Y	+Y
1	✔	✔	✘	✘	✔	✔
2	✔	✔	✘	✔	✔	✔
3	✘	✔	✘	✘	✘	✔
4	✘	✔	✘	✔	✘	✘
5	✔	✔	✘	✘	✘	✘
6	✘	✔	✘	✘	✘	✔
Succes Rate (%)	50%	100%	0%	33%	33%	67%

D)

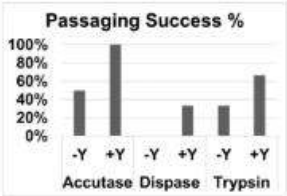

Figure 20: Passaging optimization experiment timeline and results. **A)** D6 – D22 Differentiation timeline, during which passaging of the NPCs and MNPs are required. **B)** Phase contrast images of MNPs 24 hours after the passaging (Experiment-2, Scale Bar: 100µm). **C)** Passaging success evaluation table of the six MNP passaging optimization experiments. **D)** Passaging success rate the six MNP passaging optimization experiments.

3.2.1.3. Expansion Optimization & Extended Culturing Optimization

Recapitulation of the disease phenotype in vitro relies on successful differentiation and maturation of the MNPs as electrophysiological and global gene expression patterns vary greatly between mature and immature cells. Many experimental setups require extended culturing of the neuronal cell lines. Considering these, I wanted to test whether iMNs could be cultured for extended periods of time and mature to enable long-term experiments.

Motor neuron and pancreas homeobox 1 (MNX1), also known as Homeobox HB9 (HLXB9), is a transcription factor and a key marker of the MN lineage [208]. To visualize the *MNX1* expression, I have transduced the WT KU-BVVL-iMNs with a lentiviral MNX1:RFP reporter construct. I have observed that MNP population begins to express MNX1 as they expand in the expansion medium. As expected, switching to MN maturation medium further increased the number of $MNX1^+$ MNPs (Figure 21, App. Figure 2).

I have successfully differentiated OLIG2+ early-stage MNPs (esMNPs) into $MNX1^+$ late-stage MNPs (lsMNPs) and $ChAT^+$ mature iMNs in 17 Days (equal to Day 28 of the “Differentiation Timeline”) following esMNP seeding. Regardless of the genetic background, axon length and diameter significantly improved over time of all KU-BVVL-iMNs. However, I have observed the emergence of a population of fast-dividing, presumably non-neuronal, cells during extended culture (Figure 22).

Considering the relatively longer proliferative period, morphology, and the NPC/MNP origin of the cells, the expression of the glia-specific “Glial Fibrillary Acidic Protein” GFAP within these cell populations were tested. *GFAP* expression was detected in the long-term cultured MN populations, which were cultured over three weeks following esMNP seeding. Interestingly, although I observed MN formation in the glial cell containing wells, relative expression levels of *OLIG2*, *MNX1,* and *ChAT* genes were significantly reduced. This may be a result of the dilution of the RNA originating from the cells of the neuronal lineage or misdifferentiation of MNP due to down-regulation of *OLIG2*, a transcription factor known for determining motor neuron and oligodendrocyte differentiation (Figure 23) [209].

CHAPTER 3: RESULTS

To minimize $GFAP^+$ cell generation and maximize the efficiency of MN Differentiation protocol, I have limited MNP expansion to three passages and designed an optimized experimental template, which approximately achieves amplification of a single iPSC to 10^4 throughout the process and 10^8 if MNPs expanded for two passages and provides enough cells for the characterization and functional experiments such as RT-qPCR, immunofluorescence staining, BioID protein tagging, and glutamate-induced toxicity experiments. The optimized experimental template further standardized our differentiation protocol. In addition, this protocol also decreased the number of $GFAP^+$ cells significantly during long-term culturing but failed to prevent their emergence completely (Figure 24).

CHAPTER 3: RESULTS

3.2.2. Characterization of Patient-Specific Induced Motor Neurons

Following the optimization steps, I simultaneously generated four patient-specific iMNs, from the following iPSC lines: KU-BVVL-WT, KU-BVVL-KIF-MT3, KU-BVVL-KIF-MT4, and KU-BVVL-52A3-MT. On day 28 of the differentiation KU-BVVL iMNs I have isolated RNA and prepared iMN on coverslips for immunofluorescence staining.

Regardless of the genetic background, *MNX1*, and *ChAT* genes were expressed on day 28 KU-BVVL-iMNs. In addition, all differentiation stage-specific marker genes were expressed in KU-BVVL iPSC-derived cell lines throughout the differentiation process (Figure 25).

Immunofluorescence staining with antibodies against motor neuron and pancreas homeobox 1 (MNX1), class III beta-tubulin (TuJ1) revealed that Day 28 cell populations consist of neurons with a considerable amount of $MNX1^+$ motor neurons (Figure 26).

In addition, to establish whether differentiated MNs can be used for KIF13A-mutation related disease modeling, I investigated the expression and intracellular localization of KIF13A via immunofluorescence. I observed that KIF13A protein is abundantly present in iMNs. Interestingly, KIF13A was predominantly in the soma and dendritic regions, but not limited to those. In addition, I have observed KIF13A protein presence in the axonal region, suggesting a role for KIF13A in somatic and axonal pathways (Figure 27).

CHAPTER 3: RESULTS

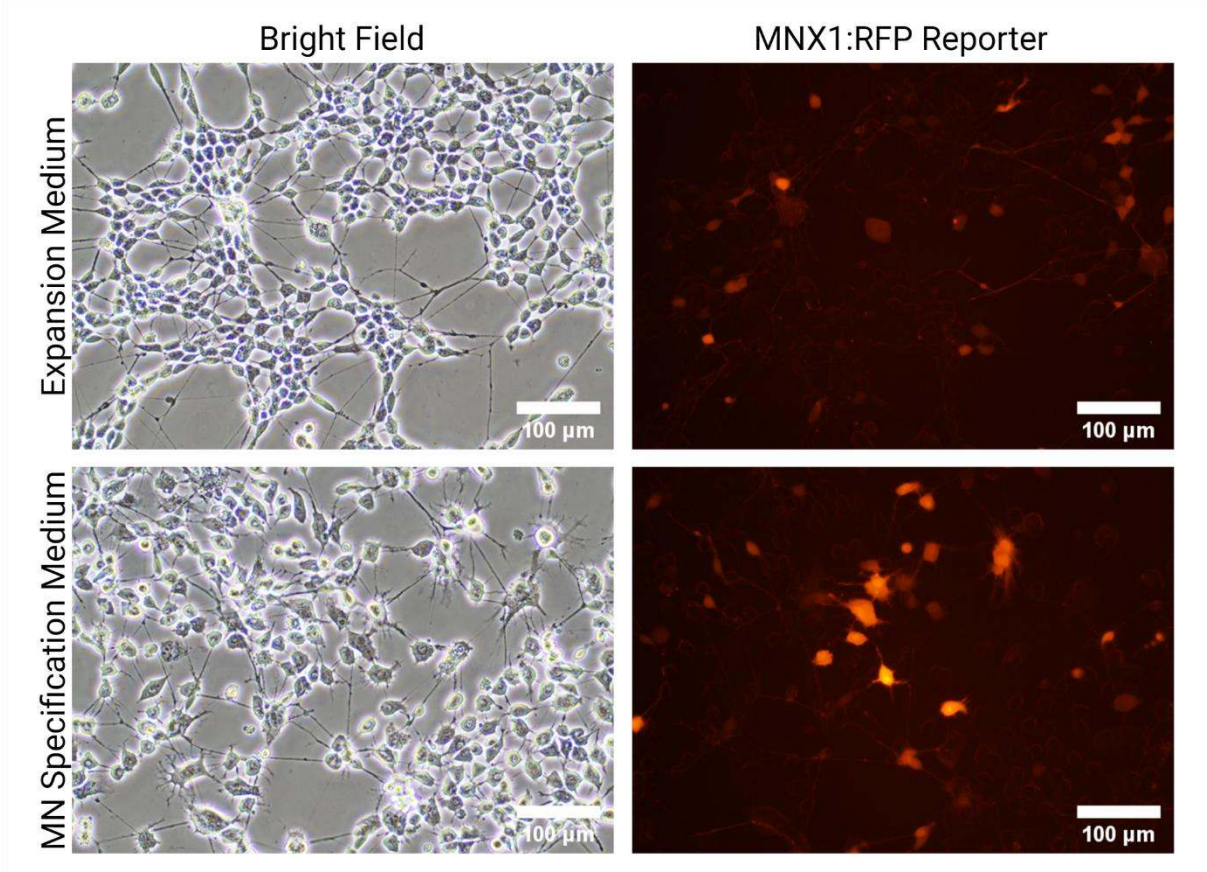

Figure 21: Bright field and fluorescence microscopy images of WT KU-BVVL-MNP transduced with lentiviral MNX1:RFP reporter construct. MNP populations under expansion condition begin to express MNX1 as we expand them using expansion medium. Switching to maturation medium further increase the number of MNX1+ MNPs (Scale Bar: 100µm).

CHAPTER 3: RESULTS

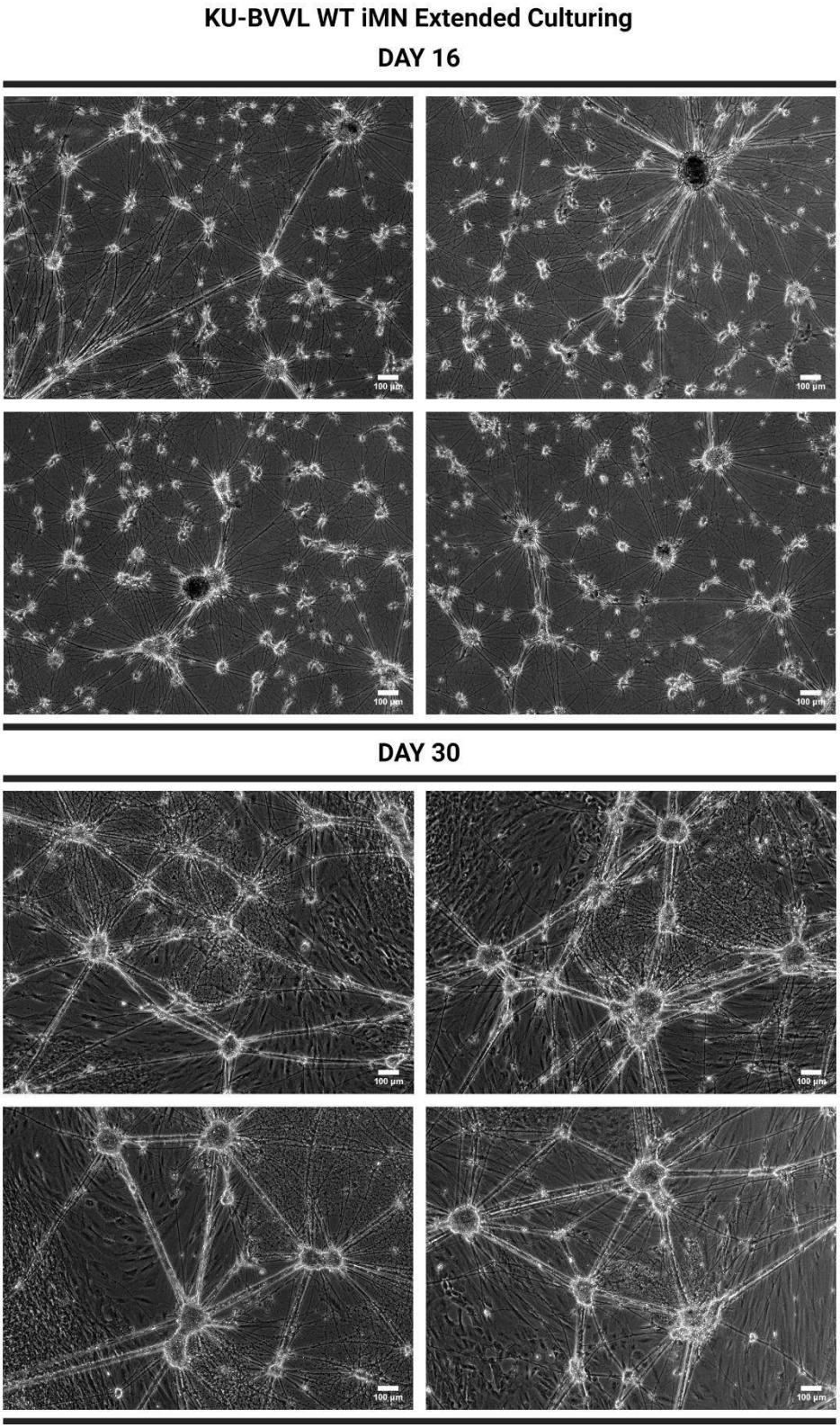

Figure 22: Phase contrast images of Day 16 & 30 KU-BVVL WT iMNs. Axon length and diameter significantly improved over time of all KU-BVVL-iMNs. However, we have observed fast-dividing distinctly different cells become apparent on the background as culturing time extends.

CHAPTER 3: RESULTS

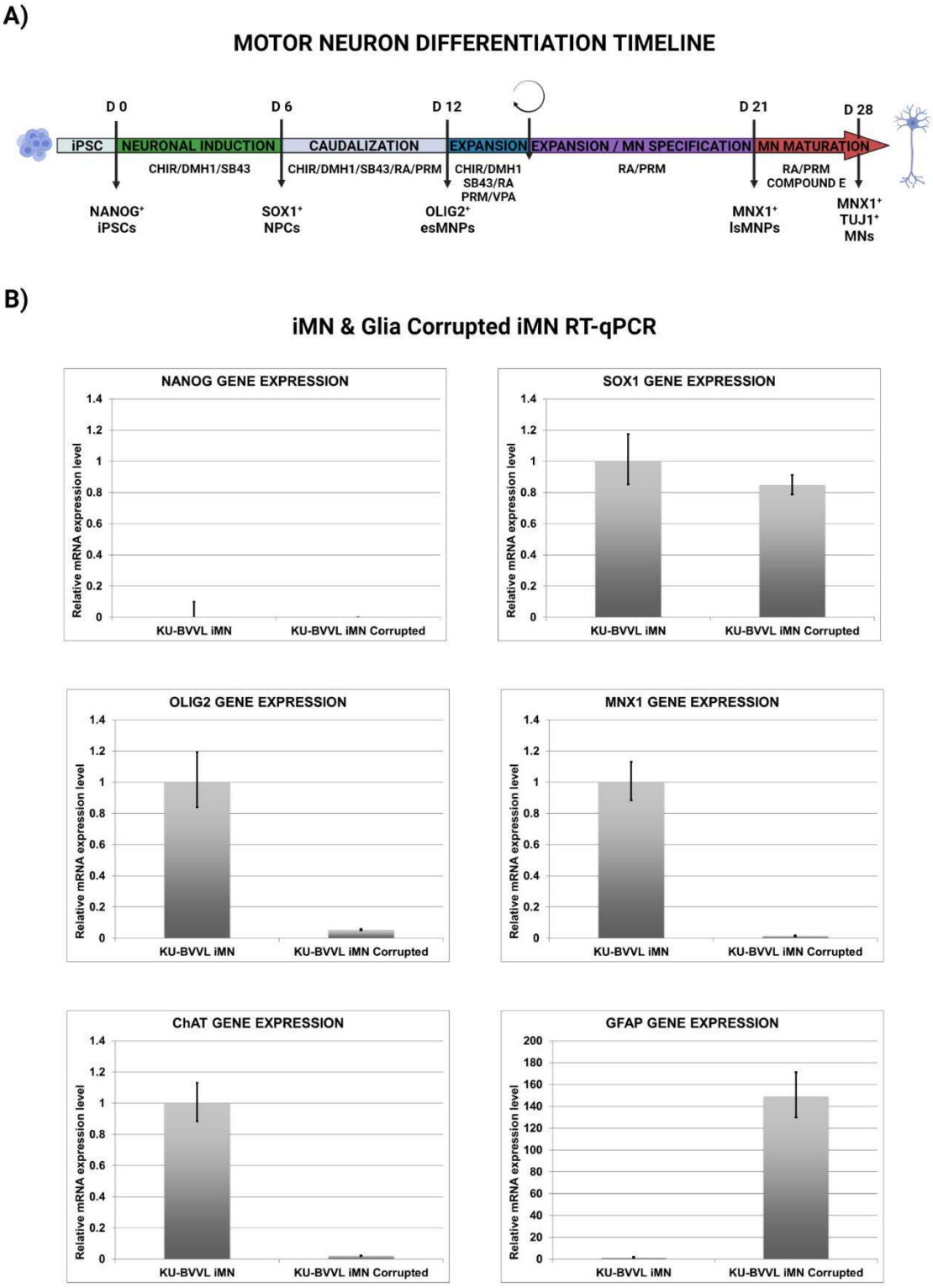

Figure 23: Comparative RT-qPCR results of KU-BVVL iMN and KU-BVVL iMN Corrupted. **A)** Motor neuron differentiation timeline. **B)** Comparative RT-qPCR results of KU-BVVL iMN population without glial infestation and population with glial infestation referred to as KU-BVVL iMN and KU-BVVL iMN corrupted, respectively.

CHAPTER 3: RESULTS

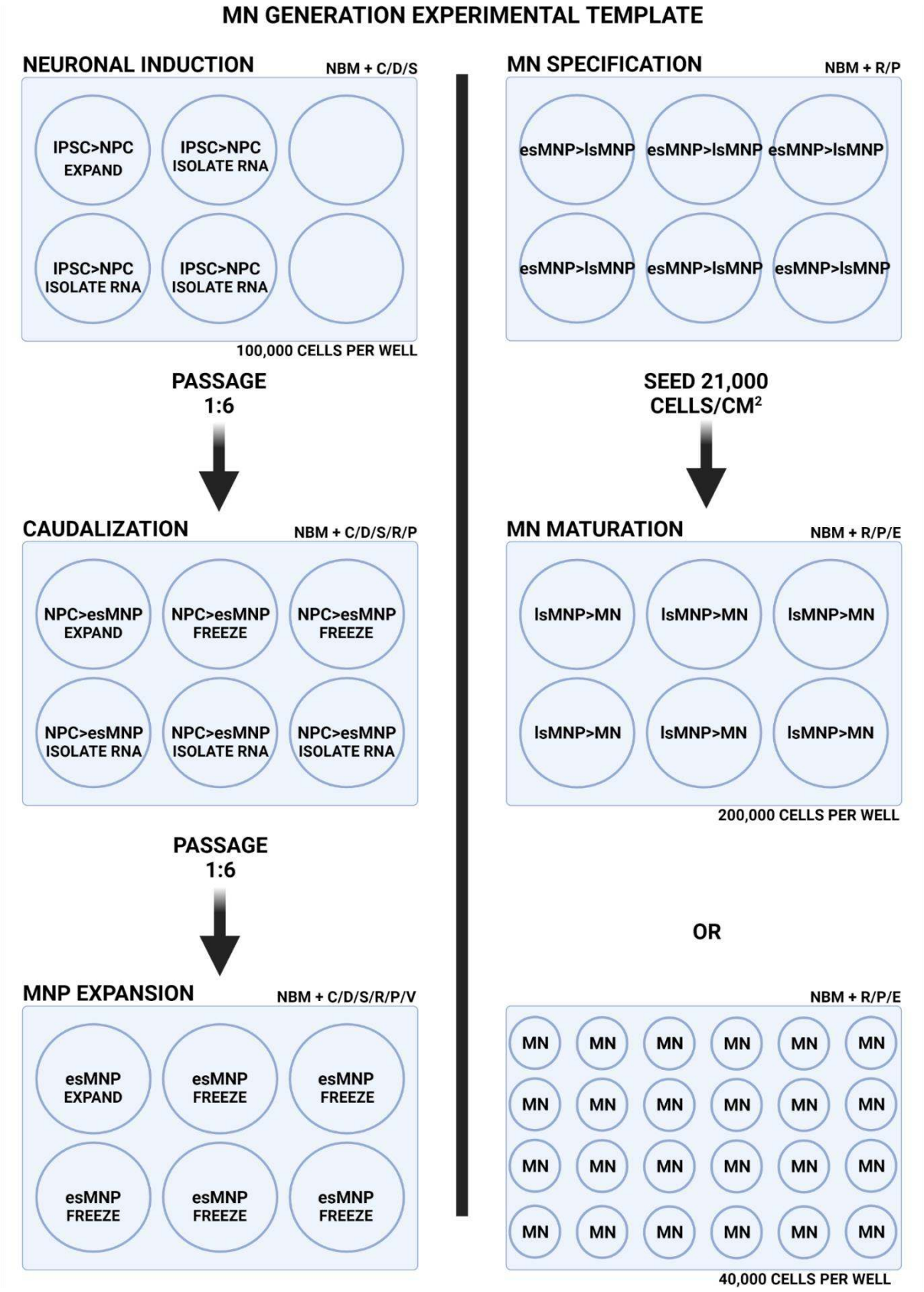

Figure 24: Optimized experimental differentiation template. We have designed an optimized experimental template, which provides enough cell count for the characterization and functional experiments.

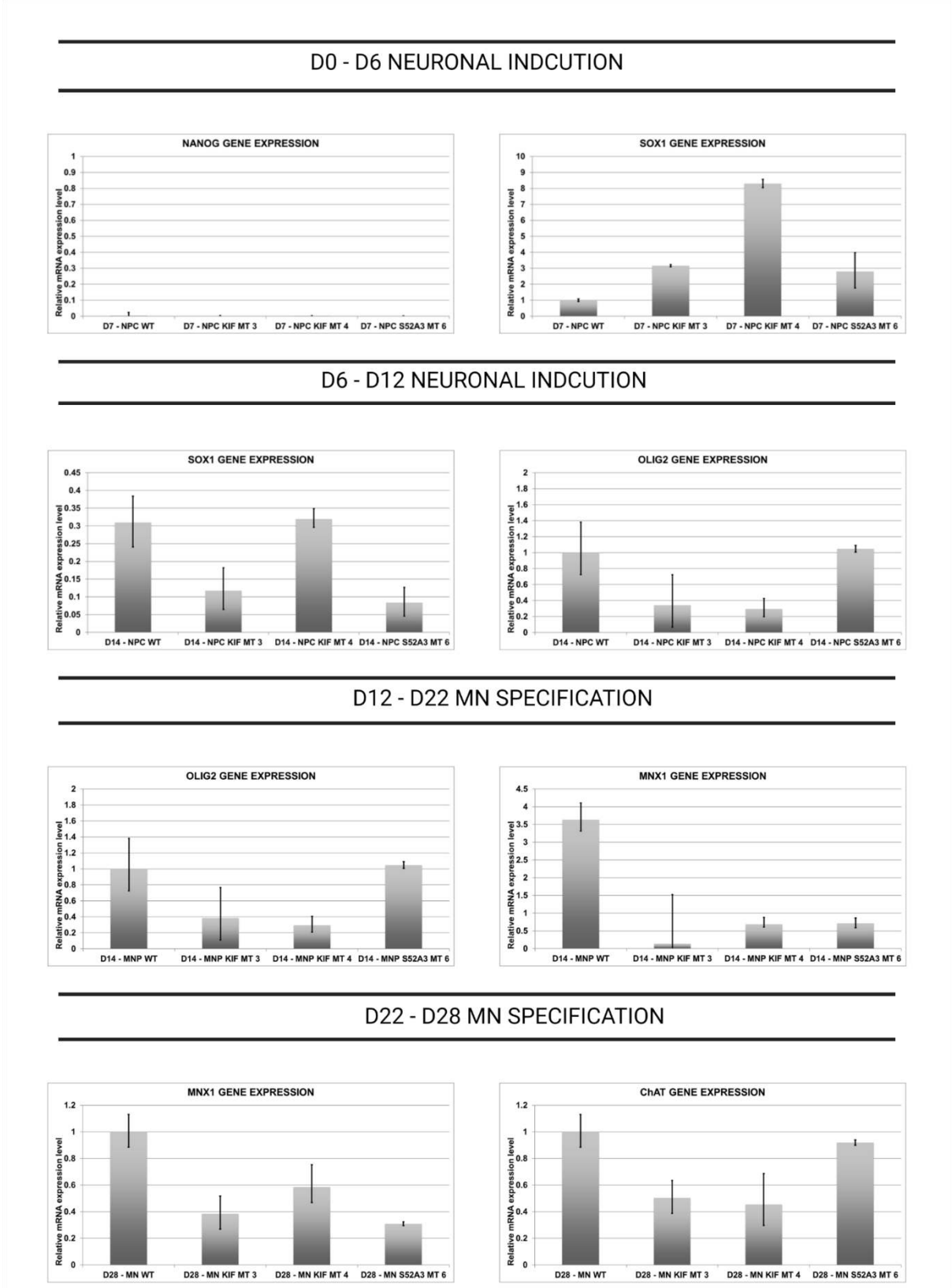

Figure 25: Gene expression pattern of KU-BVVL cell lines of throughout the MN Differentiation process. Initial KU-BVVL WT differentiation cDNA samples were used as positive control and results normalized to the RT-qPCR result of a cell with positive expression value for each differentiation stage (n=3).

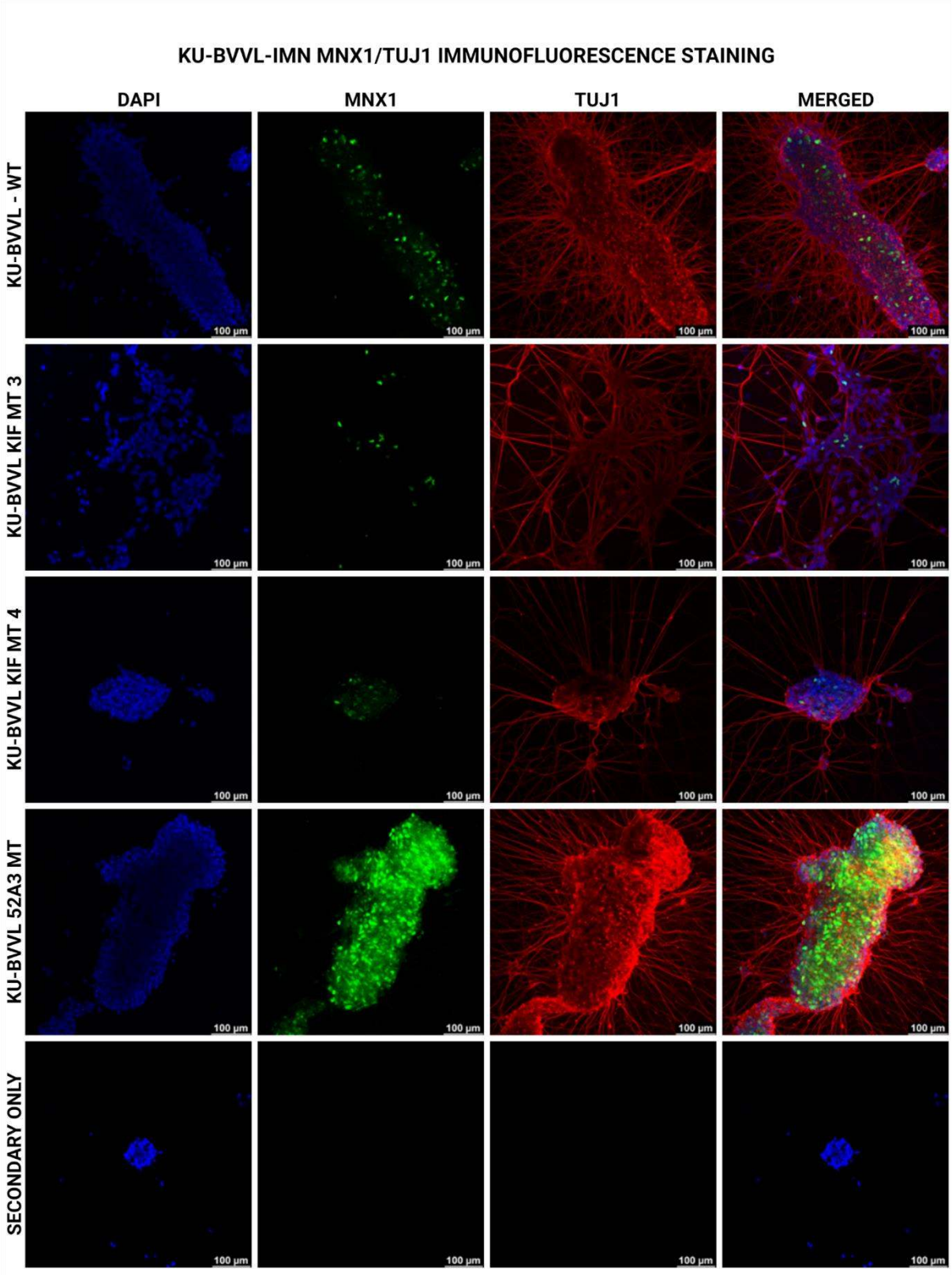

Figure 26: Immunofluorescence staining of KU-BVVL-iMNs. Motor neuron specific protein MNX1 and generic neuron protein TUJ1 are stained (Scale Bar: 100µm).

CHAPTER 3: RESULTS

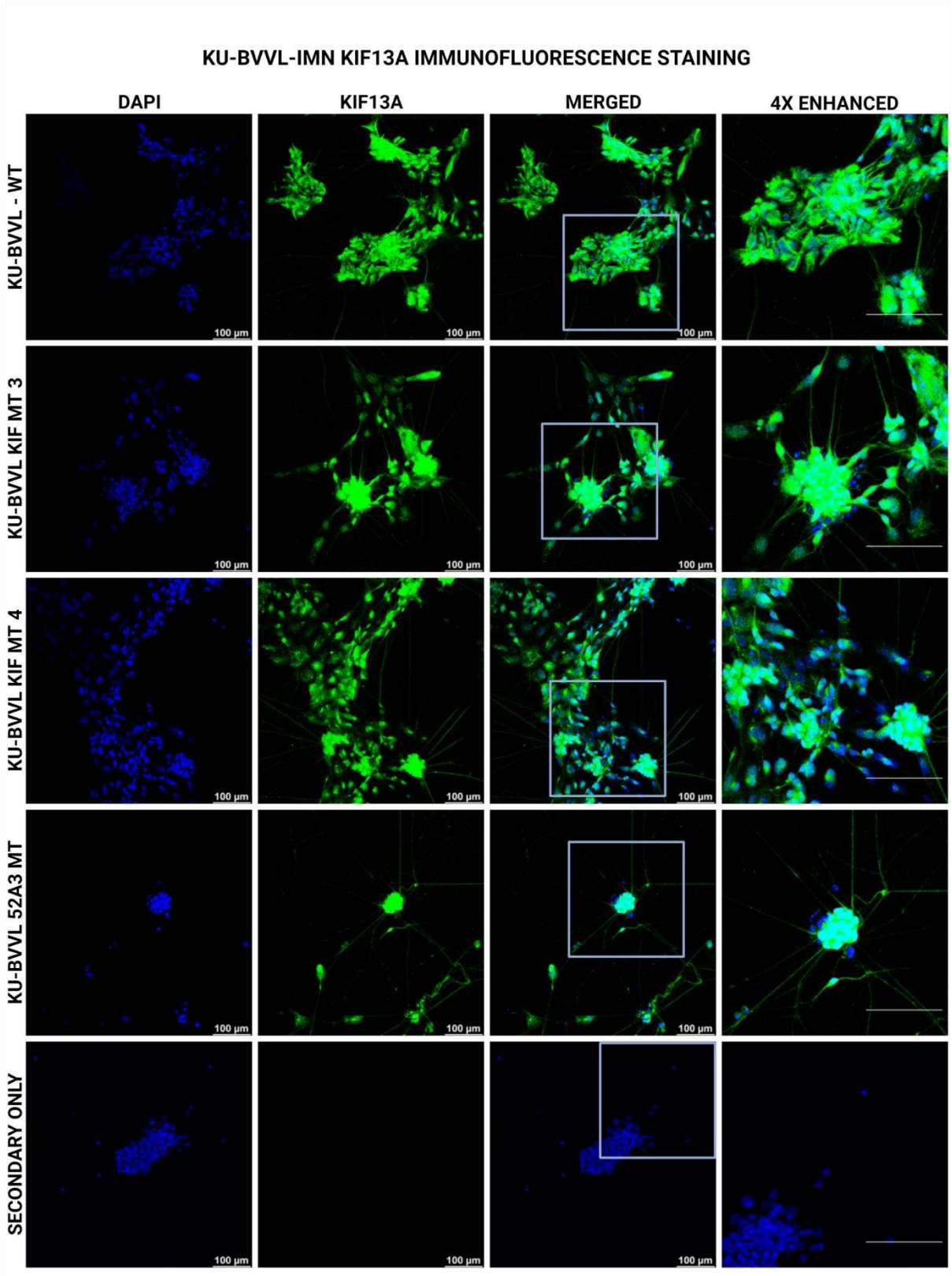

Figure 27: Immunofluorescence staining of KU-BVVL-iMNs. KIF13A protein is stained. (Scale Bar: 100µm, Scale Bars of 4X ENHANCED panel was simplified to make them less obscurant).

CHAPTER 4: DISCUSSION

The Brown-Vialetto-Van Laere syndrome (BVVL) is a rare neurological disease characterized by progressive bulbar palsy, with sensorineural deafness.

Although the unique clinical characteristics of this disease have been described at the end of the 1800s, the first clues regarding the genetic cause of BVVL were revealed when solute carrier family 52 (SLC52) member gene mutations were discovered in BVVL [82, 83]. SLC52 family proteins are responsible for dietary uptake and transportation of riboflavin (Vitamin B2), which is a key molecule in an aerobic cell since flavoproteins are crucial for mitochondrial function, oxidative phosphorylation, and oxidative stress reduction. Deficiencies in riboflavin uptake and transport result in mitochondrial dysfunction by reduced energy levels and oxidative stress reduction [84].

In line with these progressions, it was also discovered that high dose intravenous riboflavin application halted and, up to some point, reversed the progression of neurodegeneration in BVVL patients. As a result, BVVL has become the first treatable ALS-like disease [85].

Currently, the only known cause of BVVL is riboflavin deficiency, which is linked to mutations in Solute carrier 52 family proteins, also known as riboflavin transporter proteins. Interestingly, although all KU-BVVL patients responded favorably to riboflavin treatment and had marked improvements in their complaints, no mutations were detected in *SLC52A2/3* genes with whole-exome sequencing (WES).

However, mutations in the SLC52 family genes are not found in a fraction of the patients who are clinically diagnosed with BVVL, suggesting that there may be other genes involved in the pathophysiology of BVVL.

CHAPTER 4: DISCUSSION

To identify the genetic mutation in this family; whole-exome sequencing (WES) and homozygosity mapping were carried out at the Koç University Suna and İnan Kıraç Foundation Neurodegeneration Research Laboratory (Figure 2).

WES and homozygosity mapping, supported with in silico analysis, revealed a novel mutation in *KIF13A gene*, encoding Kinesin-3 family member KIF13A protein, with a possible pathogenic single nucleotide variation (SNV). Detected SNV results in amino acid change "p.Glu1656Lys". A high GERP score of 6.0799 suggests that this variation might be in an evolutionary constrained site. In addition, the DANN algorithm labelled this variant as non-functioning, and the effect of this variation was reported as damaging (adversely affecting the protein function) in SIFT predictive model (Figure 3, Table 1).

Considering the deficiency of riboflavin transport and metabolism observed in BVVL patients and the response of KU-BVVL patients to high dose riboflavin treatment, our approach revolved around generating patient-specific iPSCs to be able to rapidly differentiate these cells into the intestinal, vascular, and nervous system and develop in vitro cell models that accurately reflect the diseased phenotype. KIF13A mutation results in amino acid change "p.Glu1656Lys" in the tail region of the motor protein, which could affect its cargo transport capabilities. To reveal any possible alteration in protein-protein interaction of KIF13A caused by this mutation, I have designed and generated various, fluorescent-labeled riboflavin transporter proteins and Rab-GTPases, as well as KIF13A-BioID fusion constructs (Table 24). RNA-Sequencing could also be a useful tool as alterations in gene expression patterns could provide insight into affected pathways and how the cells are coping with possible affected pathways. The hurdle in this manner was to find the correct cell line, in this case, a neuronal subtype that could accurately reflect the diseased phenotype. KIF13A was expressed and abundantly present in KU-BVVL-iMNs, meaning they could be used as model cell lines accurately reflecting the diseased phenotype (Figure 27). Currently, neurodegeneration in BVVL patients is considered to be an outcome of riboflavin deficiency. Although mutations in the SLC52 family genes are not found in a fraction of the clinically diagnosed patients with BVVL, in many recent studies, BVVL is renamed and referred to as riboflavin transporter deficiency (RTD). Our results suggest that this disease could have a more complex etiology with multiple causative factors such as KIF13A tail region mutations. The expression vectors that we have generated along with KU-BVVL-iMNs will be important tools to understand KIF13A related processes and molecular mechanisms crucial for a healthy, functioning

nervous system. As for the future directions, we aim to use the set of tools that have been generated in this study to conduct BioID based analysis to reveal the KIF13A interactome (Table 24). We aim to conduct RNA-Sequencing to reveal differentially expressed genes to identify molecular processes affected by the novel “p.Glu1656Lys” KIF13A mutation. We aim to investigate the effect of the novel mutation on KIF13A mediated tubular endosome formation and the role of KIF13A on glutamate receptor distribution and cellular homeostasis (See “Future Directions” section).

CHAPTER 4: DISCUSSION

4.1. Generation & Characterization of Integration free Patient-Specific iPSC Lines

4.1.1. Generation of Integration-Free Patient-Specific IPSCs

The first iPSCs from BVVL patients were generated by Rizzo et al. in 2017. In this study, iMNs were derived from iPSCs generated from BVVL patients carrying SLC52A2 or SLC52A3 mutations. In that study, a reduction in axon elongation coupled with perturbations in neurofilament composition and reduced autophagic/mitophagic flux was observed [154]. In a recent study, Marioli et al. (2020) iMNs were derived from iPSCs generated from BVVL patients carrying SLC52A2 or SLC52A3 mutations. In that study, possible beneficial effects of several antioxidants Vitamin C, Idebenone, Coenzyme Q10, and EPI-743, either alone or in combination with riboflavin on the morphology and function of motor neurons derived from iPSCs generated from BVVL patients carrying SLC52A2 or SLC52A3 mutations [155].

In this study, I generated and characterized five iPSC lines from BVVL patients, one carrying a *SLC52A3* mutation and four carrying novel “Glu1656Lys” KIF13A tail region mutation. Our cohort also included iPSCs derived from the healthy sibling of the KIF13A mutant family. I generated iPSC lines with nucleofection of Yamanaka factors, an integration-free method (Figure 11,12). The reason for this is that disruption of the genomic integrity may result from the use of lentiviral and retroviral vectors. Except for the Sendai virus, the use of viral vectors leads to random integration of exogenous DNA into the genome. For disease modeling studies, this may disrupt the functionality of the important genes and hinder efforts to model or discover pathways that cause the disease [148]. On day 21 post-nucleofection, I began to observe newly forming iPSC colonies. I isolated and expanded the twelve embryonic stem cell-like colonies from each patient-derived fibroblast line, taking into consideration cell morphology and proliferation rate. During expansion, I narrowed this number to five clones for each patient, which were expanded and stocked (Table 22).

CHAPTER 4: DISCUSSION

4.1.2. Generated Wild Type and Mutant KU-BVVL iPSCs are Pluripotent

I conducted a series of characterization experiments on newly generated KU-BVVL-iPSCs to assess whether: (1) these cells still carry mutations of interest, (2) there is an integration of episomal vectors into the genome, (3) that pluripotency related proteins are present, (4) there is any chromosomal abnormality caused during the reprogramming procedure, and (5) these cells are pluripotent.

Although the genome of induced pluripotent stem cells (iPSCs) is thought to be identical to the source organism, in this case, our patients, genetic variations can be introduced into the iPSCs from different sources during iPSC generation and maintenance. I have re-validated the mutations that are revealed by whole-exome sequencing in KIF13A and SLC52A3 genes of the patient-specific iPSCs (Figure 9,10).

All our constructs used for reprogramming the fibroblast into iPSCs contain two components of the Epstein-Barr virus, OriP, and EBNA1, which not only serve to improve the reprogramming efficiency but also serve as a marker of the integration of OSKM vectors into the genome. Amplification of EBNA1 sequence was not detected in PCR conducted using KU-BVVL-iPSC gDNA, indicating genomic integrity was not compromised (Figure 13).

Chromosomal abnormalities may occur during the reprogramming, whether the reprogramming procedure is episomal or viral [205]. No chromosomal abnormality was detected in karyotyping analysis of the select KU-BVVL-iPSCs (Figure 14).

Expression of pluripotency-related ESC proteins OCT4, SSEA4, and NANOG in KU-BVVL-iPSCs were validated with Immunofluorescence (IF) staining (Figure 12,15,16). When intramuscularly injected into SCID mice, KU-BVVL-iPSCs formed teratomas containing endodermal, ectodermal, and mesodermal cells, meaning these cells are pluripotent (Figure 17).

CHAPTER 4: DISCUSSION

4.2. Generation & Characterization of Patient-Specific iMN Lines

4.2.1. Establishing a Motor Neuron Differentiation Method

I aimed to establish a neuronal differentiation protocol to be used as a stable source of patient-specific neurons, preferably motor neurons, considering the nature of BVVL disease.

MN Differentiation protocol I established is based on Du et al.'s small-molecule-based MN differentiation protocol, which is based on the use of different small-molecule combination cocktails, added on a simple base medium throughout different stages of differentiation [162]. This protocol also contains two different MN specification stages following the Neural Induction stage, enabling us to specify Motor Neuron Progenitor (MNP) lineage, between Caudal (lower motor neuron) and, Rostral (upper motor neuron). These MNPs can be expanded for three passages and can be differentiated into highly pure MN populations, with low numbers of glial cells present in the population. I modified this protocol according to our optimization experiment results and experimental needs (Figure 8). In addition, I have also generated KU-BVVL-NGN-iPSC lines stably expressing Neurogenin-2 (NGN2) under control of TetON promoter (Addgene: 52047, Zhang et al. 2013) as a precaution in case of small molecule approach failed or required additional interference to increase MN differentiation efficiency (App. Figure 3) [174].

Each stage from iPSC generation to final maturation contributes to interindividual interclonal variability. Optimization and standardization of each step in a differentiation protocol are essential for generating reproducible in vivo disease models. I modified Du et al.'s small-molecule-based MN differentiation protocol to minimize interindividual and interclonal variability. I addressed the sources of variance in two subjects: I. Interindividual and interclonal variability of iPSCs and II. Culturing Conditions.

I optimized passaging and culturing conditions and established an optimized experimental template, which approximately achieves amplification of a single iPSC to 10^4 throughout the process and 10^8 if MNPs expanded for two passages and provides enough cell count for the characterization and functional experiments such as RT-qPCR, immunofluorescence staining,

CHAPTER 4: DISCUSSION

BioID protein tagging, and glutamate-induced toxicity experiments. I have alternated the suspension culture during the MN Specification stage to adherent culture. This transition allowed us to conduct more standardized differentiation as it enabled us to seed MNPs in a single cell manner. More importantly, switching to adherent culture during MNP Specification enables us to conduct transduction of lentiviral constructs or, in combination, perform antibiotic resistance-based selection, which is not feasible in 3D-Suspension culture. I have observed neurite formation following the passaging during the expansion of the MNPs, suggesting that MNPs are obtaining MN-like morphology. Neurite formation intensified as the passage number of MNPs increased. The expression of *OLIG2*, a transcription factor, a relatively early marker of lower motor neuron lineage, known for determining motor neuron and oligodendrocyte differentiation, was also down-regulated in MNP populations passaged for more than three passages and in populations where Glia-like cells emerge. Suspecting the possibility of the loss or reduction of *OLIG2* gene expression as the cause of MNP misdifferentiation, MNP expansion was limited for three passages to minimize loss or reduction *OLIG2* expression. This protocol decreased the number of $GFAP^+$ cells significantly during long-term culturing but failed to prevent their emergence completely (Figure 24). Differentiation efficiency can be further increased by using Neurogenin-2 (NGN2) under control of TetON promoter (Addgene: 52047, Zhang et al. 2013) in combination with the small-molecule-based differentiation method [174]. Stably expressing the TetON NGN2 can be generated by short-term activation of NGN2 under the control of TetON promoter. Activation of NGN2 was not sufficient to initiate irreversible differentiation during our experiments in three days. However, it provided enough time to conduct selection with puromycin resistance gene carried in TetON NGN2 construct.

Although highly efficient, differentiation methods are not 100% efficient, as it is unlikely to initiate differentiation simultaneously in every cell in the culture. Disease-causing gene mutations may further lower differentiation efficiency or cause premature death of cells interest in the bulk population of cells. Importantly, all the cells undergoing differentiation are at a different stage, and if they survive, cells with the diseased genome are at a different stage of neurodegeneration due to the fact that the neurodegenerative process or deficit is present for a varying period. Due to that, each individual cell in the heterogenous bulk population is actually a different individual at a different stage of the disease. Due to that, without sorting the bulk population, cells could obscure the early markers of neurodegeneration or early cope-up mechanisms in the cells, which could be possible therapeutic targets. However, this could be used for our advantage as if all individual cells are at varying stages of neurodegeneration.

CHAPTER 4: DISCUSSION

If single-cell sorted and RNA-sequencing is conducted, sample size increases from hundreds to hundred thousands. This phenomenon was observed and exploited by Lang et al. in 2019. Lang et al. demonstrated how single-cell transcriptomics could exploit cellular heterogeneity to reveal disease mechanisms and identify therapeutic targets by applying cell type purification and a combination of bulk and single-cell gene expression profiling to iPSC-derived dopamine neurons from three PD patients carrying *GBA-N370S* mutation. They identified disease-distinguishing molecular etiologies and revealed a temporal ordering of gene expression variation that proposed a role for the transcriptional regulator HDAC4 in upstream regulation of disease progression. They confirmed this finding by the rescue of downstream expression variation and correction of cellular phenotypes previously shown in *GBA-N370S* model PD via the pharmacological modulation of HDAC4 activity or localization, thus paving the way for a pharmacological therapeutic approach to treat PD [152].

Fluorescence-activated cell sorting (FACS) could be used to purify the $MNX1^+$ cells. $MNX1^+$ cells can be sorted out using MNX1:RFP reporter construct or $MNX1^+$ antibody staining. As expected, MNP populations under expansion conditions begin to express MNX1 as I expand them using the expansion medium. Switching to the MN maturation medium further increases the number of MNX1+ MNPs. This phenomenon can also be used as an indicator of reaching the next stage of differentiation. For our optimization experiments, I have generated MNX1:RFP infected WT MNP lines to monitor that a specific point in the differentiation process was reached.

4.2.2. Generated Wild Type and Mutant KU-BVVL iMNs and Express KIF13A

I simultaneously generated four patient-specific iMNs, one being wild type and another being SLC52A3 mutant.

Regardless of the genetic background, *MNX1* and *ChAT* genes were expressed on day 28 KU-BVVL-iMNs. In addition, all differentially expressed marker genes were expressed in KU-BVVL iPSC-derived cell lines throughout the differentiation process (Figure 25). However, expression levels of these genes varied significantly between cell lines. Immunofluorescence staining of neuronal cell fate proteins: Motor neuron and pancreas homeobox 1 (MNX1), class III beta-tubulin (TuJ1) also confirmed this, as the Day 28 cell population consists of neurons

with a considerable amount of MNX1^{+} motor neurons at varying ratios (Figure 26). MNX1:RFP reporter construct that contains Bleomycin resistance gene (Addgene: 37081) could be used for both FACS and antibiotic resistance selection based, purification of MNX1^{+} cells.

KU-BVVL-iMNs can be used as a valid model cell line that reflects the diseased phenotype as immunofluorescence staining of KIF13A protein revealed that KIF13A protein is abundantly present in iMNs. Interestingly, KIF13A was predominantly in the soma and dendritic regions, but not limited to those. In addition, I have observed KIF13A protein presence in the axonal region, indicating KIF13A protein's involvement in somatic and axonal pathways (Figure 27).

CHAPTER 4: DISCUSSION

4.3. Future Directions

In the future work described below, patient-specific iMNs will be used to investigate the interactome KIF13A and possible alterations in the interactome caused by KIF13A "Glu1656Lys" mutation. We aim to pursue the possible effect of the novel KIF13A mutation on MVB formation if we have a hit on the interactome analysis. We aim to conduct RNA-Sequencing on KU-BVVL-iMNs to reveal alterations in the gene expression patterns to reveal possible affected pathways or reveal upregulated cellular mechanisms coping up with the diseased phenotype. RE tubule morphogenesis mechanism, which KIF13A mediated by KIF13A activity explained using the "tug-of-war" model. This model suggests that tubular endosome elongation and fission is a result of "tug-of-war" like activity of opposite-polarity motors, kinesin(s), and dynein(s) [138, 139]. Etoh et al. revealed that kinesin involved in this mechanism is KIF13A and is indispensable for RE tubule morphogenesis, as tubular elongation diminished in KIF13$^{-/-}$ cells [101]. Broken equilibrium in this "tug-of-war" towards one side could affect downstream RE trafficking and could lead to neurodegeneration through deficiency in multiple critical molecular pathways for neuronal survival. We aim to investigate the effect of the novel KIF13A on RE tubule formation dynamics by staining "Microtubule Associated Monooxygenase, Calponin and LIM Domain Containing 1" (MICAL1) and measuring RE tubule length in wild-type and mutant iMNs. Gutiérrez et al.'s study revealing KIF13A involvement in the delivery of AMPA-type glutamate receptors, we aim to use patient-specific iMNs to investigate the role of KIF13A in glutamate receptor distribution and test whether the affected iMNs are more sensitive to glutamate-induced toxicity (Figure 28) [125]. In addition, we have designed and generated various plasmid constructs, including mutant and wild type constructs of KIF13A, KIF13A targeting CRISPR/Cas9 constructs. These molecular reagents along with patient iPSC-derived motor neurons will be important tools to understand KIF13A-related processes and molecular mechanisms that are crucial for a healthy, functioning nervous system. We aim to use the said constructs to generate KIF13A KO iMNs, conduct loss of function and rescue of function experiments to validate and further bolster our findings in the future.

CHAPTER 4: DISCUSSION

4.3.1. Investigation of Differentially Expressed Genes in Wild Type and Mutant iMNs Using RNA-Sequencing

The role of genes in disease development can be investigated at three distinct levels of the central dogma, DNA level, RNA, and protein level. At the DNA level, by studying mutations to determine their effects on a gene, at the RNA level, studying gene expression level and differential splicing of mRNAs, and finally, at the protein level by examining protein folding patterns and interactome.

Developed more than a decade ago, RNA sequencing (RNA-seq) has become an indispensable tool for transcriptome-wide analysis of differential gene expression. The prominent advantage of RNA-seq is that it enables the sequencing of new transcriptome without prior information and is massively high-throughoutput. RNA-seq enables statistical modeling of significant changes in the expression levels of individual genes and/or transcripts between sample groups [210].

RNA-seq can be used to characterize whole transcriptome modifications occurring in disease provide snapshots of transcriptomic events characterizing the disease. Rna-seq provides insight into disease development with statistical modeling of significant changes in the expression levels of individual genes. Up-regulated and/or down-regulated genes can be used to identify compromised molecular processes resulting from a genomic alteration, thus, reveal novel mechanisms and targets [152, 199, 210-218].

We aim to conduct RNA-Sequencing on KU-BVVL-iMNs to reveal alterations in the gene expression patterns to reveal possible affected pathways or reveal upregulated cellular mechanisms coping up with the diseased phenotype.

CHAPTER 4: DISCUSSION

4.3.2. Biotinylation Based Investigation of KIF13A Interactome

Finding physiologically relevant protein interactions is crucial for understanding the mechanistic properties of the proteins of interest. Different methods have been developed to detect protein-protein interactions, such as co-immunoprecipitation (co-IP) to detect direct interactions, yeast two-hybrid to investigate in vivo binding of two proteins, and Proximity-dependent biotinylation methods to identify weak and/or transient interactions [219].

Biotinylation is the cellular process of covalent attaching biotin to a protein, nucleic acid, or other molecules. Biotinylation rarely occurs in the cells compared to acetylation, methylation, or ubiquitination in nature. Therefore, exogeneous biotinylation can be detected via mass-spectrometry analysis, and specific proteins can be determined via comparison with the control background. Biotinylation is a rapid, specific process. Due to the small size of biotin, biotinylation is unlikely to disturb the natural function of a molecule. Thus, Proximity-dependent biotinylation methods enable the screening for physiologically relevant protein interactions that occur in living cells and prove to be a valuable tool for the identification of weak and/or transient interactions.

Proximity-dependent biotinylation approaches involve the fusion of a protein of interest with a biotinylation enzyme. Biotin protein ligase and APEX peroxidase are distinctly used enzymes in Proximity-dependent biotinylation approaches, used in BioID and APEX techniques, respectively [219-223].

BioID is a technique that harnesses modified, promiscuous biotin ligase to biotinylate proteins based on proximity, Proteins identified by BioID are candidate interactors for the protein of interest. Taking advantage of the nature of the biotinylation process BioID can be applied to insoluble proteins, can identify weak and/or transient interactions, and is amenable to temporal regulation [220].

Considering our protein of interest, KIF13A is a kinesin-like motor protein involved in molecular cargo transport and modulation of recycling endosomes, finding physiologically relevant

protein interactions, more importantly, the discovery of an alteration in the mutant KIF13A interactome is crucial for understanding the mechanistic properties of the protein of our interest and other interaction partners. The Discovery of additional interaction partner(s) and KIF13A dependent molecular processes could further improve knowledge on neurodegeneration and possible therapeutic targets and pave the road for potential therapeutic applications.

In future experiments, we aim to investigate the interactome KIF13A and possible alterations in the interactome caused by KIF13A "Glu1656Lys" mutation. For this purpose, we have designed and generated lentiviral BioID fusion constructs of wild-type and mutant KIF13A protein. Newly generated, sequence validated KIF13A-BioID constructs tested for function using western blot. Exogenous biotinylation was detected in 293T Cells transfected with lentiviral KIF13A-BioID constructs and cultured in a medium supplemented with biotin, proving KIF13A-BioID constructs are functional (App. Figure 9). We aim to generate stable wild-type, KIF13A mutant, and *KIF13A*$^{-/-}$ iPSCs expressing wild-type and mutant KIF13A-BioID fusion constructs. KIF13A protein functions as weak dimers. Results originating from the wild-type and mutant KIF13A dimers could obscure the actual alterations in the interactome and be misleading. Thus, we aim to generate these cell lines that express KIF13A-BioID corresponding to their genetic background and conduct BioID assay on the iMN progeny (Figure 28, Table 23).

Cell Line	Genetic Background	Expressing
KU-BVVL-WT-BioID	Wild Type	WT KIF13A-BioID
KU-BVVL-MT-BioID	KIF13A Glu1656Lys Mutant	MT KIF13A-BioID
KU-BVVL-WT-BioID-CT	*KIF13A*$^{-/-}$	WT KIF13A-BioID
KU-BVVL-MT-BioID-CT	*KIF13A*$^{-/-}$	MT KIF13A-BioID

Table 23: Proposed iPSC lines for the KIF13A BioID assay. Cell lines that express KIF13A-BioID correspond to their genetic background. BioID assay will be conducted on the iMN progeny.

CHAPTER 4: DISCUSSION

4.3.3. Investigation of the Role KIF13A in Glutamate Receptor Distribution and Sensitivity to Glutamate Induced Excitotoxicity

Glutamate is the most abundant free amino acid in the brain and is the major excitatory neurotransmitter in the brain. Glutamate binds and activates both ligand-gated ion channels (ionotropic glutamate receptors) and a class of G-protein coupled receptors (metabotropic glutamate receptors) [224, 225].

The toxic actions of excitatory neurotransmitters, primarily glutamate, may lead to a phenomenon referred to as excitotoxicity, where the exacerbated or prolonged activation of glutamate receptors starts a cascade of neurotoxicity that ultimately leads to the loss of neuronal function and cell death. Both acute and chronic causes have been shown to lead to glutamate-induced excitotoxicity. Acute excitotoxicity refers to insults like ischemic stroke via the overactivation of ionotropic glutamate receptors. Chronic excitotoxicity refers to the type of excitotoxicity observed in neurodegenerative diseases, including amyotrophic lateral sclerosis, Alzheimer's disease, and Huntington's disease. Based on these findings, Efforts to develop neuroprotective strategies and drugs have commenced that either inhibit glutamate receptors or decrease extracellular glutamate. Expanding the knowledge on molecular processes that could sensitize the cells to glutamate-induced excitotoxicity could help these efforts [224-229].

In 2018 Shi et al. showed that haploinsufficiency leads to neurodegeneration in C9ORF72 ALS/FTD human induced motor neurons. Their results indicate that haploinsufficiency for C9ORF72 activity triggers neurodegeneration in C9ORF72 ALS through reduced C9ORF72 activity causing the accumulation of both AMPA and NMDA glutamate receptors and excitotoxicity in response to glutamate caused by lysosomal maturation deficit. They proposed that reduced C9ORF72 levels lead to fewer lysosomes in motor neurons in vitro and in vivo, and this may be a result of, in part, altered trafficking of M6PR+ vesicles [150]. Although KIF13A was only shown to transfer mannose-6-phosphate receptors (M6PR) to the cell surface in T cells, this finding could also indicate the possibility of KIF13A dependent transport of M6PR, essential for lysosome biogenesis [137].

CHAPTER 4: DISCUSSION

In 2021 Gutiérrez et al. found that KIF13A is specifically required for the delivery of AMPARs to the spine surface during LTP induction and KIF13A depletion from hippocampal slices abolishes LTP expression [125]. Even in a contradicting manner, KIF13A is known to be mediating the transport of at least one type of glutamate receptor, AMPA.

Considering these findings, we suspect that mutations in KIF13A could affect glutamate receptor distribution in cells. Ultimately leading to neurodegeneration through sensitization of neurons to glutamate-induced excitotoxicity.

To test whether *KIF13A* mutation affects glutamate receptor distribution and sensitivity to glutamate-induced excitotoxicity, we aim to conduct immunofluorescence staining of AMPA and NMDA glutamate receptors to test if there is a significant alteration in AMPA and/or NMDA receptor distribution in KIF13A mutant iMNs compared to wild type iMNs (Figure 28). In addition, we designed an experimental plan on which we exclude neurotrophic factors from MN maturation medium 7 Days prior to initiation of short-term, high dosed (100 µM) glutamate-induced toxicity (Figure 28). Our attempts to initiate glutamate-induced excitotoxicity iMN failed during initial optimization experiments, as we failed to observe significant cell death in high-dose glutamate treated cells. We suspect we failed to observe significant cell death because either cell culture environment was too supporting, considering the presence of glial cells and medium composition or high dose glutamate treatment period. We aim to optimize glutamate concentration and treatment time on primary rodent neuronal cultures before conducting another glutamate-induced excitotoxicity experiment series with iMN.

CHAPTER 4: DISCUSSION

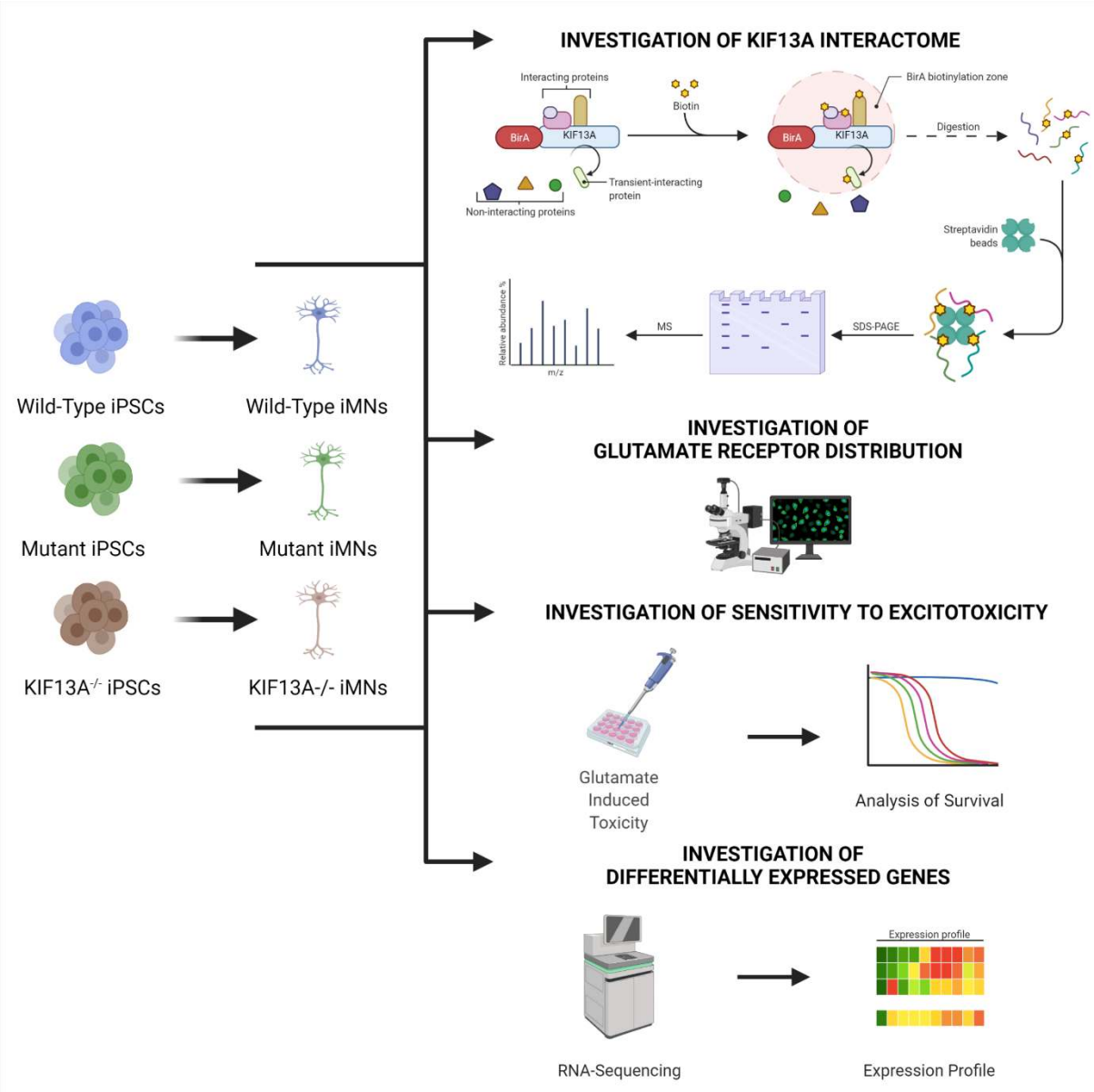

Figure 28: Representation of future directions in this project. Wild type iMNS will serve as control. Wild type and mutant KU-BVVL-iMNs will be used in biotinylation based investigation of KIF13A interactome, investigation of the role KIF13A in glutamate receptor distribution and sensitivity to glutamate Induced excitotoxicity, and investigation of differentially expressed genes in wild type and mutant iMNs via RNA-Sequencing.

CHAPTER 5: CONCLUSION

In this study, I have generated and characterized patient-specific induced pluripotent stem cells (iPSCs) of KU-BVVL patients carrying neurodegeneration, causing novel KIF13A mutation. In addition, I have generated and characterized patient-specific induced motor neurons (iMNS) of KU-BVVL patients carrying the KIF13A mutation via a small-molecule-based differentiation method which I have adapted from previous studies and optimized to suit our experimental requirements. KU-BVVL-iMNs can be used as a valid model cell line that reflects the diseased phenotype as KIF13A protein is abundantly present in iMNs, predominantly in the soma and dendritic regions, but not limited to those. Furthermore, I have also designed and generated various plasmid constructs, including mutant and wild type constructs of KIF13A, KIF13A targeting CRISPR/Cas9 constructs, and KIF13A-BioID fusion constructs. These molecular reagents, along with patient iPSC-derived motor neurons, will be important tools to understand KIF13A related processes and molecular mechanisms that are crucial for a healthy, functioning nervous system. As the future direction, we aim to use wild-type and mutant KIF13A-BioID constructs and conduct a screen for physiologically relevant protein interaction alterations that occur in the mutant iMNs. In addition, we aim to investigate the role of KIF13A in glutamate receptor distribution and conduct glutamate-induced toxicity assays to test whether mutant iMNs are more susceptible to glutamate toxicity, as in the case of C9ORF72-ALS and conduct RNA-Sequencing on KU-BVVL-iMNs to reveal alterations in the gene expression patterns to reveal possible affected pathways or reveal upregulated cellular mechanisms coping up with the diseased phenotype.

CHAPTER 6: APPENDIX

6.1. MN Differentiation Optimization Experiment Results

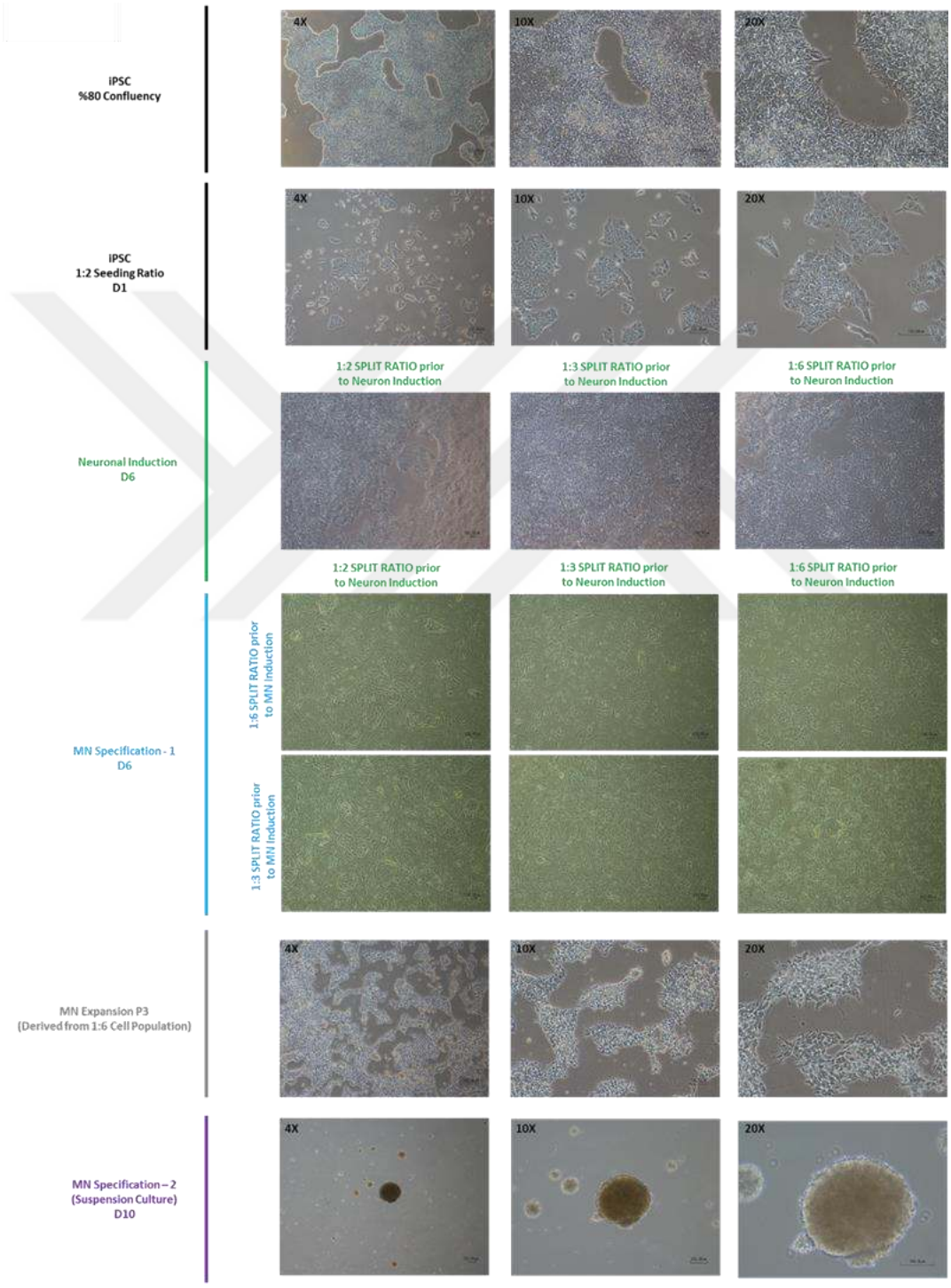

Appendix Figure 1: Bright-field and fluorescent microscopy images of WT KU-BVVL iPSC line from iPSC culture stage to the MN maturation stage of the differentiation procedure. (Scale Bar: 100µm).

CHAPTER 6: APPENDIX

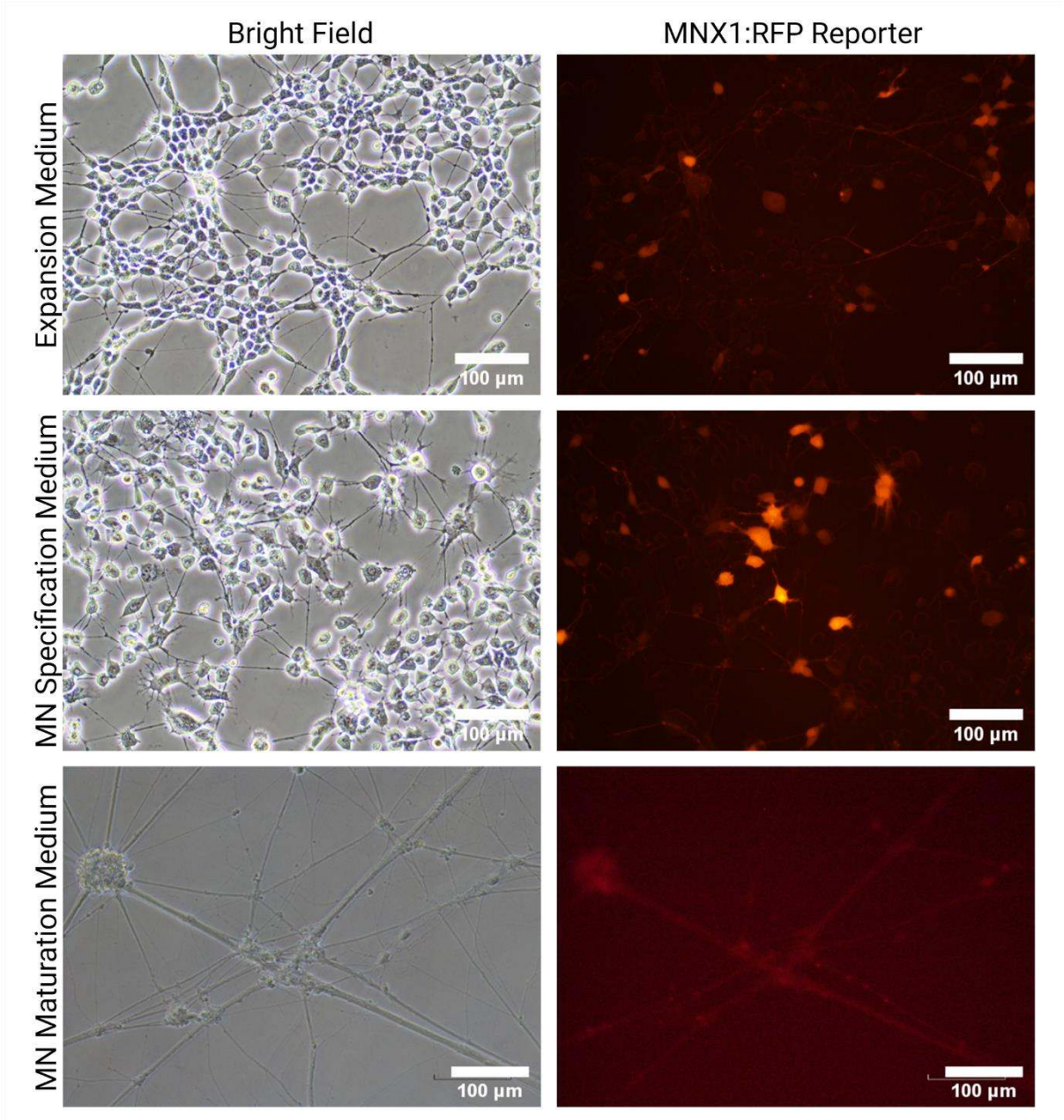

Appendix Figure 2: Bright field and fluorescence microscopy images of WT KU-BVVL-MNP transduced with lentiviral MNX1:RFP Reporter construct. MNP populations under expansion condition begin to express MNX1 as we expand them using expansion medium. Switching to maturation medium further increase the number of MNX1+ MNPs (Scale Bar: 100µm).

CHAPTER 6: APPENDIX

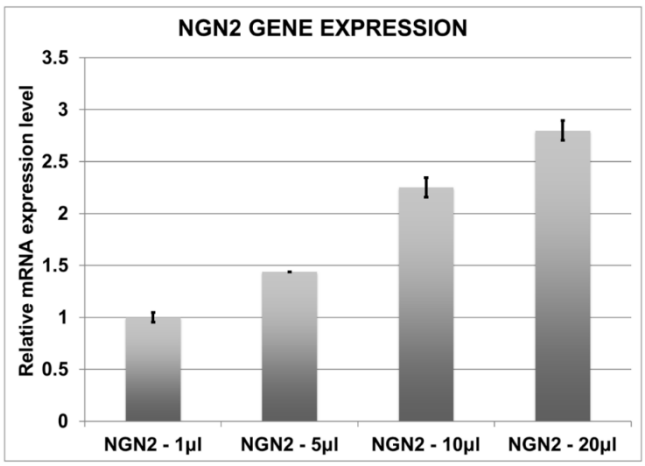

Appendix Figure 3: Functional analysis of concentrated NGN2 Virus. RT-qPCR results of 293T underwent transduction and dox treatment (n=3).

CHAPTER 6: APPENDIX

6.2. *KIF13A* and Riboflavin Transporter (*RFVT/SLC52*) RT-qPCR Conducted on Select Cell Lines

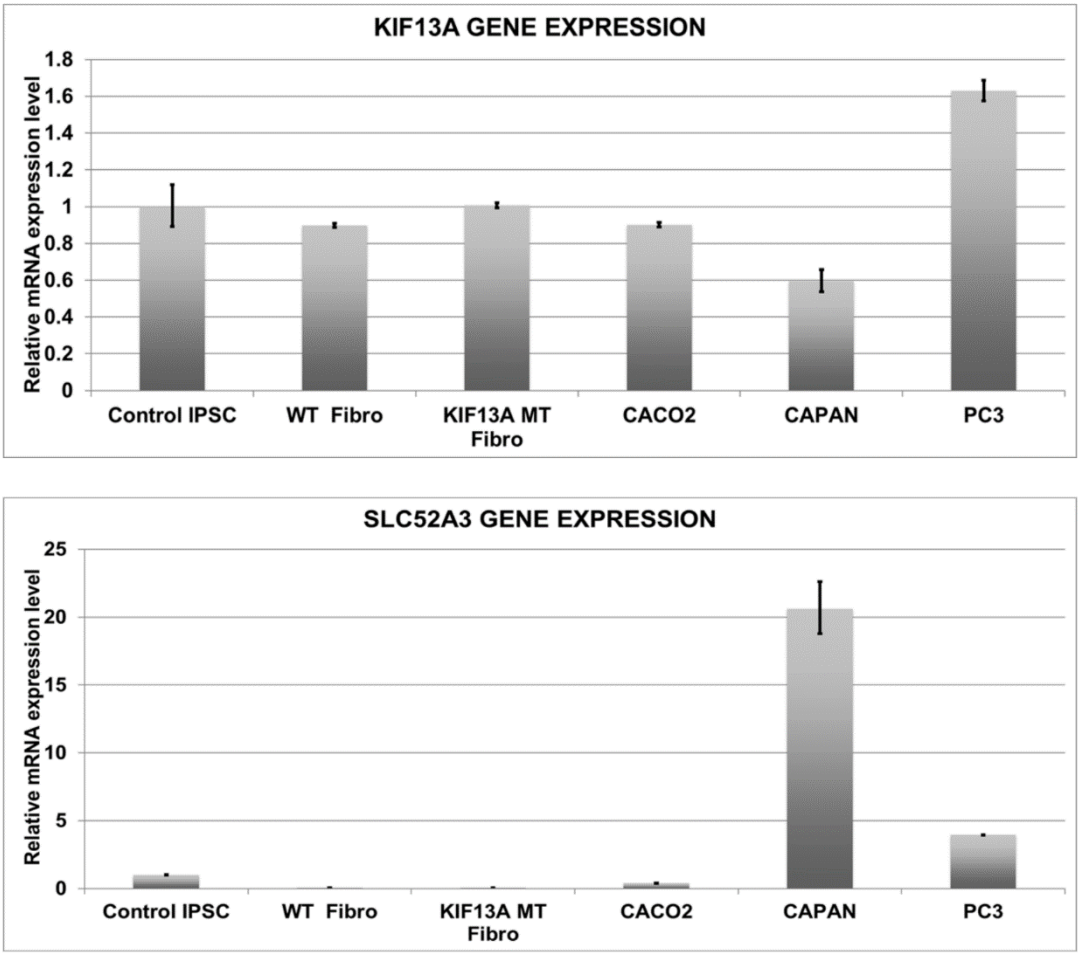

Appendix Figure 4: KIF13A and Riboflavin Transporter (RFVT/SLC52) RT-qPCR Conducted on Select Cell Lines. Relative mRNA expression level was normalized to CAPAN cell line. SLC52A2 expression was not detected in select cell lines thus, was not included in the figure.

CHAPTER 6: APPENDIX

6.3. Designed & Generated Plasmid Constructs

#	Construct	Source	Tag	Cloning Method
1	**$_{MT}$KIF13A-GFP**	Addgene: 90199 - Modified	-	Q5-SDM
2	pLenti-CRISPRv2 KIF13A-E1	Addgene: 52961 - Modified	-	REC
3	pLenti-CRISPRv2 KIF13A-E2	Addgene: 52961 - Modified	-	REC
4	pLenti-CRISPRv2 KIF13A-E4	Addgene: 52961 - Modified	-	REC
5	pLenti-CRISPRv2 KIF13A-E11	Addgene: 52961 - Modified	-	REC
6	**$_{WT}$KIF13A-BioID**	Addgene: 90199 / Addgene: 36047	HA Tag	REC
7	**$_{MT}$KIF13A-BioID**	$_{MT}$KIF13A-GFP / Addgene: 36047	HA Tag	REC
8	**BioID-$_{WT}$KIF13A**	Addgene: 90199 / Addgene:35700	HA Tag	Q5-SDM/REC
9	**BioID-$_{MT}$KIF13A**	$_{MT}$KIF13A-GFP / Addgene: 35700	HA Tag	Q5-SDM/REC
10	**$_{WT}$KIF13A-miniTurbo**	Addgene: 90199 / Addgene: 124647	FLAG Tag	REC
11	**$_{MT}$KIF13A-miniTurbo**	$_{MT}$KIF13A-GFP / Addgene: 124647	FLAG Tag	REC
12	**miniTurbo-$_{WT}$KIF13A**	Addgene: 90199 / Addgene: 124647	FLAG Tag	REC
13	**miniTurbo-$_{MT}$KIF13A**	$_{MT}$KIF13A-GFP / Addgene: 124647	FLAG Tag	REC
14	**mCherry-SLC52A2**	Addgene: 54563 / Addgene: 161068	HA Tag	REC
15	**SLC52A2-mCherry**	Addgene: 161068 / Addgene: 54517	HA Tag	REC
16	**mCerulean-SLC52A2**	Addgene: 54605 / Addgene: 161068	HA Tag	REC
17	**SLC52A2-mCerulean**	Addgene: 161068 / Addgene: 54730	HA Tag	REC
18	**mCherry-SLC52A3**	Addgene: 54563 / Addgene: 161347	HA Tag	REC
19	**SLC52A3-mCherry**	Addgene: 161347 / Addgene: 54517	HA Tag	REC
20	**mCherry-Rab11A-HA Tag**	Addgene: 54563 / Addgene: 55390	HA Tag	REC
21	**PENTR1A – HinDIII in MCS**	Addgene: 17398 - Modified	-	Q5-SDM

Table 24: The list of designed and generated plasmid constructs in this study. For fusion constructs the first cited plasmid refers to the backbone, the second cited plasmid refers to the insert. **(**Q5-SDM: Q5-Site-Directed Mutagenesis. REC: Restriction Enzyme Cloning).

CHAPTER 6: APPENDIX

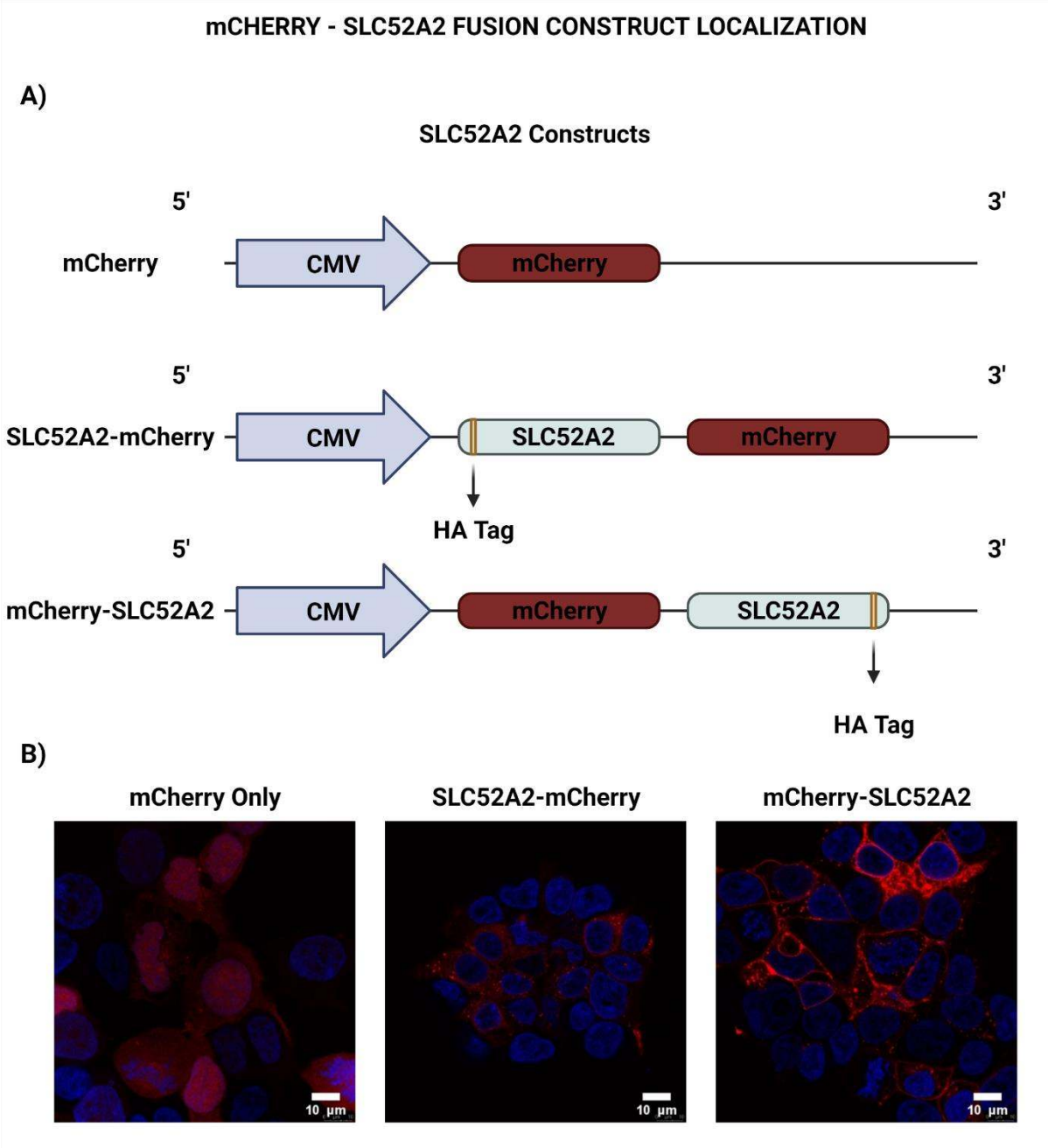

Appendix Figure 5: mCherry-SLC52A2 Fusion Construct Localization Experiment. **A)** mCherry, SLC52A2-mCherry, and mCherry-SLC52A2 partial cDNA maps. **B)** Confocal microscopy images of HEK 293T cells transfected with mCherry, SLC52A2-mCherry, and mCherry-SLC52A2 plasmids (Scale Bar: 10 µm).

CHAPTER 6: APPENDIX

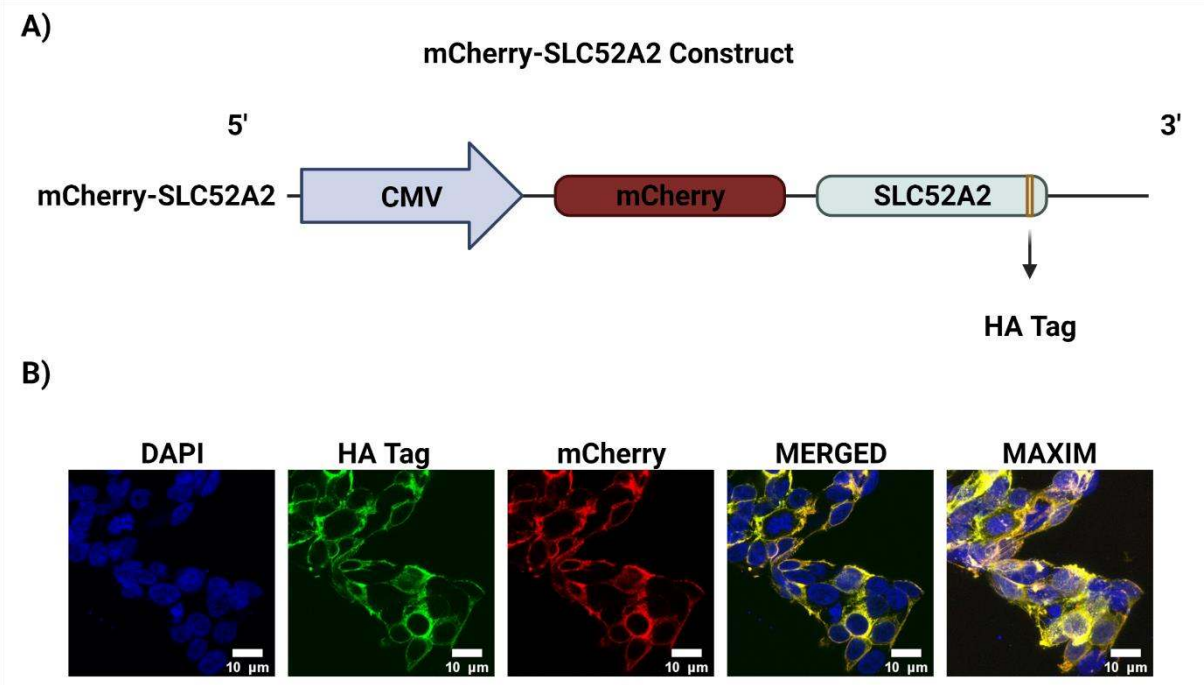

Appendix Figure 6: mCherry-SLC52A2 Fusion Construct Localization Experiment. **A)** mCherry-SLC52A2 partial cDNA map. **B)** Confocal microscopy images of HEK 293T cells transfected with mCherry-SLC52A2 plasmid. SLC52A2 was stained with anti-HA-Tag antibody. (Scale Bar: 10 µm).

CHAPTER 6: APPENDIX

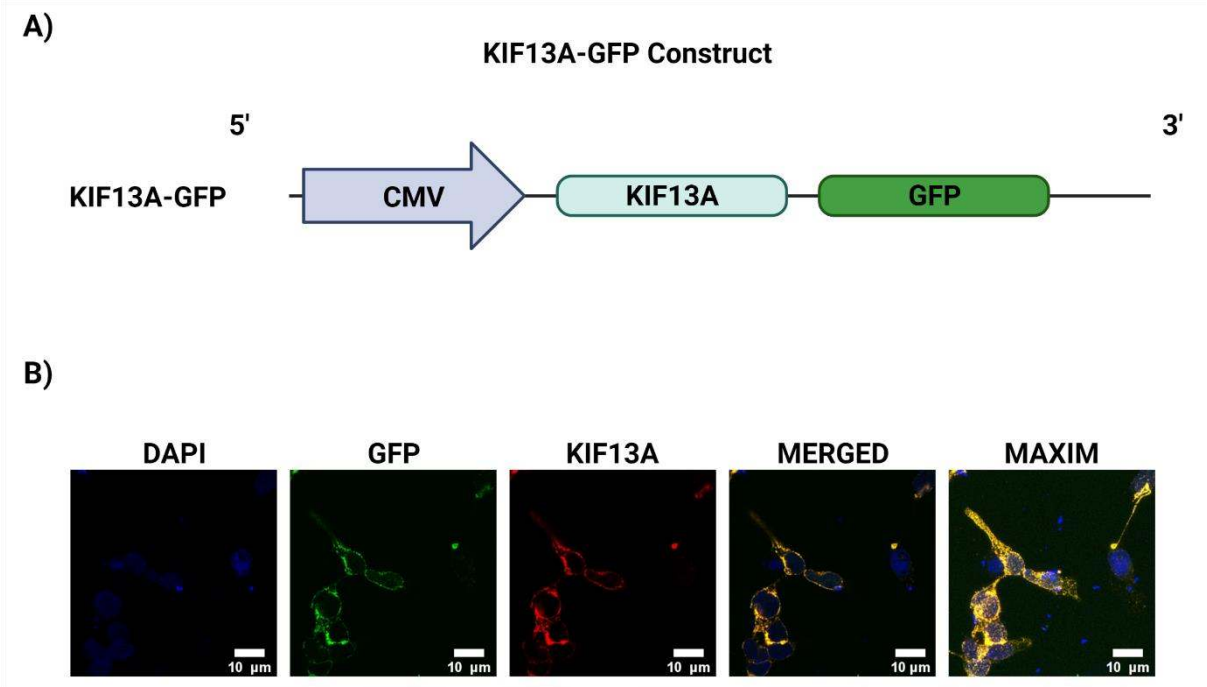

Appendix Figure 7: KIF13A-GFP Fusion Construct Localization Experiment. **A)** KIF13A-GFP partial cDNA map. **B)** Confocal microscopy images of HEK 293T cells transfected KIF13A-GFP plasmid. KIF13A was stained with anti-KIF13A antibody. (Scale Bar: 10 µm).

CHAPTER 6: APPENDIX

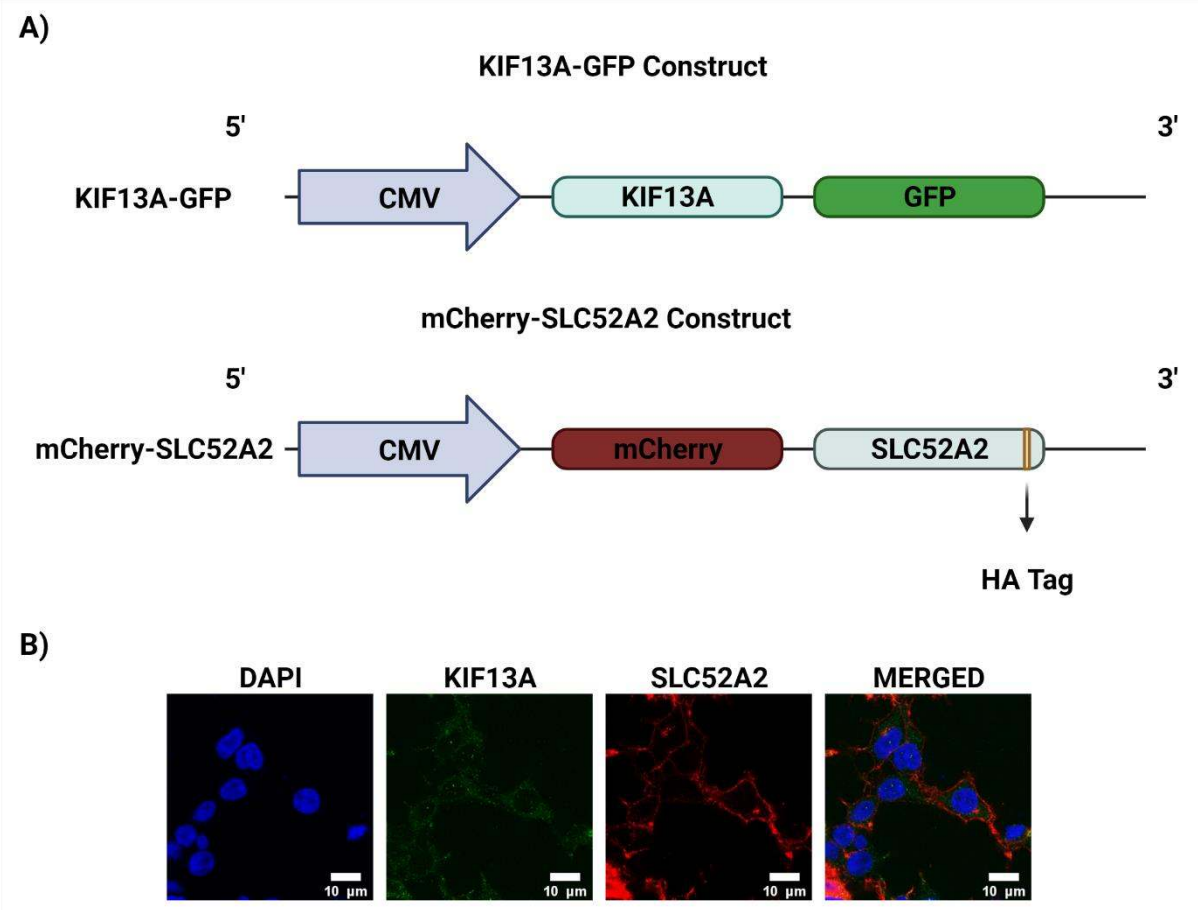

Appendix Figure 8: KIF13A and SLC52A2 Fusion Construct Colocalization Experiment. **A)** KIF13A-GFP and mCherry-SLC52A2 partial cDNA maps. **B)** Confocal microscopy images of HEK 293T cells transfected KIF13A-GFP and mCherry-SLC52A2 plasmids. KIF13A was stained with anti-KIF13A antibody to further enhance GFP signal. (Scale Bar: 10 µm).

CHAPTER 6: APPENDIX

Biotin-HRP Western Blot to Test the Functionality of BioID Constructs

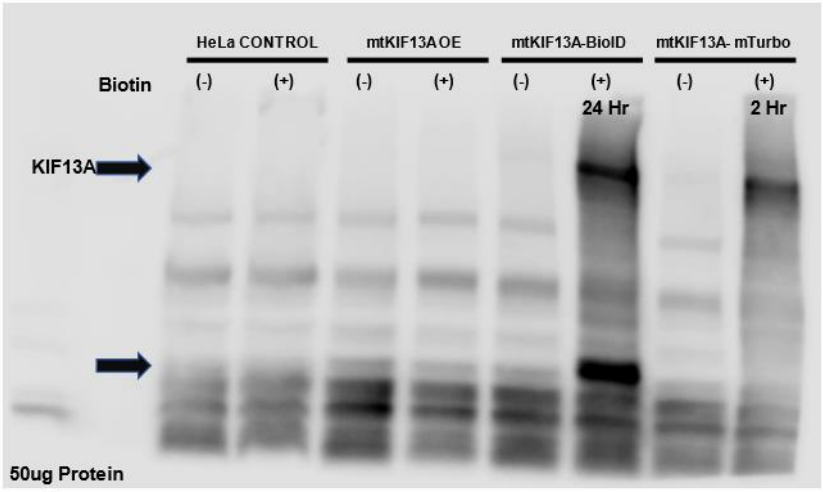

Appendix Figure 9: Biotin-HRP western blot following transfection and biotin treatment. (Protein Concentration: 50µg overexpression whole cell lysate samples were loaded.)

CHAPTER 6: APPENDIX

6.4. Generation of KIF13A K/O Cell Lines

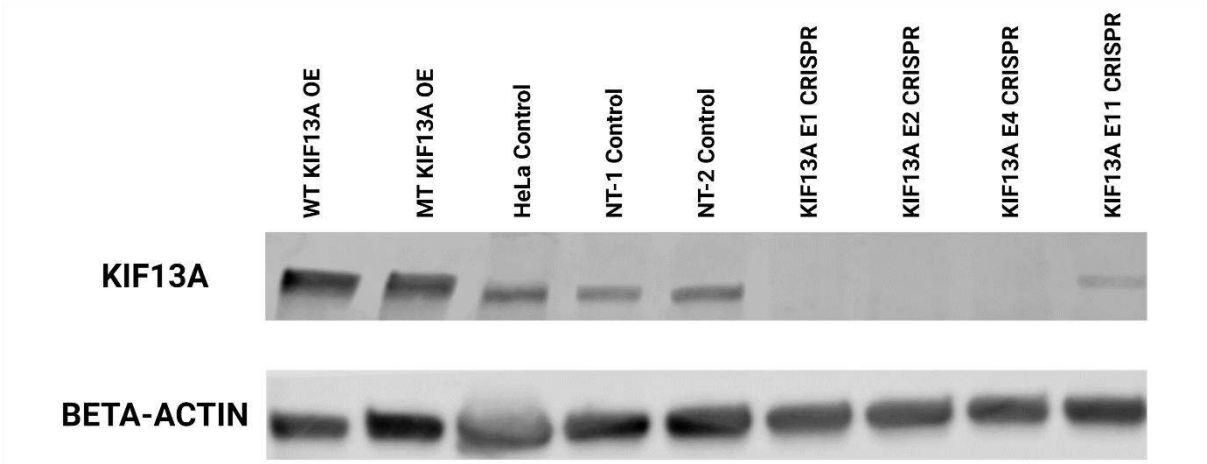

Appendix Figure 10: KIF13A western blot following transduction and puromycin selection. Characterization of KIF13A KO Cell Lines. (Protein Concentrations: 50µg overexpression whole cell lysate samples were loaded, for the rest 100µg whole cell lysate samples were loaded.)

REFERENCES

REFERENCES

1. Gan, L., et al., *Converging pathways in neurodegeneration, from genetics to mechanisms.* Nat Neurosci, 2018. **21**(10): p. 1300-1309.

2. Nollen, E.A., et al., *Genome-wide RNA interference screen identifies previously undescribed regulators of polyglutamine aggregation.* Proc Natl Acad Sci U S A, 2004. **101**(17): p. 6403-8.

3. Spiess, C., et al., *Mechanism of the eukaryotic chaperonin: protein folding in the chamber of secrets.* Trends Cell Biol, 2004. **14**(11): p. 598-604.

4. Settembre, C., et al., *Signals from the lysosome: a control centre for cellular clearance and energy metabolism.* Nat Rev Mol Cell Biol, 2013. **14**(5): p. 283-96.

5. Sontag, E.M., et al., *Exogenous delivery of chaperonin subunit fragment ApiCCT1 modulates mutant Huntingtin cellular phenotypes.* Proc Natl Acad Sci U S A, 2013. **110**(8): p. 3077-82.

6. Lindberg, I., et al., *Chaperones in Neurodegeneration.* J Neurosci, 2015. **35**(41): p. 13853-9.

7. Noormohammadi, A., et al., *Somatic increase of CCT8 mimics proteostasis of human pluripotent stem cells and extends C. elegans lifespan.* Nat Commun, 2016. **7**: p. 13649.

8. Shorter, J., *Engineering therapeutic protein disaggregases.* Mol Biol Cell, 2016. **27**(10): p. 1556-60.

9. Gomez-Pastor, R., et al., *Abnormal degradation of the neuronal stress-protective transcription factor HSF1 in Huntington's disease.* Nat Commun, 2017. **8**: p. 14405.

REFERENCES

10. Lackie, R.E., et al., *The Hsp70/Hsp90 Chaperone Machinery in Neurodegenerative Diseases.* Front Neurosci, 2017. **11**: p. 254.

11. Kim, G.H., et al., *The Role of Oxidative Stress in Neurodegenerative Diseases.* Exp Neurobiol, 2015. **24**(4): p. 325-40.

12. Beal, M.F., et al., *Neurochemical and histologic characterization of striatal excitotoxic lesions produced by the mitochondrial toxin 3-nitropropionic acid.* J Neurosci, 1993. **13**(10): p. 4181-92.

13. Cui, L., et al., *Transcriptional repression of PGC-1alpha by mutant huntingtin leads to mitochondrial dysfunction and neurodegeneration.* Cell, 2006. **127**(1): p. 59-69.

14. Weydt, P., et al., *Thermoregulatory and metabolic defects in Huntington's disease transgenic mice implicate PGC-1alpha in Huntington's disease neurodegeneration.* Cell Metab, 2006. **4**(5): p. 349-62.

15. Cuervo, A.M., *Autophagy and aging: keeping that old broom working.* Trends Genet, 2008. **24**(12): p. 604-12.

16. Batlevi, Y. and A.R. La Spada, *Mitochondrial autophagy in neural function, neurodegenerative disease, neuron cell death, and aging.* Neurobiol Dis, 2011. **43**(1): p. 46-51.

17. Shin, J.H., et al., *PARIS (ZNF746) repression of PGC-1alpha contributes to neurodegeneration in Parkinson's disease.* Cell, 2011. **144**(5): p. 689-702.

18. Sugiura, A., et al., *A new pathway for mitochondrial quality control: mitochondrial-derived vesicles.* EMBO J, 2014. **33**(19): p. 2142-56.

19. Burte, F., et al., *Disturbed mitochondrial dynamics and neurodegenerative disorders.* Nat Rev Neurol, 2015. **11**(1): p. 11-24.

REFERENCES

20. Dickey, A.S., et al., *PPAR-delta is repressed in Huntington's disease, is required for normal neuronal function and can be targeted therapeutically.* Nat Med, 2016. **22**(1): p. 37-45.

21. Burbulla, L.F., et al., *Dopamine oxidation mediates mitochondrial and lysosomal dysfunction in Parkinson's disease.* Science, 2017. **357**(6357): p. 1255-1261.

22. Golpich, M., et al., *Mitochondrial Dysfunction and Biogenesis in Neurodegenerative diseases: Pathogenesis and Treatment.* CNS Neurosci Ther, 2017. **23**(1): p. 5-22.

23. Sorrentino, V., et al., *Enhancing mitochondrial proteostasis reduces amyloid-beta proteotoxicity.* Nature, 2017. **552**(7684): p. 187-193.

24. Hara, T., et al., *Suppression of basal autophagy in neural cells causes neurodegenerative disease in mice.* Nature, 2006. **441**(7095): p. 885-9.

25. Komatsu, M., et al., *Essential role for autophagy protein Atg7 in the maintenance of axonal homeostasis and the prevention of axonal degeneration.* Proc Natl Acad Sci U S A, 2007. **104**(36): p. 14489-94.

26. Buchan, J.R., et al., *Eukaryotic stress granules are cleared by autophagy and Cdc48/VCP function.* Cell, 2013. **153**(7): p. 1461-74.

27. Cortes, C.J., et al., *Polyglutamine-expanded androgen receptor interferes with TFEB to elicit autophagy defects in SBMA.* Nat Neurosci, 2014. **17**(9): p. 1180-9.

28. Ochaba, J., et al., *Potential function for the Huntingtin protein as a scaffold for selective autophagy.* Proc Natl Acad Sci U S A, 2014. **111**(47): p. 16889-94.

29. Seguin, S.J., et al., *Inhibition of autophagy, lysosome and VCP function impairs stress granule assembly.* Cell Death Differ, 2014. **21**(12): p. 1838-51.

30. Abeliovich, A. and A.D. Gitler, *Defects in trafficking bridge Parkinson's disease pathology and genetics.* Nature, 2016. **539**(7628): p. 207-216.

REFERENCES

31. Taylor, J.P., R.H. Brown, Jr., and D.W. Cleveland, *Decoding ALS: from genes to mechanism.* Nature, 2016. **539**(7628): p. 197-206.

32. Ashkenazi, A., et al., *Polyglutamine tracts regulate beclin 1-dependent autophagy.* Nature, 2017. **545**(7652): p. 108-111.

33. Menzies, F.M., et al., *Autophagy and Neurodegeneration: Pathogenic Mechanisms and Therapeutic Opportunities.* Neuron, 2017. **93**(5): p. 1015-1034.

34. Oakes, J.A., M.C. Davies, and M.O. Collins, *TBK1: a new player in ALS linking autophagy and neuroinflammation.* Mol Brain, 2017. **10**(1): p. 5.

35. Wang, C., et al., *Endo-lysosomal dysfunction: a converging mechanism in neurodegenerative diseases.* Curr Opin Neurobiol, 2018. **48**: p. 52-58.

36. Hernandez, A.R. and E.T. Kool, *The components of xRNA: synthesis and fluorescence of a full genetic set of size-expanded ribonucleosides.* Org Lett, 2011. **13**(4): p. 676-9.

37. O'Rourke, J.G., et al., *C9orf72 is required for proper macrophage and microglial function in mice.* Science, 2016. **351**(6279): p. 1324-9.

38. Kamelgarn, M., et al., *ALS mutations of FUS suppress protein translation and disrupt the regulation of nonsense-mediated decay.* Proc Natl Acad Sci U S A, 2018. **115**(51): p. E11904-E11913.

39. Chen, H.J., et al., *RRM adjacent TARDBP mutations disrupt RNA binding and enhance TDP-43 proteinopathy.* Brain, 2019. **142**(12): p. 3753-3770.

40. Gunawardena, S. and L.S. Goldstein, *Disruption of axonal transport and neuronal viability by amyloid precursor protein mutations in Drosophila.* Neuron, 2001. **32**(3): p. 389-401.

41. Duncan, J.E. and L.S. Goldstein, *The genetics of axonal transport and axonal transport disorders.* PLoS Genet, 2006. **2**(9): p. e124.

REFERENCES

42. Morfini, G.A., et al., *Axonal transport defects in neurodegenerative diseases.* J Neurosci, 2009. **29**(41): p. 12776-86.

43. Lloyd, T.E., *Axonal transport disruption in peripheral nerve disease: From Jack's discoveries as a resident to recent contributions.* J Peripher Nerv Syst, 2012. **17 Suppl 3**: p. 46-51.

44. Anderson, E.N., J.A. White, and S. Gunawardena, *Axonal transport and neurodegenerative disease: vesicle-motor complex formation and their regulation.* Degener Neurol Neuromuscul Dis, 2014. **4**: p. 29-47.

45. Sleigh, J.N., et al., *Axonal transport and neurological disease.* Nat Rev Neurol, 2019. **15**(12): p. 691-703.

46. Vitet, H., V. Brandt, and F. Saudou, *Traffic signaling: new functions of huntingtin and axonal transport in neurological disease.* Curr Opin Neurobiol, 2020. **63**: p. 122-130.

47. Zuccato, C. and E. Cattaneo, *Brain-derived neurotrophic factor in neurodegenerative diseases.* Nat Rev Neurol, 2009. **5**(6): p. 311-22.

48. Parkhurst, C.N., et al., *Microglia promote learning-dependent synapse formation through brain-derived neurotrophic factor.* Cell, 2013. **155**(7): p. 1596-609.

49. Eyileten, C., et al., *The Relation of the Brain-Derived Neurotrophic Factor with MicroRNAs in Neurodegenerative Diseases and Ischemic Stroke.* Mol Neurobiol, 2021. **58**(1): p. 329-347.

50. Ruiz-Gonzalez, D., et al., *Effects of physical exercise on plasma brain-derived neurotrophic factor in neurodegenerative disorders: A systematic review and meta-analysis of randomized controlled trials.* Neurosci Biobehav Rev, 2021. **128**: p. 394-405.

51. Johnson, J.O., et al., *Exome sequencing reveals VCP mutations as a cause of familial ALS.* Neuron, 2010. **68**(5): p. 857-64.

REFERENCES

52. Liu-Yesucevitz, L., et al., *Tar DNA binding protein-43 (TDP-43) associates with stress granules: analysis of cultured cells and pathological brain tissue.* PLoS One, 2010. **5**(10): p. e13250.

53. Vanderweyde, T., et al., *Contrasting pathology of the stress granule proteins TIA-1 and G3BP in tauopathies.* J Neurosci, 2012. **32**(24): p. 8270-83.

54. Cirulli, E.T., et al., *Exome sequencing in amyotrophic lateral sclerosis identifies risk genes and pathways.* Science, 2015. **347**(6229): p. 1436-41.

55. Patel, A., et al., *A Liquid-to-Solid Phase Transition of the ALS Protein FUS Accelerated by Disease Mutation.* Cell, 2015. **162**(5): p. 1066-77.

56. Lee, K.H., et al., *C9orf72 Dipeptide Repeats Impair the Assembly, Dynamics, and Function of Membrane-Less Organelles.* Cell, 2016. **167**(3): p. 774-788 e17.

57. Lin, Y., et al., *Toxic PR Poly-Dipeptides Encoded by the C9orf72 Repeat Expansion Target LC Domain Polymers.* Cell, 2016. **167**(3): p. 789-802 e12.

58. Vanderweyde, T., et al., *Interaction of tau with the RNA-Binding Protein TIA1 Regulates tau Pathophysiology and Toxicity.* Cell Rep, 2016. **15**(7): p. 1455-1466.

59. Boeynaems, S., et al., *Phase Separation of C9orf72 Dipeptide Repeats Perturbs Stress Granule Dynamics.* Mol Cell, 2017. **65**(6): p. 1044-1055 e5.

60. Gopal, P.P., et al., *Amyotrophic lateral sclerosis-linked mutations increase the viscosity of liquid-like TDP-43 RNP granules in neurons.* Proc Natl Acad Sci U S A, 2017. **114**(12): p. E2466-E2475.

61. Mackenzie, I.R., et al., *TIA1 Mutations in Amyotrophic Lateral Sclerosis and Frontotemporal Dementia Promote Phase Separation and Alter Stress Granule Dynamics.* Neuron, 2017. **95**(4): p. 808-816 e9.

REFERENCES

62. Apicco, D.J., et al., *Reducing the RNA binding protein TIA1 protects against tau-mediated neurodegeneration in vivo.* Nat Neurosci, 2018. **21**(1): p. 72-80.

63. Yin, F., et al., *Exaggerated inflammation, impaired host defense, and neuropathology in progranulin-deficient mice.* J Exp Med, 2010. **207**(1): p. 117-28.

64. Cribbs, D.H., et al., *Extensive innate immune gene activation accompanies brain aging, increasing vulnerability to cognitive decline and neurodegeneration: a microarray study.* J Neuroinflammation, 2012. **9**: p. 179.

65. Griciuc, A., et al., *Alzheimer's disease risk gene CD33 inhibits microglial uptake of amyloid beta.* Neuron, 2013. **78**(4): p. 631-43.

66. Crotti, A., et al., *Mutant Huntingtin promotes autonomous microglia activation via myeloid lineage-determining factors.* Nat Neurosci, 2014. **17**(4): p. 513-21.

67. Cho, S.H., et al., *SIRT1 deficiency in microglia contributes to cognitive decline in aging and neurodegeneration via epigenetic regulation of IL-1beta.* J Neurosci, 2015. **35**(2): p. 807-18.

68. Wang, Y., et al., *TREM2 lipid sensing sustains the microglial response in an Alzheimer's disease model.* Cell, 2015. **160**(6): p. 1061-71.

69. Hong, S., et al., *Complement and microglia mediate early synapse loss in Alzheimer mouse models.* Science, 2016. **352**(6286): p. 712-716.

70. Lui, H., et al., *Progranulin Deficiency Promotes Circuit-Specific Synaptic Pruning by Microglia via Complement Activation.* Cell, 2016. **165**(4): p. 921-35.

71. Sampson, T.R., et al., *Gut Microbiota Regulate Motor Deficits and Neuroinflammation in a Model of Parkinson's Disease.* Cell, 2016. **167**(6): p. 1469-1480 e12.

72. Liddelow, S.A., et al., *Neurotoxic reactive astrocytes are induced by activated microglia.* Nature, 2017. **541**(7638): p. 481-487.

REFERENCES

73. Salter, M.W. and B. Stevens, *Microglia emerge as central players in brain disease.* Nat Med, 2017. **23**(9): p. 1018-1027.

74. Sulzer, D., et al., *T cells from patients with Parkinson's disease recognize alpha-synuclein peptides.* Nature, 2017. **546**(7660): p. 656-661.

75. Statland, J.M., et al., *Patterns of Weakness, Classification of Motor Neuron Disease, and Clinical Diagnosis of Sporadic Amyotrophic Lateral Sclerosis.* Neurol Clin, 2015. **33**(4): p. 735-48.

76. BROWN, C.H., *INFANTILE AMYOTROPHIC LATERAL SCLEROSIS OF THE FAMILY TYPE.* The Journal of Nervous and Mental Disease, 1894. **19**(11): p. 707-716.

77. E., V., *Contributo alla forma ereditaria della paralisi bulbare progressive. .* Riv. Sper. Freniat, 1936.

78. Van Laere, J., *[Familial progressive chronic bulbo-pontine paralysis with deafness. A case of Klippel-Trenaunay syndrome in siblings of the same family. Diagnostic and genetic problems].* Rev Neurol (Paris), 1966. **115**(2): p. 289-95.

79. Van Laere, J., *[On a new case of chronic bulbopontine paralysis with deafness].* Verh K Vlaam Acad Geneeskd Belg, 1967. **29**(3): p. 288-308.

80. van Laere, J., *[Chronic progressive bulbopontine paralysis with deafness. A clinical syndrome].* Verh K Acad Geneeskd Belg, 1977. **39**(3): p. 126-58.

81. Van Laere, J.E., *[A new case of chronic progressive bulbo-pontine paralysis and deafness].* Rev Neurol (Paris), 1977. **133**(2): p. 119-24.

82. Green, P., et al., *Brown-Vialetto-Van Laere Syndrome, a Ponto-Bulbar Palsy with Deafness, Is Caused by Mutations in C20orf54.* American Journal of Human Genetics, 2010. **86**(3): p. 485-489.

REFERENCES

83. Johnson, J.O., et al., *Exome sequencing reveals riboflavin transporter mutations as a cause of motor neuron disease.* Brain, 2012. **135**: p. 2875-2882.

84. Udhayabanu, T., et al., *Riboflavin Responsive Mitochondrial Dysfunction in Neurodegenerative Diseases.* Journal of Clinical Medicine, 2017. **6**(5).

85. Foley, A.R., et al., *Treatable childhood neuronopathy caused by mutations in riboflavin transporter RFVT2.* Brain, 2014. **137**(Pt 1): p. 44-56.

86. Lek, M., et al., *Analysis of protein-coding genetic variation in 60,706 humans.* Nature, 2016. **536**(7616): p. 285-291.

87. Huber, C.D., B.Y. Kim, and K.E. Lohmueller, *Population genetic models of GERP scores suggest pervasive turnover of constrained sites across mammalian evolution.* PLoS Genet, 2020. **16**(5): p. e1008827.

88. Quang, D., Y. Chen, and X. Xie, *DANN: a deep learning approach for annotating the pathogenicity of genetic variants.* Bioinformatics, 2015. **31**(5): p. 761-3.

89. Sim, N.L., et al., *SIFT web server: predicting effects of amino acid substitutions on proteins.* Nucleic Acids Res, 2012. **40**(Web Server issue): p. W452-7.

90. Lawrence, C.J., et al., *A standardized kinesin nomenclature.* J Cell Biol, 2004. **167**(1): p. 19-22.

91. Verhey, K.J. and J.W. Hammond, *Traffic control: regulation of kinesin motors.* Nature Reviews Molecular Cell Biology, 2009. **10**(11): p. 765-777.

92. Goldenring, J.R., *Recycling endosomes.* Curr Opin Cell Biol, 2015. **35**: p. 117-22.

93. Hu, Y.-B., et al., *The endosomal-lysosomal system: from acidification and cargo sorting to neurodegeneration.* Translational Neurodegeneration, 2015. **4**(1): p. 18.

REFERENCES

94. Weigert, R., et al., *Rab22a regulates the recycling of membrane proteins internalized independently of clathrin.* Mol Biol Cell, 2004. **15**(8): p. 3758-70.

95. Ward, E.S., et al., *From sorting endosomes to exocytosis: association of Rab4 and Rab11 GTPases with the Fc receptor, FcRn, during recycling.* Mol Biol Cell, 2005. **16**(4): p. 2028-38.

96. Sharma, M., et al., *MICAL-L1 links EHD1 to tubular recycling endosomes and regulates receptor recycling.* Mol Biol Cell, 2009. **20**(24): p. 5181-94.

97. Rahajeng, J., et al., *MICAL-L1 is a tubular endosomal membrane hub that connects Rab35 and Arf6 with Rab8a.* Traffic, 2012. **13**(1): p. 82-93.

98. Takahashi, S., et al., *Rab11 regulates exocytosis of recycling vesicles at the plasma membrane.* J Cell Sci, 2012. **125**(Pt 17): p. 4049-57.

99. Solis, G.P., et al., *Reggies/flotillins interact with Rab11a and SNX4 at the tubulovesicular recycling compartment and function in transferrin receptor and E-cadherin trafficking.* Mol Biol Cell, 2013. **24**(17): p. 2689-702.

100. Shakya, S., et al., *Rab22A recruits BLOC-1 and BLOC-2 to promote the biogenesis of recycling endosomes.* EMBO Rep, 2018. **19**(12).

101. Etoh, K. and M. Fukuda, *Rab10 regulates tubular endosome formation through KIF13A and KIF13B motors.* J Cell Sci, 2019. **132**(5).

102. Patel, N.M., et al., *KIF13A motors are regulated by Rab22A to function as weak dimers inside the cell.* Science Advances, 2021. **7**(6): p. eabd2054.

103. Shi, P., et al., *Effects of ALS-related SOD1 mutants on dynein- and KIF5-mediated retrograde and anterograde axonal transport.* Biochim Biophys Acta, 2010. **1802**(9): p. 707-16.

REFERENCES

104. Dafinger, C., et al., *Mutations in KIF7 link Joubert syndrome with Sonic Hedgehog signaling and microtubule dynamics.* J Clin Invest, 2011. **121**(7): p. 2662-7.

105. Ostergaard, P., et al., *Mutations in KIF11 cause autosomal-dominant microcephaly variably associated with congenital lymphedema and chorioretinopathy.* Am J Hum Genet, 2012. **90**(2): p. 356-62.

106. Rath, O. and F. Kozielski, *Kinesins and cancer.* Nature Reviews Cancer, 2012. **12**(8): p. 527-539.

107. Zhou, R., et al., *A Molecular Motor, KIF13A, Controls Anxiety by Transporting the Serotonin Type 1A Receptor.* Cell Reports, 2013. **3**(2): p. 509-519.

108. Shang, Z., et al., *High-resolution structures of kinesin on microtubules provide a basis for nucleotide-gated force-generation.* Elife, 2014. **3**: p. e04686.

109. Bougé, A.L. and M.L. Parmentier, *Tau excess impairs mitosis and kinesin-5 function, leading to aneuploidy and cell death.* Dis Model Mech, 2016. **9**(3): p. 307-19.

110. Hotchkiss, L., et al., *Novel De Novo Mutations in KIF1A as a Cause of Hereditary Spastic Paraplegia With Progressive Central Nervous System Involvement.* J Child Neurol, 2016. **31**(9): p. 1114-9.

111. Muhia, M., et al., *The Kinesin KIF21B Regulates Microtubule Dynamics and Is Essential for Neuronal Morphology, Synapse Function, and Learning and Memory.* Cell Rep, 2016. **15**(5): p. 968-977.

112. Gromova, K.V., et al., *Neurobeachin and the Kinesin KIF21B Are Critical for Endocytic Recycling of NMDA Receptors and Regulate Social Behavior.* Cell Reports, 2018. **23**(9): p. 2705-2717.

113. Gabrych, D.R., et al., *Going Too Far Is the Same as Falling Short(†): Kinesin-3 Family Members in Hereditary Spastic Paraplegia.* Front Cell Neurosci, 2019. **13**: p. 419.

REFERENCES

114. Mandal, K., et al., *Role of a Kinesin Motor in Cancer Cell Mechanics.* Nano Lett, 2019. **19**(11): p. 7691-7702.

115. Li, T.-F., et al., *Overexpression of kinesin superfamily members as prognostic biomarkers of breast cancer.* Cancer Cell International, 2020. **20**(1): p. 123.

116. Lam, C.-W., et al., *Postzygotic inactivating mutation of KIF13A located at chromosome 6p22.3 in a patient with a novel mosaic neuroectodermal syndrome.* Journal of Human Genetics, 2021. **66**(8): p. 825-829.

117. Zahavi, E.E., et al., *Combined kinesin-1 and kinesin-3 activity drives axonal trafficking of TrkB receptors in Rab6 carriers.* Dev Cell, 2021. **56**(4): p. 494-508.e7.

118. Reid, E., et al., *A Kinesin Heavy Chain (KIF5A) Mutation in Hereditary Spastic Paraplegia (SPG10).* The American Journal of Human Genetics, 2002. **71**(5): p. 1189-1194.

119. López, E., et al., *Identification of two novel KIF5A mutations in hereditary spastic paraplegia associated with mild peripheral neuropathy.* Journal of the Neurological Sciences, 2015. **358**(1): p. 422-427.

120. Brenner, D., et al., *Hot-spot KIF5A mutations cause familial ALS.* Brain, 2018. **141**(3): p. 688-697.

121. Nicolas, A., et al., *Genome-wide analyses identify KIF5A as a novel ALS gene.* Neuron, 2018. **97**(6): p. 1268-1283. e6.

122. Bentley, M., et al., *A novel assay reveals preferential binding between Rabs, kinesins, and specific endosomal subpopulations.* J Cell Biol, 2015. **208**(3): p. 273-81.

123. Drecourt, A., et al., *Impaired Transferrin Receptor Palmitoylation and Recycling in Neurodegeneration with Brain Iron Accumulation.* Am J Hum Genet, 2018. **102**(2): p. 266-277.

REFERENCES

124. Sumbria, R.K., *Targeting the transferrin receptor to develop erythropoietin for Alzheimer's disease.* Neural Regen Res, 2020. **15**(12): p. 2251-2252.

125. Gutiérrez, Y., et al., *KIF13A drives AMPA receptor synaptic delivery for long-term potentiation via endosomal remodeling.* Journal of Cell Biology, 2021. **220**(6).

126. Sheff, D.R., et al., *The receptor recycling pathway contains two distinct populations of early endosomes with different sorting functions.* J Cell Biol, 1999. **145**(1): p. 123-39.

127. Collingridge, G.L., J.T.R. Isaac, and Y.T. Wang, *Receptor trafficking and synaptic plasticity.* Nature Reviews Neuroscience, 2004. **5**(12): p. 952-962.

128. Park, M., et al., *Recycling endosomes supply AMPA receptors for LTP.* Science, 2004. **305**(5692): p. 1972-5.

129. Correia, S.S., et al., *Motor protein-dependent transport of AMPA receptors into spines during long-term potentiation.* Nat Neurosci, 2008. **11**(4): p. 457-66.

130. Grant, B.D. and J.G. Donaldson, *Pathways and mechanisms of endocytic recycling.* Nature Reviews Molecular Cell Biology, 2009. **10**(9): p. 597-608.

131. Petrini, E.M., et al., *Endocytic trafficking and recycling maintain a pool of mobile surface AMPA receptors required for synaptic potentiation.* Neuron, 2009. **63**(1): p. 92-105.

132. van der Sluijs, P. and C.C. Hoogenraad, *New insights in endosomal dynamics and AMPA receptor trafficking.* Semin Cell Dev Biol, 2011. **22**(5): p. 499-505.

133. Granger, A.J., et al., *LTP requires a reserve pool of glutamate receptors independent of subunit type.* Nature, 2013. **493**(7433): p. 495-500.

134. Huganir, R.L. and R.A. Nicoll, *AMPARs and synaptic plasticity: the last 25 years.* Neuron, 2013. **80**(3): p. 704-17.

REFERENCES

135. Kneussel, M. and T.J. Hausrat, *Postsynaptic Neurotransmitter Receptor Reserve Pools for Synaptic Potentiation.* Trends Neurosci, 2016. **39**(3): p. 170-182.

136. Birdsall, V., et al., *Axonal transport of Hrs is activity-dependent and rate limiting for synaptic vesicle protein degradation.* bioRxiv, 2021: p. 2020.04.16.044818.

137. Ahmed, K.A. and J. Xiang, *mTORC1 regulates mannose-6-phosphate receptor transport and T-cell vulnerability to regulatory T cells by controlling kinesin KIF13A.* Cell Discovery, 2017. **3**(1): p. 17011.

138. Soppina, V., et al., *Tug-of-war between dissimilar teams of microtubule motors regulates transport and fission of endosomes.* Proc Natl Acad Sci U S A, 2009. **106**(46): p. 19381-6.

139. *The pillars of endocytic sorting: how tubular endosomes are formed.* Journal of Cell Science, 2019. **132**(5): p. e0505-e0505.

140. Gong, X., et al., *KIF13A-regulated RhoB plasma membrane localization governs membrane blebbing and blebby amoeboid cell migration.* Embo j, 2018. **37**(17).

141. Al-Bassam, J. and S. Nithianantham, *Malleable folding of coiled-coils regulates kinesin-3 dimerization.* Proceedings of the National Academy of Sciences, 2018. **115**(51): p. 12845-12847.

142. Ren, J., et al., *Coiled-coil 1-mediated fastening of the neck and motor domains for kinesin-3 autoinhibition.* Proceedings of the National Academy of Sciences, 2018. **115**(51): p. E11933-E11942.

143. Atala, A., *Handbook of Stem Cells 2nd Edition*, R. Lanza, Editor. 2012, Academic Press

144. Takahashi, K. and S. Yamanaka, *Induction of pluripotent stem cells from mouse embryonic and adult fibroblast cultures by defined factors.* Cell, 2006. **126**(4): p. 663-76.

REFERENCES

145. Takahashi, K., et al., *Induction of pluripotent stem cells from adult human fibroblasts by defined factors.* Cell, 2007. **131**(5): p. 861-72.

146. Aasen, T., et al., *Efficient and rapid generation of induced pluripotent stem cells from human keratinocytes.* Nat Biotechnol, 2008. **26**(11): p. 1276-84.

147. Fidan, K., et al., *Transgene-Free Disease-Specific iPSC Generation from Fibroblasts and Peripheral Blood Mononuclear Cells.* Methods Mol Biol, 2016. **1353**: p. 215-31.

148. Doss, M.X. and A. Sachinidis, *Current Challenges of iPSC-Based Disease Modeling and Therapeutic Implications.* Cells, 2019. **8**(5): p. 403.

149. Rizzo, F., et al., *Genome-wide RNA-seq of iPSC-derived motor neurons indicates selective cytoskeletal perturbation in Brown-Vialetto disease that is partially rescued by riboflavin.* Sci Rep, 2017. **7**: p. 46271.

150. Shi, Y., et al., *Haploinsufficiency leads to neurodegeneration in C9ORF72 ALS/FTD human induced motor neurons.* Nature Medicine, 2018. **24**(3): p. 313-325.

151. Georges, P., et al., *Induced pluripotent stem cells-derived neurons from patients with Friedreich ataxia exhibit differential sensitivity to resveratrol and nicotinamide.* Scientific Reports, 2019. **9**(1): p. 14568.

152. Lang, C., et al., *Single-Cell Sequencing of iPSC-Dopamine Neurons Reconstructs Disease Progression and Identifies HDAC4 as a Regulator of Parkinson Cell Phenotypes.* Cell Stem Cell, 2019. **24**(1): p. 93-106 e6.

153. Hernández-Sapiéns, M.A., et al., *A Three-Dimensional Alzheimer's Disease Cell Culture Model Using iPSC-Derived Neurons Carrying A246E Mutation in PSEN1.* Frontiers in Cellular Neuroscience, 2020. **14**(151).

154. Manole, A., et al., *Clinical, pathological and functional characterization of riboflavin-responsive neuropathy.* Brain, 2017. **140**(11): p. 2820-2837.

REFERENCES

155. Marioli, C., et al., *Antioxidant Amelioration of Riboflavin Transporter Deficiency in Motoneurons Derived from Patient-Specific Induced Pluripotent Stem Cells.* International Journal of Molecular Sciences, 2020. **21**(19): p. 7402.

156. Hawrot, J., S. Imhof, and B.J. Wainger, *Modeling cell-autonomous motor neuron phenotypes in ALS using iPSCs.* Neurobiology of Disease, 2020. **134**: p. 104680.

157. Egawa, N., et al., *Drug Screening for ALS Using Patient-Specific Induced Pluripotent Stem Cells.* Science Translational Medicine, 2012. **4**(145): p. 145ra104-145ra104.

158. Burkhardt, M.F., et al., *A cellular model for sporadic ALS using patient-derived induced pluripotent stem cells.* Mol Cell Neurosci, 2013. **56**: p. 355-64.

159. Kiskinis, E., et al., *Pathways Disrupted in Human ALS Motor Neurons Identified through Genetic Correction of Mutant SOD1.* Cell Stem Cell, 2014. **14**(6): p. 781-795.

160. Qu, Q., et al., *High-efficiency motor neuron differentiation from human pluripotent stem cells and the function of Islet-1.* Nature Communications, 2014. **5**(1): p. 3449.

161. Wainger, B.J., et al., *Intrinsic membrane hyperexcitability of amyotrophic lateral sclerosis patient-derived motor neurons.* Cell Rep, 2014. **7**(1): p. 1-11.

162. Du, Z.-W., et al., *Generation and expansion of highly pure motor neuron progenitors from human pluripotent stem cells.* Nature Communications, 2015. **6**(1): p. 6626.

163. Lopez-Gonzalez, R., et al., *Poly(GR) in C9ORF72-Related ALS/FTD Compromises Mitochondrial Function and Increases Oxidative Stress and DNA Damage in iPSC-Derived Motor Neurons.* Neuron, 2016. **92**(2): p. 383-391.

164. Naujock, M., et al., *4-Aminopyridine Induced Activity Rescues Hypoexcitable Motor Neurons from Amyotrophic Lateral Sclerosis Patient-Derived Induced Pluripotent Stem Cells.* Stem Cells, 2016. **34**(6): p. 1563-75.

REFERENCES

165. Bhinge, A., et al., *Genetic Correction of SOD1 Mutant iPSCs Reveals ERK and JNK Activated AP1 as a Driver of Neurodegeneration in Amyotrophic Lateral Sclerosis.* Stem Cell Reports, 2017. **8**(4): p. 856-869.

166. Guo, W., et al., *HDAC6 inhibition reverses axonal transport defects in motor neurons derived from FUS-ALS patients.* Nature Communications, 2017. **8**(1): p. 861.

167. Imamura, K., et al., *The Src/c-Abl pathway is a potential therapeutic target in amyotrophic lateral sclerosis.* Sci Transl Med, 2017. **9**(391).

168. Bianchi, F., et al., *Rapid and efficient differentiation of functional motor neurons from human iPSC for neural injury modelling.* Stem Cell Res, 2018. **32**: p. 126-134.

169. Fujimori, K., et al., *Modeling sporadic ALS in iPSC-derived motor neurons identifies a potential therapeutic agent.* Nat Med, 2018. **24**(10): p. 1579-1589.

170. Marrone, L., et al., *Isogenic FUS-eGFP iPSC Reporter Lines Enable Quantification of FUS Stress Granule Pathology that Is Rescued by Drugs Inducing Autophagy.* Stem Cell Reports, 2018. **10**(2): p. 375-389.

171. Naumann, M., et al., *Impaired DNA damage response signaling by FUS-NLS mutations leads to neurodegeneration and FUS aggregate formation.* Nat Commun, 2018. **9**(1): p. 335.

172. Davis, R.L., H. Weintraub, and A.B. Lassar, *Expression of a single transfected cDNA converts fibroblasts to myoblasts.* Cell, 1987. **51**(6): p. 987-1000.

173. Vierbuchen, T., et al., *Direct conversion of fibroblasts to functional neurons by defined factors.* Nature, 2010. **463**(7284): p. 1035-41.

174. Zhang, Y., et al., *Rapid single-step induction of functional neurons from human pluripotent stem cells.* Neuron, 2013. **78**(5): p. 785-98.

REFERENCES

175. Pfisterer, U., et al., *Direct conversion of human fibroblasts to dopaminergic neurons.* Proc Natl Acad Sci U S A, 2011. **108**(25): p. 10343-8.

176. Son, E.Y., et al., *Conversion of mouse and human fibroblasts into functional spinal motor neurons.* Cell Stem Cell, 2011. **9**(3): p. 205-18.

177. Victor, M.B., et al., *Generation of human striatal neurons by microRNA-dependent direct conversion of fibroblasts.* Neuron, 2014. **84**(2): p. 311-23.

178. Wainger, B.J., et al., *Modeling pain in vitro using nociceptor neurons reprogrammed from fibroblasts.* Nat Neurosci, 2015. **18**(1): p. 17-24.

179. Gasiunas, G., et al., *Cas9-crRNA ribonucleoprotein complex mediates specific DNA cleavage for adaptive immunity in bacteria.* Proc Natl Acad Sci U S A, 2012. **109**(39): p. E2579-86.

180. Jinek, M., et al., *A programmable dual-RNA-guided DNA endonuclease in adaptive bacterial immunity.* Science, 2012. **337**(6096): p. 816-21.

181. Konermann, S., et al., *Optical control of mammalian endogenous transcription and epigenetic states.* Nature, 2013. **500**(7463): p. 472-476.

182. Maeder, M.L., et al., *Targeted DNA demethylation and activation of endogenous genes using programmable TALE-TET1 fusion proteins.* Nature Biotechnology, 2013. **31**(12): p. 1137-1142.

183. Mali, P., K.M. Esvelt, and G.M. Church, *Cas9 as a versatile tool for engineering biology.* Nature Methods, 2013. **10**(10): p. 957-963.

184. Perez-Pinera, P., et al., *RNA-guided gene activation by CRISPR-Cas9-based transcription factors.* Nat Methods, 2013. **10**(10): p. 973-6.

185. Qi, L.S., et al., *Repurposing CRISPR as an RNA-guided platform for sequence-specific control of gene expression.* Cell, 2013. **152**(5): p. 1173-83.

REFERENCES

186. Tanenbaum, M.E., et al., *A protein-tagging system for signal amplification in gene expression and fluorescence imaging.* Cell, 2014. **159**(3): p. 635-46.

187. Chavez, A., et al., *Highly efficient Cas9-mediated transcriptional programming.* Nature Methods, 2015. **12**(4): p. 326-328.

188. Konermann, S., et al., *Genome-scale transcriptional activation by an engineered CRISPR-Cas9 complex.* Nature, 2015. **517**(7536): p. 583-8.

189. Zalatan, J.G., et al., *Engineering complex synthetic transcriptional programs with CRISPR RNA scaffolds.* Cell, 2015. **160**(1-2): p. 339-50.

190. Chavez, A., et al., *Comparison of Cas9 activators in multiple species.* Nat Methods, 2016. **13**(7): p. 563-567.

191. Savell, K.E., et al., *A Neuron-Optimized CRISPR/dCas9 Activation System for Robust and Specific Gene Regulation.* eNeuro, 2019. **6**(1).

192. Ng, A.H.M., et al., *A comprehensive library of human transcription factors for cell fate engineering.* Nat Biotechnol, 2021. **39**(4): p. 510-519.

193. Zhou, M., et al., *Reprogramming astrocytes to motor neurons by activation of endogenous Ngn2 and Isl1.* Stem Cell Reports, 2021. **16**(7): p. 1777-1791.

194. Liu, S., et al., *Neuronal Cell-type Engineering by Transcriptional Activation.* Frontiers in Genome Editing, 2021. **3**(22).

195. Chambers, S.M., et al., *Highly efficient neural conversion of human ES and iPS cells by dual inhibition of SMAD signaling.* Nature Biotechnology, 2009. **27**(3): p. 275-280.

196. Fasano, C.A., et al., *Efficient derivation of functional floor plate tissue from human embryonic stem cells.* Cell Stem Cell, 2010. **6**(4): p. 336-47.

REFERENCES

197. Chavali, V.R.M., et al., *Dual SMAD inhibition and Wnt inhibition enable efficient and reproducible differentiations of induced pluripotent stem cells into retinal ganglion cells.* Scientific Reports, 2020. **10**(1): p. 11828.

198. Reid, J.E. and L. Wernisch, *Pseudotime estimation: deconfounding single cell time series.* Bioinformatics, 2016. **32**(19): p. 2973-80.

199. Sandor, C., et al., *Transcriptomic profiling of purified patient-derived dopamine neurons identifies convergent perturbations and therapeutics for Parkinson's disease.* Hum Mol Genet, 2017. **26**(3): p. 552-566.

200. Hanahan, D., J. Jessee, and F.R. Bloom, *Plasmid transformation of Escherichia coli and other bacteria.* Methods Enzymol, 1991. **204**: p. 63-113.

201. Labun, K., et al., *CHOPCHOP v3: expanding the CRISPR web toolbox beyond genome editing.* Nucleic Acids Res, 2019. **47**(W1): p. W171-w174.

202. Jozefczuk, J., K. Drews, and J. Adjaye, *Preparation of mouse embryonic fibroblast cells suitable for culturing human embryonic and induced pluripotent stem cells.* J Vis Exp, 2012(64).

203. Schmittgen, T.D. and K.J. Livak, *Analyzing real-time PCR data by the comparative C(T) method.* Nat Protoc, 2008. **3**(6): p. 1101-8.

204. Okita, K., et al., *An efficient nonviral method to generate integration-free human-induced pluripotent stem cells from cord blood and peripheral blood cells.* Stem Cells, 2013. **31**(3): p. 458-66.

205. Taapken, S.M., et al., *Karyotypic abnormalities in human induced pluripotent stem cells and embryonic stem cells.* Nature Biotechnology, 2011. **29**(4): p. 313-314.

206. Vitale, A.M., et al., *Variability in the generation of induced pluripotent stem cells: importance for disease modeling.* Stem Cells Transl Med, 2012. **1**(9): p. 641-50.

REFERENCES

207. Volpato, V. and C. Webber, *Addressing variability in iPSC-derived models of human disease: guidelines to promote reproducibility.* Dis Model Mech, 2020. **13**(1).

208. Sun, M.-a., et al., *Homeobox transcription factor MNX1 is crucial for restraining the expression of pan-neuronal genes in motor neurons.* bioRxiv, 2021: p. 2021.08.07.455331.

209. Sagner, A., et al., *Olig2 and Hes regulatory dynamics during motor neuron differentiation revealed by single cell transcriptomics.* PLOS Biology, 2018. **16**(2): p. e2003127.

210. D'Erchia, A.M., et al., *Massive transcriptome sequencing of human spinal cord tissues provides new insights into motor neuron degeneration in ALS.* Scientific Reports, 2017. **7**(1): p. 10046.

211. Srinivasan, K., et al., *Untangling the brain's neuroinflammatory and neurodegenerative transcriptional responses.* Nature Communications, 2016. **7**(1): p. 11295.

212. Ofengeim, D., et al., *Single-Cell RNA Sequencing: Unraveling the Brain One Cell at a Time.* Trends Mol Med, 2017. **23**(6): p. 563-576.

213. Mukherjee, S., et al., *A Microglial Signature Directing Human Aging and Neurodegeneration-Related Gene Networks.* Frontiers in Neuroscience, 2019. **13**.

214. Andrade-Navarro, M.A., et al., *RNA Sequencing of Human Peripheral Blood Cells Indicates Upregulation of Immune-Related Genes in Huntington's Disease.* Frontiers in Neurology, 2020. **11**.

215. Dols-Icardo, O., et al., *Motor cortex transcriptome reveals microglial key events in amyotrophic lateral sclerosis.* Neurology - Neuroimmunology Neuroinflammation, 2020. **7**(5): p. e829.

216. Ahmadi, A., et al., *Single-cell Transcriptional Changes in Neurodegenerative Diseases.* Neuroscience, 2021. **479**: p. 192-205.

REFERENCES

217. Neff, R.A., et al., *Molecular subtyping of Alzheimer’s disease using RNA sequencing data reveals novel mechanisms and targets.* Science Advances, 2021. **7**(2): p. eabb5398.

218. Sobue, A., et al., *Microglial gene signature reveals loss of homeostatic microglia associated with neurodegeneration of Alzheimer's disease.* Acta Neuropathologica Communications, 2021. **9**(1): p. 1.

219. Titeca, K., et al., *Discovering cellular protein-protein interactions: Technological strategies and opportunities.* Mass Spectrom Rev, 2019. **38**(1): p. 79-111.

220. Roux, K.J., et al., *BioID: A Screen for Protein-Protein Interactions.* Curr Protoc Protein Sci, 2018. **91**: p. 19.23.1-19.23.15.

221. Kalocsay, M., *APEX Peroxidase-Catalyzed Proximity Labeling and Multiplexed Quantitative Proteomics.* Methods Mol Biol, 2019. **2008**: p. 41-55.

222. Cho, K.F., et al., *Proximity labeling in mammalian cells with TurboID and split-TurboID.* Nat Protoc, 2020. **15**(12): p. 3971-3999.

223. Samavarchi-Tehrani, P., R. Samson, and A.-C. Gingras, *Proximity Dependent Biotinylation: Key Enzymes and Adaptation to Proteomics Approaches*.* Molecular & Cellular Proteomics, 2020. **19**(5): p. 757-773.

224. Zhou, Y. and N.C. Danbolt, *Glutamate as a neurotransmitter in the healthy brain.* J Neural Transm (Vienna), 2014. **121**(8): p. 799-817.

225. Lewerenz, J. and P. Maher, *Chronic Glutamate Toxicity in Neurodegenerative Diseases—What is the Evidence?* Frontiers in Neuroscience, 2015. **9**.

226. Jakaria, M., et al., *Neurotoxic Agent-Induced Injury in Neurodegenerative Disease Model: Focus on Involvement of Glutamate Receptors.* Frontiers in Molecular Neuroscience, 2018. **11**.

REFERENCES

227. Armada-Moreira, A., et al., *Going the Extra (Synaptic) Mile: Excitotoxicity as the Road Toward Neurodegenerative Diseases.* Frontiers in Cellular Neuroscience, 2020. **14**.

228. Hu, N., M.A. Rutherford, and S.H. Green, *Protection of cochlear synapses from noise-induced excitotoxic trauma by blockade of Ca²⁺-permeable AMPA receptors.* Proceedings of the National Academy of Sciences, 2020. **117**(7): p. 3828-3838.

229. Zaghmi, A., et al., *Sustained blood glutamate scavenging enhances protection in ischemic stroke.* Communications Biology, 2020. **3**(1): p. 729.